# DEVELOPMENT OF A COMPUTATIONAL MODEL TO INVESTIGATE THE THERMO-MECHANICAL BEHAVIOUR OF CUTTING TOOLS

# DEVELOPMENT OF A COMPUTATIONAL MODEL TO INVESTIGATE THE THERMO-MECHANICAL BEHAVIOUR OF CUTTING TOOLS

By

MD KHALID SAIFULLAH

B.S.C Eng., (Islamic University of Technology, Bangladesh))

A Thesis

Submitted to the School of Graduate Studies

in Partial Fulfilment of the Requirements

for the Degree

Master of Applied Science

McMaster University



MASTER OF APPLIED SCIENCE (2019) McMaster University

(Mechanical Engineering) Hamilton, Ontario

TITLE: **DEVELOPMENT OF A COMPUTATIONAL MODEL TO INVESTIGATE THE THERMO-MECHANICAL BEHAVIOUR OF CUTTING TOOLS**

AUTHOR: MD KHALID SAIFULLAH

B.S.C. Eng., (Islamic University of Technology, Bangladesh)

SUPERVISOR: Dr. Stephen C. Veldhuis

Department of Mechanical Engineering

McMaster University

NUMBER OF PAGES: CXLVII, 147

## Abstract

During machining, the cutting tool wears out and affects the machined surface quality and overall production cost. The prediction of tool wear and analysis of cutting mechanics has significant importance for process optimization and cutting-edge design. In this present study, an efficient FE simulation approach (Arbitrary Eulerian-Lagrangian) on the Abaqus/Explicit platform has been developed to improve the predictability of flank wear and to select the appropriate tool edge geometry in the orthogonal turning operation. The FE model was calibrated by comparing the simulation and experimental force values. A new approach was applied to capture the worn tool geometry based on the frictional stress value acting on the cutting tool. The effect of wear geometry on the cutting zone was investigated with respect to temperature, normal stress, sliding velocity, and plastic deformation. The experimental tool wear pattern and characteristics for the differently prepared edges were studied and compared to the thermo-mechanical value retrieved from the FE model. Tool wear for differently prepared edges was calculated using Usui's wear rate equation, which was calibrated using a hybrid calibration method. The efficiency of the calibration method was investigated at different cutting speeds and feed rates. The performance of pre-coating edge preparation was evaluated in both experimental and numerical studies.

## Acknowledgements

First and foremost, I would like to express my sincere gratitude to my supervisor, Dr. Stephen Veldhuis, for his selfless guidance. His support and suggestions have gone a long way towards not only producing this thesis, but also towards improving my understanding in research methodologies and thinking creatively. I could not be more thankful to him for providing me with the opportunity to be a part of the large, loving family that is the McMaster Manufacturing Research Institute (MMRI).

In addition, I would like to express my deepest gratitude to Dr. Abul Arif for his exceptional guidance. I walked away from every weekly meeting with him with new ideas stemming from his constructive advice, and this thesis would not be possible without him. On a similar note, I would like to thank the MMRI team: Dr. Jose de Paiva, Dr. Maryam Aramesh, Simon, Terry, Steve, Brady and Jennifer - thank you all for patience, guidance and training. Without your help, I would have never been able to utilize the facilities as I have and would not have been able to accomplish many industrial and research tasks.

Secondly, I would like to acknowledge and thank the friends I have met before and after moving to Canada. Shariful Islam Chowdhury: you have always been by my side and have supported me from the beginning. Alam and Rohan: your encouragement when I first started at the lab helped me acclimatize to this new environment very quickly. Nino, Kan and Abdo: we have laughed, cried, and toiled together for the past two years, and I could not think of three other people I would want to graduate with. For those whose names I have not been able to mention due to space constraints: I hope you know who you are and that I am forever grateful for your continued encouragement.

Last but not the least, I would like to thank my beloved mother, grandmother, and sisters for their endless love and support in whatever decisions I have made throughout this journey, and my fiancé for her brilliant support. I would never have become who I am without your love. I love you all.

## Table of Contents

## List of Figures

## List of Tables

**List of Abbreviations and Symbols**

| | |
|---|---|
| FEM | Finite element methods |
| PSDZ | Primary shear deformation zone |
| SSDZ | Secondary shear deformation zone |
| TSDZ | Tertiary shear deformation zone |
| $\alpha$ | Rake angle |
| $\gamma$ | Clearance angle |
| $t_c$ | Chip thickness |
| t | Uncut chip thickness |
| $\varphi$ | Shear angle |
| $\beta$ | Friction angle |
| Fc | Cutting force (Tangential force) |
| Ft | Feed force (Thrust force) |
| $F_s$ | Shear force |
| $F_c$ | Friction force |
| $N_s$ | Shear normal force |
| $N_c$ | Normal friction force |
| $\mu$ | Coefficient of friction |
| $\tau$ | The frictional shear stress |
| BUE | Built Up Edge |
| r | Chip thickness ratio |
| $\rho$ | Material Density |
| $l_f$ | Tool-chip contact length |
| $\eta_f$ | Percentage of the energy converted to heat |
| C | Specific heat |
| $\beta_H$ | Percentage of the heat transmitted to workpiece |
| $\Delta S$ | Incremental slip |
| K | Heat conductivity |

| | |
|---|---|
| $\eta_m$ | The fraction of inelastic heat dissipation |
| K | Form factor |
| φ | Apex angle |
| $\frac{dw}{dt}$ | Tool wear rate |
| P | Applied load in tribometer |
| $\tau_f$ | frictional stress |
| $\mu$ | coefficient of friction |
| $\sigma_n$ | normal stress |
| $\tau_{max}$ | limiting frictional stress |
| SL | Sacrificial layer |
| CVD | Chemical Vapor Deposition (coating) |
| PVD | Physical Vapor Deposition (coating) |
| ALE | Arbitrary Lagrangian Eulerian |
| CEL | Coupled Eulerian-Lagrangian |
| UL | Updated Lagrangian |
| A | A Johnson-Cook plastic model invariant parameter |
| B | A Johnson-Cook plastic model invariant parameter |
| C | strain rate dependency in Johnson-Cook plastic model |
| n | Experimental factor in Johnson-Cook |
| m | Experimental factor in Johnson-cook |
| $\dot{\varepsilon}$ | Strain rate |
| $\dot{\varepsilon}_{ref}$ | Reference strain rate in Johnson cook model |
| $\theta_{amb}$ | Ambient temperature |
| $\theta_{melt}$ | Melting temperature |
| RMSE | Root mean square error |
| MAPE | Mean absolute percentage error |

# CHAPTER 1. INTRODUCTION

## 1.1 Background

Modern manufacturing processes demand reliable, stable and highly productive cutting processes. This necessitates significant improvements in the design of cutting tool microgeometry, new coatings and improved tool substrate and workpiece materials. The design of cutting tool micro-geometry refers to the micro shaping of sharp edges into a smooth profile using an edge preparation technique. By changing the properties and micro-geometry of the edge, cutting edge preparation strengthens the cutting edge, enhances tool life, minimizes the propensity of chipping, improves part quality and enhances the workpiece surface finish [1], [2], [3]. Prepared cutting tools with a coated layer can improve cutting tool performance to a great extent [4], [5].

Increased thermo-mechanical loads during machining generate wear on the cutting tool. The micro-geometry of the cutting-edge influences cutting mechanics that determine the progress of tool wear. Denkena et al. [6] reported that the direction and magnitude of the thermal load on the cutting edge are influenced by cutting edge geometry. Plastic deformation, chipping, flaking and crack formation are all largely dependent on the mechanical load produced by the cutting edge [7]. The stability of the process can be influenced by the geometry of the cutting edges, particularly in micro-machining procedures [8]. The chip formation mechanism is controlled by the ratio of edge radius to uncut chip thickness [9]. The machined surface quality is dependent on the geometrical shape of the edge radius [10]. Furthermore, the initial cutting-edge shape changes during the course of tool wear, which also alters the thermo-mechanical load on the cutting tool and induces undesirable tensile residual stresses on the machined surface [11]. Therefore, cutting tool design requires a thorough evaluation of the thermo-mechanical properties of the cutting processes.

Metal cutting is a highly dynamic mechanical process with strain rates of up to $10^6$ $s^{-1}$ and a temperature that can reach nearly 1000ºC [12]. Due to the nature of the cutting process, it is difficult and expensive to experimentally measure process outputs such as temperature, stress and cutting forces. With the advancement of electronic technology, Finite Element Analysis has become one of the most powerful tools for simulating metal cutting processes. The finite element method (FEM) based metal cutting simulation helps gain a better understanding of the development of deformation zones and subsequent thermo-mechanically affected zones [13], [14], [7]. One of FEA's most useful features is its ability to predict the chip formation process [15], [16]. Residual stress on the machined surfaces and stagnation zones on the tool tip are key to evaluating the integrity of the machined surface. Both of these parameters have been successfully modeled using FEM [17], [18]. Tool wear prediction using FEA is becoming increasingly popular among researchers [11], [19]–[21].

A coating applied to the tool can improve machining performance by acting as a thermal barrier [22]. The structure and properties of a coating have a significant influence on coating performance [23]. FE investigations have been performed to understand the effect of coating properties and architecture in the cutting zone [23], [24].

## 1.2 Motivation

Optimizing cutting edge microgeometry requires a thorough understanding of the thermo-mechanical behaviours occurring in the cutting zone. FE modelling is a promising candidate for accomplishing this task. However, most published studies on FE modelling, focus on the workpiece material rather than the cutting tool. There is scarce literature on the effect of cutting-edge geometry on the thermo-mechanical behaviour and performance of the tool. A limited number of investigations have been conducted on the effects of edge micro-geometry and edge preparation techniques on tool stress and temperature and even fewer linking numerical results to experimental tool-life performance.

The aim of the current research is to provide a detailed understanding of the effect that a prepared cutting tool micro-geometry has on both coated and uncoated cutting tools using experimental and FE analysis during orthogonal finish turning of AISI 4140 alloy steel. An effective method of predicting tool wear using a hybrid calibration method is presented.

## 1.3 Research Objective

The chief goal of the current study is to investigate the effect of tool-microgeometry on the thermo-mechanical loads acting on the cutting tool. The following is a summary of this research project's objectives:

1. To develop an efficient computational model for studying the thermo-mechanical behaviour of uncoated and coated tools that accounts for tool wear.
2. To conduct a thorough numerical investigation of the thermo-mechanical behaviour of tools with differently prepared cutting edges.
3. To investigate the effect of pre-coating edge preparation on tool performance using experimental and numerical studies.

## 1.4 Thesis Outline

This paper is organized into seven chapters. The following is a summary of each:

CHAPTER 1 INTRODUCTION: The effects of edge preparation on tool wear are described and the motivation behind this research is outlined.

CHAPTER 2 LITERATURE REVIEW: A detailed overview of orthogonal cutting, FE modelling techniques, friction modelling, tool wear mechanisms, tool wear modelling and coating modelling techniques are provided.

CHAPTER 3 FE MODELLING: This chapter details the material model, boundary conditions and meshing techniques used in this study's FE models. All three formulation methods are compared to experimental data and the best formulation method is selected.

CHAPTER 4 THERMO-MECHANICAL BEHAVIOUR OF EDGE GEOMETRIES: This chapter is a detailed study of the thermo-mechanical loads on differently prepared cutting edges. Changes in thermo-mechanical behaviour on the cutting edge due to tool wear are presented. Furthermore, FE results are related to experimental tool wear. A detailed thermo-mechanical study of prepared edges by different techniques are provided.

CHAPTER 5 MODELLING OF COATED TOOL: This chapter presents a thorough description of the cutting test experimental set up with prepared coated tools, including the experimental methodology and the coating deposition technology. A comprehensive thermo-mechanical study was performed to understand the behaviour of the coated tool.

CHAPTER 6 TOOL WEAR PREDICTION: Tool wear is predicted using a hybrid calibration method. The prediction accuracy is tested at different cutting speeds. A parametric study of tool wear progression is conducted at different cutting speeds and feed rates.

CHAPTER 7 CONCLUSION AND FUTURE STUDY: This chapter highlights the significant results of this study. Cutting-edge geometry is recommended to optimize cutting processes.

# CHAPTER 2. LITERATURE REVIEW

## 2.1 Orthogonal cutting

In this research, both the experimental and numerical study will focus on orthogonal machining. As shown in Fig. 1(a), the cutting edge is perpendicular to cutting velocity(v) and chip flow($v_c$) in orthogonal machining. The inclination angle (i) between the workpiece and the cutting tool is always zero. To simplify the orthogonal cutting into a two-dimensional analysis, uncut chip thickness (t) must be smaller than one tenth the width of the cut (b) [25].

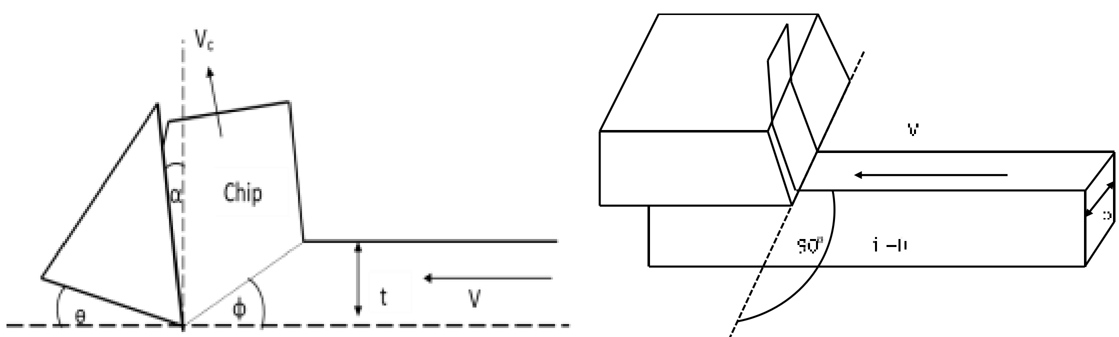


a) b)

Figure 1: a) 2D orthogonal cutting b) 3D orthogonal cutting [25]

Merchant [26] first introduced the force circle, based on the concept of 2D orthogonal cutting. In Merchant's model, the cutting tool is assumed to be perfectly sharp and without any built-up edge. The workpiece material is considered to be homogenous. Fig. 2 shows that the resultant force (R) can be separated into cutting force ($F_c$) along the horizontal direction and feed force ($F_t$) in the vertical direction. The force component along the tool rake face is the frictional force ($F_r$), and the component perpendicular to the rake face is the normal friction force ($N_r$). The shear force ($F_s$) acts along the slip line, and the normal shear force ($N_s$) acts perpendicular to it.

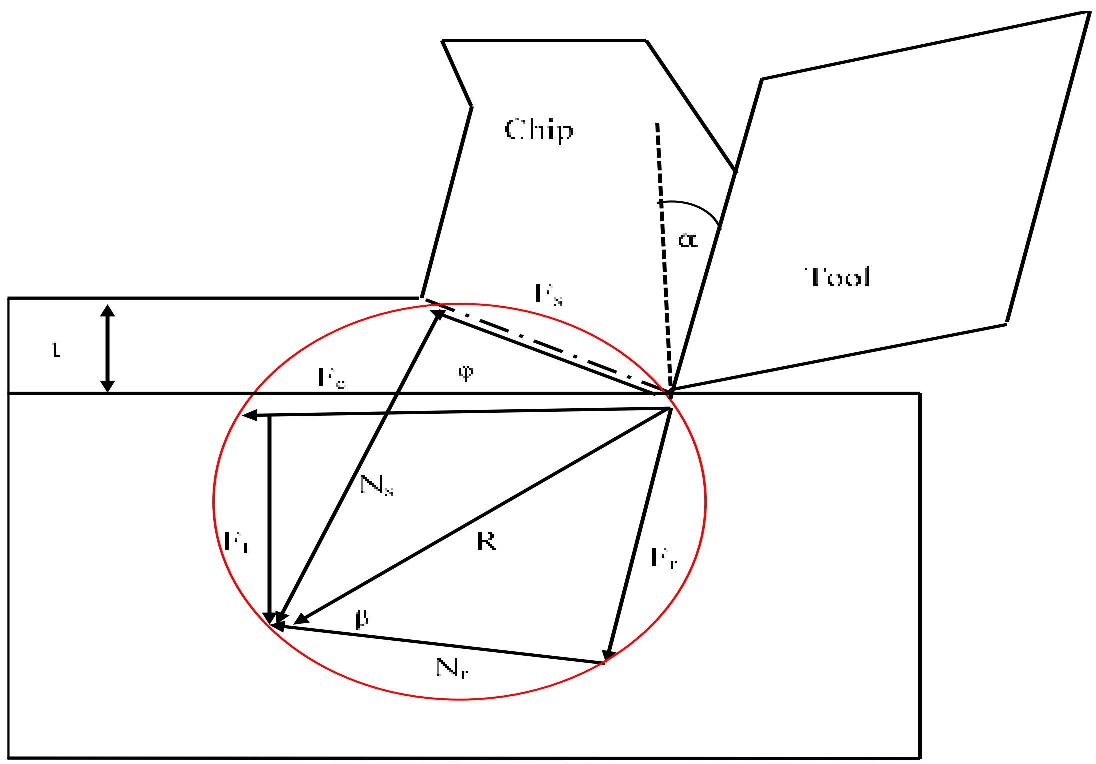


Figure 2: Merchant Circle Diagram [27]

Shear forces on a shear plane can be represented as a function of the cutting forces ($F_c$) and shear angle(φ);

$$F_s = F_c \cos\varphi - F_t \sin\varphi \quad (1)$$

$$N_s = F_t \cos\varphi - F_c \sin\varphi \quad (2)$$

The friction force ($F_r$) and normal force ($N_r$) act on the rake face, and can be represented as a function of the rake angle and cutting forces;

$$F_r = F_c \sin\alpha + F_t \cos\alpha \quad (3)$$

$$N_r = F_c \cos\alpha - F_t \sin\alpha \quad (4)$$

Plastic deformation takes place as the workpiece is being cut during metal cutting. Primarily, two shear deformation zones are developed, as shown in Fig. 3. As the chip is being formed, maximum shear stress can be found in front of the tool tip where the chip separates from the machined surface. This is known as the primary shear deformation zone (PSDZ). The chip thickness ($t_c$) depends upon the degree of deformation at the PSDZ. A secondary shear deformation zone (SSDZ) appears as a result of higher than normal stress (~3GPa) acting on the tool-chip interface.

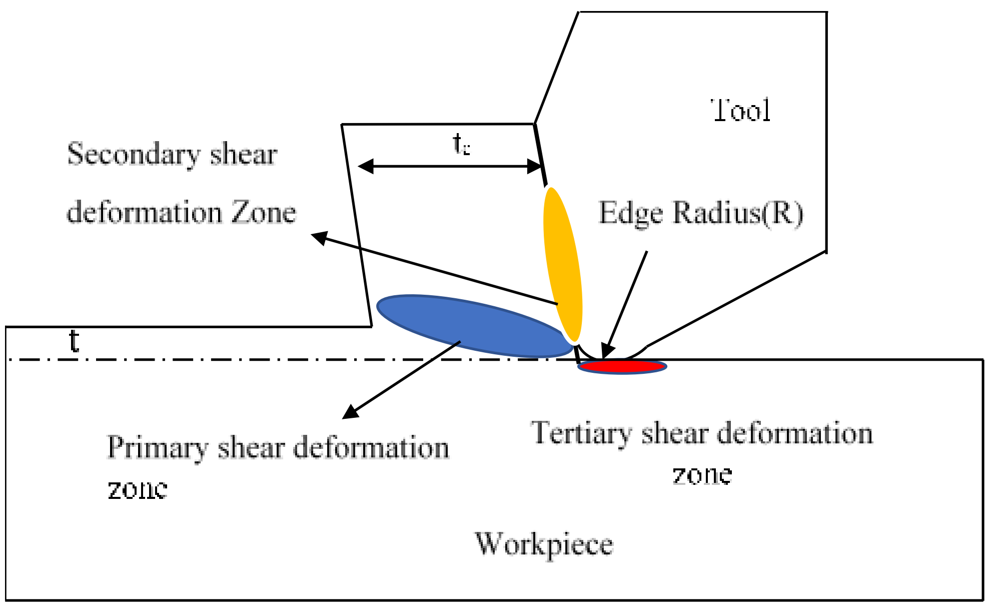


Figure 3: Plastic Deformation zones during machining [27]

No cutting edge is perfectly sharp. The edge radius (R) will induce ploughing while machining. Therefore, friction phenomena take place between the cutting tool and the machined surface, resulting in the formation of a tertiary shear deformation zone. The tertiary shear deformation zone deteriorates surface finish and accelerates flank wear. The modelling and investigation of the secondary and tertiary shear deformation zone will be the main focus of this study.

## 2.2 Finite element formulation and technique

Four main formulation methods have been used over the years to simulate the metal cutting process [28], [17], [29], [30]. The formulation methods are as follows:

a) Eulerian Formulation (EF)
b) Updated Lagrangian (UL)
c) Arbitrary Eulerian-Lagrangian (ALE)
d) Coupled Eulerian-Lagrangian (CEL)

The Eulerian and Lagrangian methods are the two basic formulation methods for every finite element analysis. The relationship between the two formulation methods can be illustrated by a generalized equation (5) [31]:

$$\bar{V}_i = a_i + b_i * V_i \tag{5}$$

where, $V_i$ is the velocity of the material point, $\bar{V}_i$ is the velocity of the mesh grid point, and $a_i$ and $b_i$ are arbitrary coefficients that define the mesh motion scheme. For instance, $a_i = b_i = 0$ refers to the Eulerian formulation while $a_i = 0$, $b_i = 1$ represents the Lagrangian formulation.

Fig. 4 represents the mesh grid and material behaviour during deformation for Lagrangian and Eulerian formulations, respectively. However, in the Arbitrary Eulerian Lagrangian (ALE) method, both $a_i$ and $b_i$ are non-zero and constant. In the Coupled Eulerian Lagrangian (CEL) method, the workpiece is considered as to be Eulerian, and the tool, Lagrangian. ALE and CEL are also called hybrid formulation methods. These hybrid formulation methods are utilized to control higher element distortion in cutting simulations. The three most popular formulation methods are discussed in this literature and will be simulated later on.

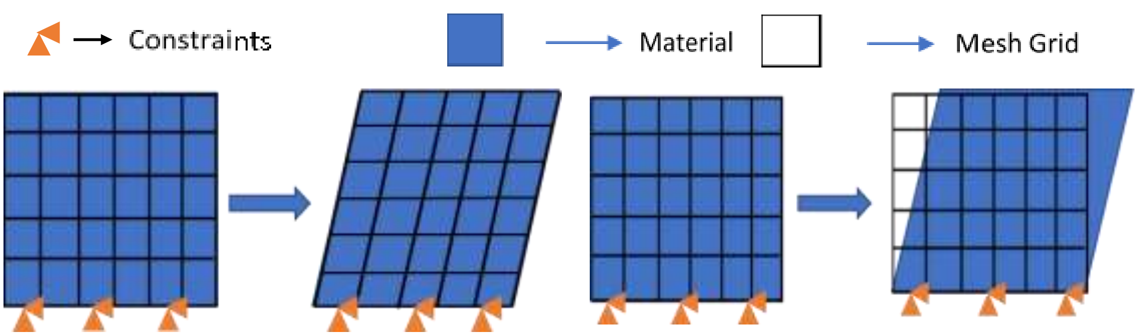


a) Lagrangian formulation, $a_i$=0, $b_i$=1 b) Eulerian formulation, $a_i$ =$b_i$=0

Figure 4: Deformation behavior of a) Lagrangian b) Eulerian Formulation

### 2.2.1 Updated Lagrangian (UL)

The Updated Lagrangian formulation technique is the most widely used for solving solid mechanics problems [32]–[34]. The Lagrangian approach allows material and mesh to flow simultaneously. The simplicity of this formulation method makes the cutting simulation convenient for FE engineers and researchers. Figure 5 shows a typical cutting simulation model done with the Lagrangian formulation [35]. However, controlling large deformation during simulation is one of the major challenges with this formulation method. The mesh often becomes severely distorted due to large deformations, forcing the simulation to terminate itself. To control the element distortion, a predefined sacrificial layer on the workpiece is kept right below the uncut chip thickness. The sacrificial layer elements are removed as the cutting tool moves along the workpiece. Thus, the chip grows automatically, and an initial chip assumption is not required. In Fig. 5, elements A and B represent the sacrificial layer used in the Lagrangian simulation; the use of a sacrificial layer requires a damage model to remove the elements along with the sacrificial layer. The simulation result is significantly influenced by the parameters used by the damage model [27].

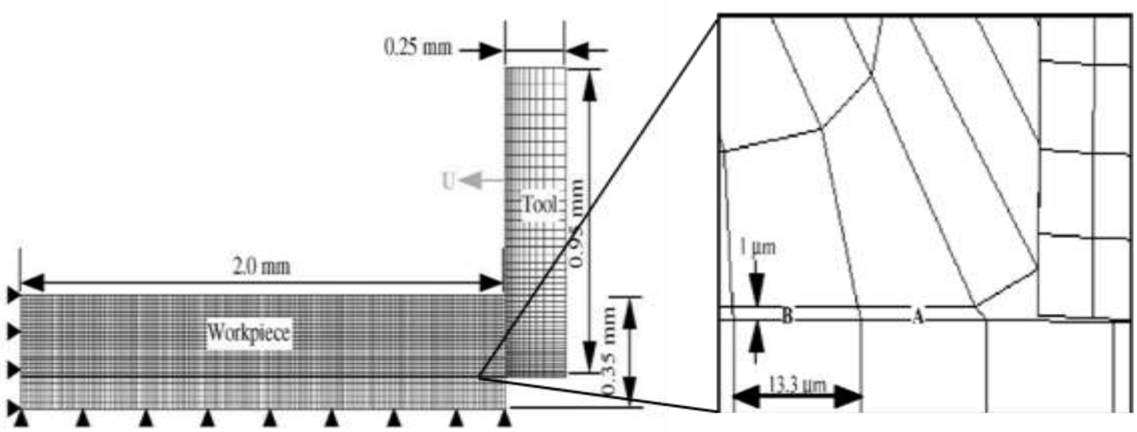


Figure 5: The updated Lagrangian formulation technique with sacrificial element A, B (reprinted with permission [32])

Huang and Black [36] illustrated the evolution of the separation model based on nodal distance, plastic strain, energy density, and stress. They concluded that both the geometrical and physical criteria could not simulate initial cutting accurately. One of the main drawbacks of using a sacrificial layer is the inability to capture valuable information such as the stagnation zone, ploughing, and size effect. The model is also incapable of predicting feed force (Ft) [27]. Despite the drawbacks of the Lagrangian formulation method, it is mostly used among researchers due to its ability to predict workpiece microstructure [37], segmental chip formation [38], and 3D modeling [39].

### 2.2.2 Arbitrary Lagrangian Eulerian (ALE)

Both the Eulerian and Lagrangian methods have some drawbacks when predicting the characteristics of metal cutting. The Arbitrary Lagrangian and Eulerian (ALE) formulation combines the advantages of both formulation methods and minimizes the limitations of the metal cutting simulation. ALE formulation method is applied by FEM software by activating an adaptive mesh option. There are different ways of formulating the ALE method: implementing Eulerian and sliding surfaces with the definition of the inflow/outflow of the material [38], [39], defining Eulerian and Lagrangian regions separately [42] or simply using an adaptive remeshing technique in the workpiece element [43]. Fig. 6 shows the boundary conditions of the ALE approach where Eulerian and Lagrangian regions have been defined separately at different partitions of the workpiece. The Eulerian region is activated simply by constraining the mesh (Zone B). The uncut chip thickness has been deliberately kept Lagrangian to allow the chip grow on its own. The main purpose of defining the Eulerian region near the tooltip is to prevent excessive element distortion during cutting without using a sacrificial layer.

The cutting simulation can be performed with a different cutting-edge radius, which is one of the major advantages of the ALE formulation. In addition, the stagnation zone in front of the tool-tip can be characterized by this approach [42]. The ALE modeling approach is still limited to orthogonal cutting and is incapable of simulating bi-metal workpiece materials. The ALE formulation has been used for predicting the temperature in the cutting zone [44] as well as the residual stress [42].

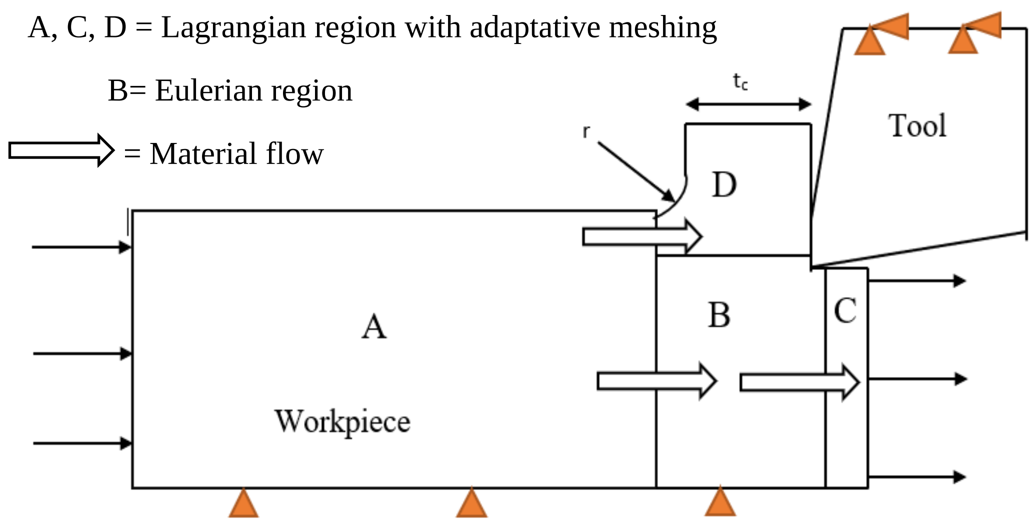


Figure 6: Boundary conditions and material flow of ALE formulation technique [36]

### 2.2.3 Coupled Eulerian-Lagrangian (CEL)

A Coupled Eulerian-Lagrangian (CEL) simulation is performed by considering the workpiece as an Eulerian domain and the cutting tool as a Lagrangian body. The Eulerian domain includes the initial shape of the workpiece and the area for chip formation. Fig. 7 shows mesh discretization and boundary conditions for CEL formulation. The primary objective of this simulation method is to avoid extreme deformation in the metal cutting simulation with a simpler approach. The CEL method is relatively new compared to the other formulation methods (ALE, UL).

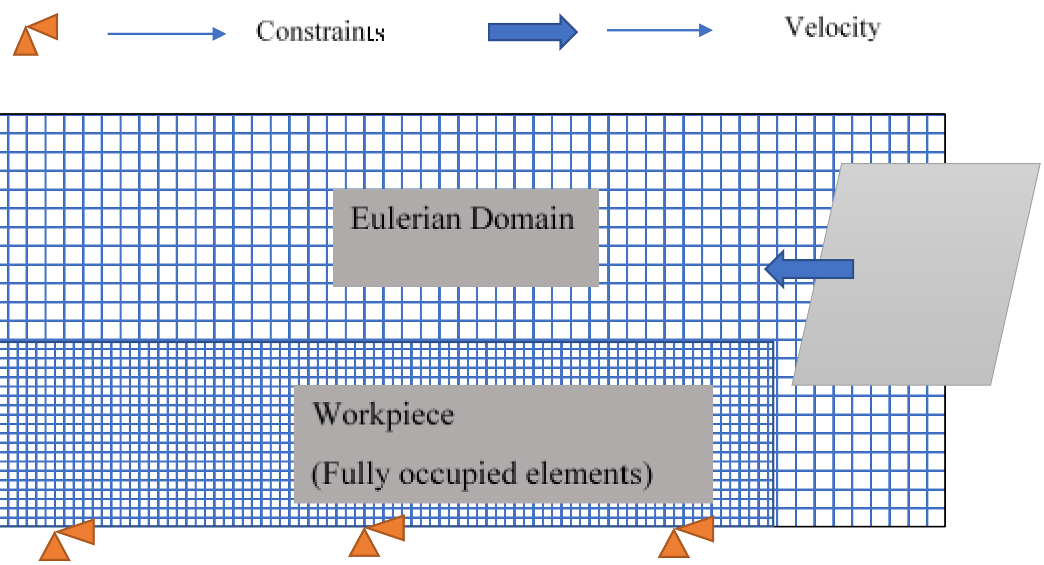


Figure 7: Boundary conditions and meshing technique of ALE formulation [ 46]

This method does not require any damage model, and output solutions are close to those of the ALE formulation [30]. Yancheng Zhang et al. [30] compared output results from the ALE, CEL and UL formulation methods for orthogonal machining of Ti6Al4V. He observed that ALE and CEL provides nearly identical results for cutting force, feed force, chip thickness ratio, and contact length. F. Ducobu et al. [45] further observed the similarities in force prediction for the ALE and CEL formulations. However, this simulation is performed within a 3D environment that requires an extended computational period to process the large number of elements in the simulated model.

Every formulation method has its advantages and disadvantages. The formulation is selected based on the interest of the research.

## 2.3 Modeling of tool-chip interaction

Proper tool-chip interaction modeling can capture more realistic machining mechanisms in a cutting simulation. The interaction properties are defined as a combination of mechanical and thermal properties.

### 2.3.1 Mechanical interaction

The mechanical interaction between the tool-chip interface mainly corresponds to the friction behaviour. There are several friction models available that can be used in cutting simulations. All friction models were implemented based on the cutting mechanism at the tool-chip interface. Some of the fundamental friction models are discussed below:

**Coulomb friction law**

Coulomb's first law of friction is defined as:

$$\tau = \mu * \sigma \tag{6}$$

The frictional shear stress ($\tau$) along the tool rake face is proportional to the normal stress ($\sigma$). The friction coefficient ($\mu$) is the simulation input. It has been stated that defining a constant friction coefficient only at the tool-chip interface is an oversimplification, as it cannot capture the sticking and sliding phenomena during metal cutting [46]. Generally, the coefficient of friction is determined using the Merchant diagram as a function of cutting forces and rake angle.

$$\mu = \frac{Fc\ Sin\alpha + Ft\ cos\alpha}{Fc\ cos\alpha - Ft\ sin\alpha} \tag{7}$$

**Constant shear friction model**

In this model, the frictional shear stress is constant at the rake face. The frictional shear stress is determined by the material flow stress of the workpiece (k) multiplied by the constant shear friction factor (m). The constant shear friction factor (m) also known as the sticking friction coefficient.

$$\tau = m * k \tag{8}$$

In this case, the input values are both flow stress and the constant shear friction factor. The flow stress is a function of shear angle (∅), cutting forces ($F_c$, $F_t$) and undeformed chip thickness (t).

$$k = \frac{(Fc\ cos\emptyset - Ft \sin^2 \emptyset)}{(t\ u\ w)} \tag{9}$$

**Constant shear in sticking and Coulomb friction in sliding**

This approach is very popular and combines two previous methods to capture a more realistic mechanism of tool-chip interaction. Coulomb's friction law is used in the sliding region and constant shear friction model in the sticking region.

$$\tau = m * k \text{ when } 0 < x < l_p \tag{10}$$

$$\tau = \mu * \sigma \text{ when } l_p < x < l_c \tag{11}$$

where the $l_p$ value is the sticking region distance, $l_c$ represents the sliding region distance and k represents the material flow stress. The $l_p$ and $l_c$ values must be determined experimentally.

**Zorev friction model**

According to the Zorev friction model, two distinct friction regions develop at the tool-chip contact length due to stress phenomena caused by metal cutting. The normal stress is at a maximum near the tool tip; this decreases exponentially and becomes zero at the point where the chip loses contact with the tool. Due to this higher-than-normal stress at the tool tip, the chip deforms plastically, resulting in a sticking zone.

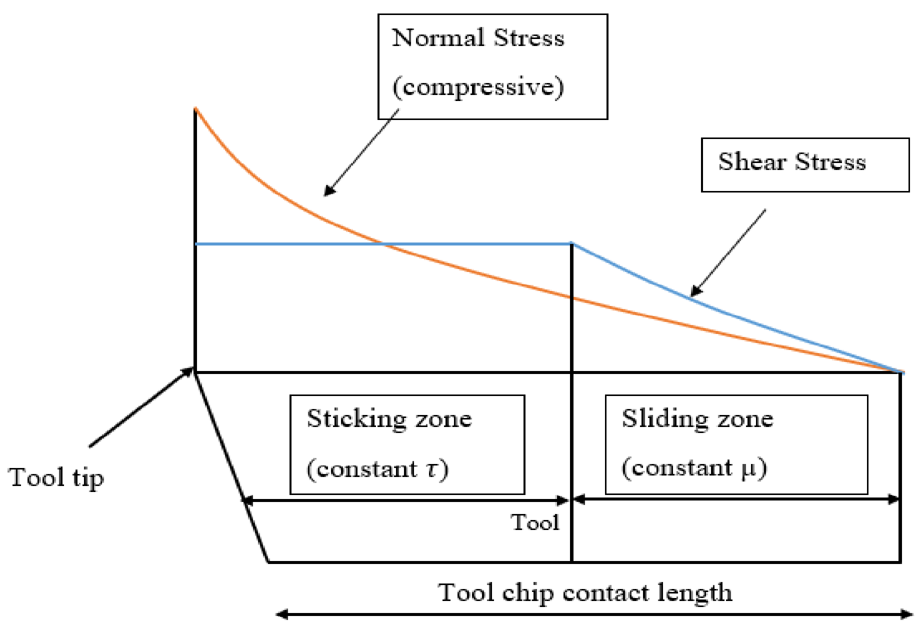


Figure 8: Normal and shear stress phenomena at the tool chip contact length

The classical friction model becomes irrelevant in the sticking zone due to the plastically deformed tool-chip interface, thus requiring constant shear stress to be defined. Both shear and normal stresses decrease proportionally within sliding region. The classical friction law applies.

Maximum shear stress ($\tau_{max}$) and COF ($\mu$) are assumed to be the inputs as for friction parameters in the FE model. This way, no experiment of either the sticking or sliding lengths is needed. Arrazola et al [41] investigated the effect of different constant shear stresses on cutting forces and temperature. It was found that both the cutting force and feed force increase up to a certain limit, $\tau_{max}$. Once the limit $\tau_{max}$ was exceeded, both temperature and force became almost constant Also, the maximum limited shear stress can be estimated in Eqn.12 [44]:

$$\tau_{max} = \sigma y/\sqrt{3} \qquad (12)$$

where, $\sigma_y$ represents the yield stress of the workpiece material.

However, in Abaqus' FE platform, the limiting shear stress is defined as the point when the contact shear stress exceeds the limiting shear stress ($\tau_{max} < \mu * \sigma$ ), and sticking behavior is observed. Otherwise, sliding behaviour will take place for ($\tau_{max} \geq \mu * \sigma$ ) [47].

**Variable COF at tool-chip interface**

In the FE software, the co-efficient of friction can be defined as a function of output variables such as contact stress, temperature, and sliding velocity. Therefore, variable coefficient of friction based on these output parameters is applied to improve FE modelling capabilities.

High contact pressure acts on the cutting tool which influences the friction characteristics during machining. Amir et al. [48] characterized the friction behaviour based on contact stress ($\sigma_n$) acting on the cutting tool. The friction at the tool-chip interface can also be presented as a function of velocity or temperature. The change of friction coefficient ($\mu$) with respect to the sliding velocity was reported in different studies [49], [50]. J. Rech et al. [50] developed the friction model as a function of sliding velocity at different contact pressures, using a tribometer for various coated tools with different lubrications. J. Boyd et al. [51] proposed a temperature-dependent friction model based on the experimental result of a tribometer test for AISI 1045 steel with uncoated carbide. A significantly improved feed force prediction was observed.

Despite the detailed investigations prevalent in literature on the effect of COF on cutting simulation, a common standard in regards to calibrating the magnitude of COF to be used in FE cutting models is still lacking [27].

### 2.3.2 Thermal interaction

FE software enables the calibration of heat generated during machining. As such, it is important to understand the properties of thermal interaction involved in machining. During interaction between the tool and chip interface, the heat flux density generated is defined as:

$$q_f = \eta_f \tau_f \left(\frac{\Delta S}{\Delta t}\right) \quad (13)$$

where $\Delta S$ is an incremental slip on the tool-chip interface at a time increment $\Delta t$ and $\tau_f$ is frictional stress [44]. The $\eta_f$ is the percentage of energy converted to heat during frictional slip. Previous literature found the value of $\eta_f$ to be between 0.85-1 [42]. A very high GAP conductivity(500-1000 KW/m/K) was assumed in the literature [39], [27]. The fraction of heat ($\beta_H$) distributed into the tool and workpiece (chip) is usually calculated based on the material heat absorption capacity[42] .

$$\beta_H = E_w/(E_w + E_t) \quad (14)$$

$$E_{w,t} = \left(\rho_{w,t} * C_{p\,w,t}\ \ k_{w,t}\ \right)^{.5} \quad (15)$$

where,

$\beta_H$= the percentage of heat distributed to the workpiece, $E_{w,t}$ = Heat energy absorbed by the workpiece or the cutting tool, $\rho_{w,t}$ = density of the workpiece or the cutting tool ,$C_{p\,w,t}$ = Specific heat of the workpiece or the cutting tool, $k_{w,t}$ = thermal conductivity of the workpiece or the cutting tool.

## 2.4 FEA investigation on thermo-mechanical behaviour of machining

The primary goal of the Finite Element Model (FEM) is to predict difficult-to-measure thermo-mechanical properties at the cutting zone. The changes in thermo-mechanical properties due to process parameters such as speed, feed and edge radius are widely investigated in literature [52], [53], [3]. This study mostly focuses on the effect of edge radius in machining. The cutting-edge radius directly affects the temperature, stress, material velocity, as well as residual stress.

### 2.4.1 Cutting edge geometries

The microgeometry of the cutting edge can be symmetrical or asymmetrical. The characterization of the cutting edge is usually performed by the K factor method [4]. In this research, the cutting-edge geometries are characterized by four main parameters, $S_\alpha$, $S_\Upsilon$, $\bar{S}$ and $r_\beta$, as shown in Fig. 9. The $S_\alpha$ refers to segment of the flank face, $S_\Upsilon$ is segment of the rake face and $\bar{S} = (\frac{S\Upsilon + S\alpha}{2})$ and $r_\beta$ is edge radius. The ratio between $S_\Upsilon$ and $S_\alpha$ is defined as K factor. The edge radius bellow 5 μm is defined as a sharp tool.

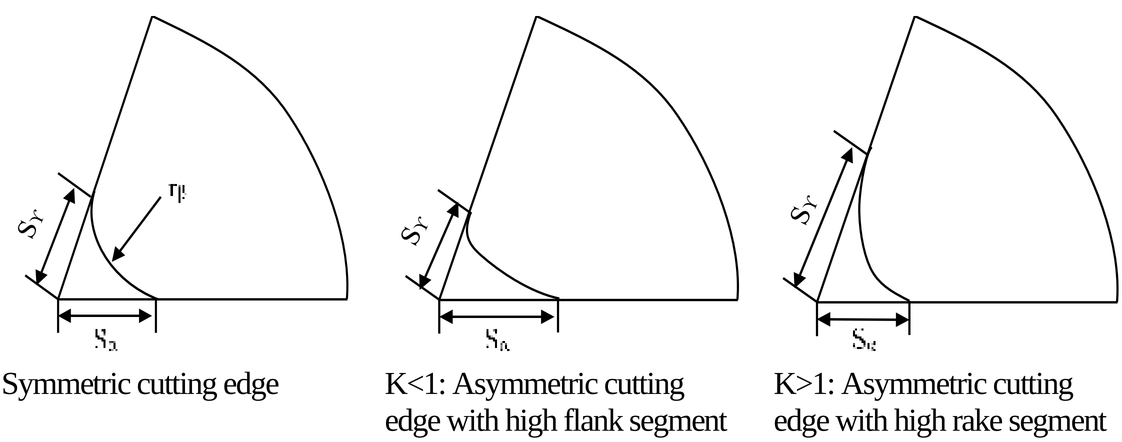


Figure 9: Cutting edge geometries characterizations

### 2.4.2 Effect of cutting edge on temperature

Increasing the size of the cutting edge radius results in an increased frictional contact area at the tool-chip interface [6]. Denkena et al. [54] numerically investigated the effect of micro edge geometry of the cutting tool in machining. It was observed that temperature in the cutting zone increases along with cutting-edge radius. During cutting, the maximum temperature is located at the rake face at a certain distance from the tool tip [55]. However, the ratio of uncut chip thickness (h) to edge radius ($\frac{h}{r\beta}$) determines the maximum temperature location in the cutting zone. With a constant uncut chip thickness, the maximum temperature shifts from rake face to flank face as the edge radius increases [56].. For an asymmetric cutting edge, the segment on the flank face ($S\alpha$) has major influence on the cutting temperature [6].The location of maximum temperature depends on size of $S\alpha$ and $S\Upsilon$ . The maximum temperature shifts to the flank face with increment of $S\alpha$, whereas the maximum temperature shifts to the rake face with the increment of $S\Upsilon$ [57].

Hosseinkhani et al. [44] numerically investigated thermo-mechanical properties during the course of a cutting tool’s lifetime. Their study showed that the average temperature in the cutting zone increased as the tool was worn out, and the maximum temperature shifted from the rake face to the flank face; see Fig.10. Similar behaviour of the worn tool was experimentally observed by Trigger et al. [58].

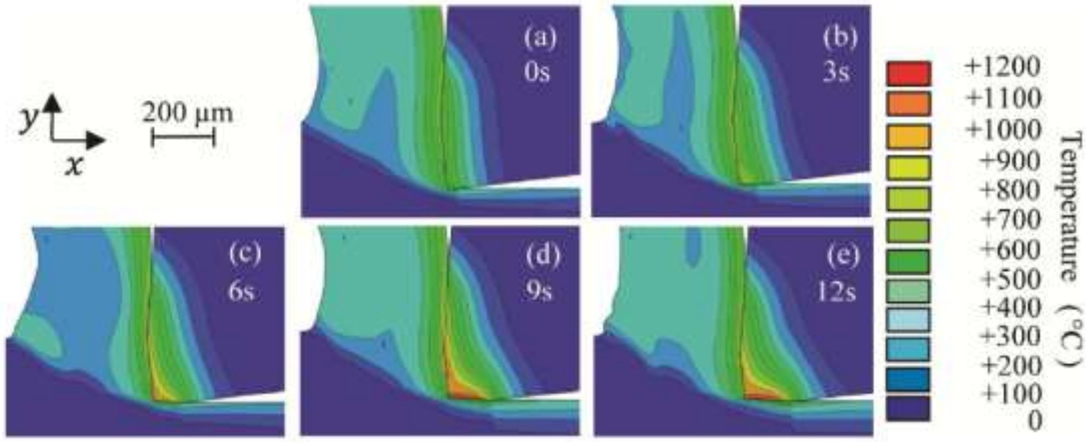


Figure 10: Change in temperature as the tool wears out. (reprinted with permission [38])

### 2.4.3 Effect of cutting edge on stress

An increase in edge radius contributes to mechanical stability. Edge rounding decreases the stress magnitude and concentration on the tool tip. Al-jkeri et al. [59] reported that compared to a sharp tool, the von Mises stress can be reduced by 4% with an edge radius of 27μm during the turning of 4142H. A similar reduction of effective stress on the tool tip achieved by an optimum edge radius was also recorded in literature [60], [53]. However, after a certain range of edge radius, the maximum effective stress value on the flank face increases with increment of the edge radius [59], [53]. This phenomenon happens due to increased contact of the cutting edge with workpiece and higher normal and friction forces [53]. The position of effective stress is primarily determined by the size of the flank edge, Sα [55].

An investigation of principle stress phenomena was performed with a round and chamfer tool during the machining of AISI H13 [61]. It was found that tensile stress was diminished by 25% while using the chamfered tool. Similar behaviour was observed in case of machining of 4140 steel [7]. It was found that the maximum principal stress (tensile) was reduced by 20% and by 30% by using a chamfer tool and a worn tool respectively.

### 2.4.4 Effect of cutting edge on material velocity

The design of the cutting tool highly influences the material flow in front of the tool tip. The uncut chip thickness (h) to edge radius ratio ($\frac{h}{r\beta}$) defines the chip formation behavior. With a constant uncut chip thickness, an increase in edge radius will cause ploughing and severe plastic deformation adjacent to the tool tip [25], and deformed material will be pushed underneath the flank surface, reducing the material velocity and causing the material to adhere to an area on the cutting tool known as the stagnation zone. A larger area of the stagnation zone is found at a greater edge radius [42] and chamfered edged cutting tool [6], as seen in Fig. 11. It was reported that the higher deformation due to the increased edge radius leads to high cutting and feed forces at a constant feed rate [3].

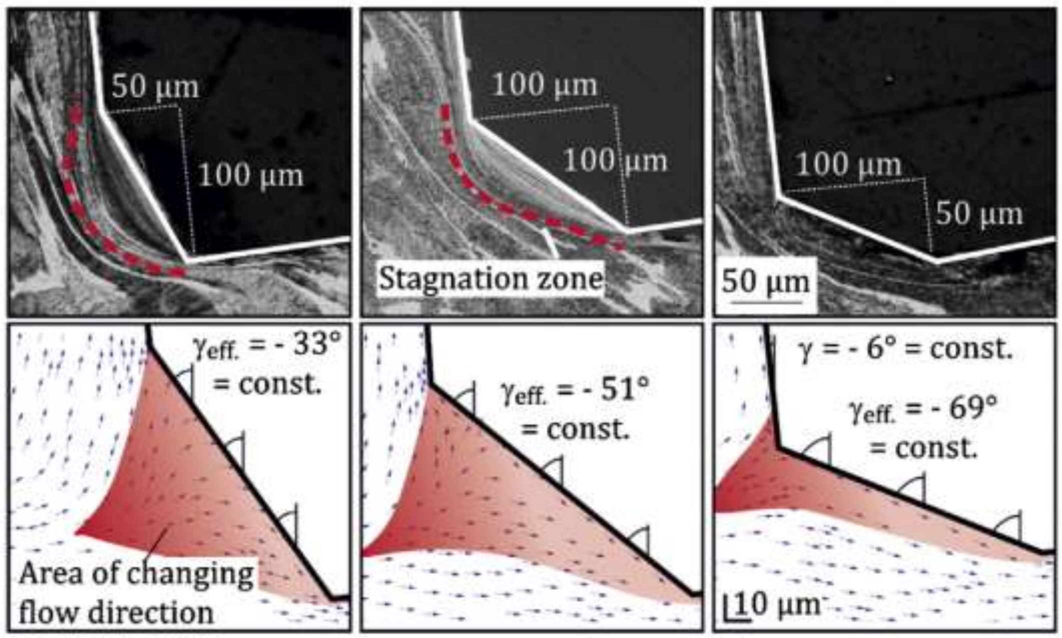


Figure 11: a) Material flow behavior for chamfered tool (reprinted with permission [1])

Although several investigations on the influence of edge geometry on the thermo-mechanical behavior of the cutting tool have been done by FEA, research relating these investigations with experimental tool wear results is still lacking.

## 2.5 Tool wear

Tool wear represents the continuous failure of the cutting tool during machining. The wear can be characterized based on the measurement technique and wear mechanism.

### 2.5.1 Tool wear measurement

The measurement of flank wear is straightforward. The width of the flank wear is measured under a microscope. An increase in flank wear results in the tool rubbing against the machined surface, which affects the dimensional accuracy and surface roughness of the finished product. The increment in flank wear also leads to an increase in normal cutting forces. The maximum flank wear for a standard tool life is 300-400µm [62].

Although the width of wear is visible on the rake face, the wear progresses in the depth direction, which is known as crater wear and is difficult to measure. The progress of crater wear weakens the cutting tool, which ultimately results in catastrophic tool failure. The groove of crater wear can sometimes work as a chip breaker.

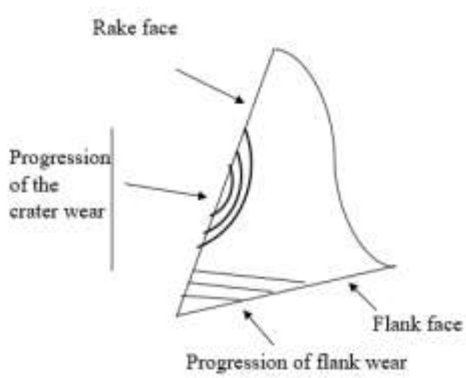


a)

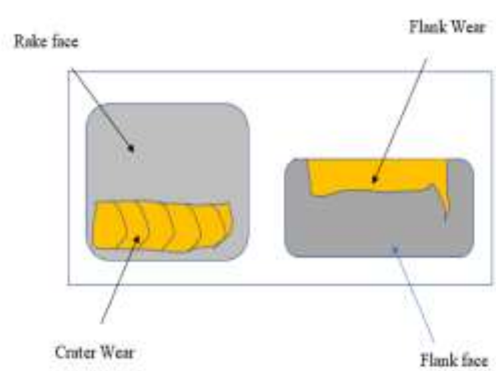


b)

Figure 12: a) 2D schematic view of different tool wear progression b) location of tool wear in the insert

### 2.5.2 Tool wear mechanism

The wear pattern on the rake and flank faces depends upon the types of wear mechanisms induced by the tool-workpiece interaction. The evolution of thermo-mechanical properties in the cutting zone represents the wear mechanism during machining. The wear mechanism varies depending on the combination of tool and workpiece. There are four primary wear mechanisms found during machining:

**Adhesion**: This type of tool wear is prevalent on the rake and flank face. The adhesion wear mechanism mainly relates to the friction behaviour of the tool-chip interface. Friction between the tool-chip interface causes the asperity junctions to weld to each other. The welded junction fractures once it reaches the critical zone. With the fracture of the asperity junction, fragments of the tool material are torn apart, wearing out the tool. Adhesion-related wear volumes are typically smaller relative to abrasion.

**Abrasion**: Abrasive tool wear refers to grooving of the tool face by hard abrasive particles present in the workpiece material. Sand particles in casting, carbide inclusions in steel, silicon particles in Al-Si alloys and strain-hardened built-up edge (BUE) fragments are examples of such abrasive particles. Abrasive wear is predominant on the flank face.

**Diffusion**: The movement of atoms from a high to low concentration in a metallic crystal lattice is known as diffusion. At the position of the higher temperature, tool and workpiece material diffuse into each other, resulting in wear. The rate of diffusion wear increases exponentially upon a growing thermal load (temperature). Diffusion wear occurs predominantly on the rake face. For example, during the machining of Ti-6Al-4V, the cutting tools mostly experience diffusion wear.

**Oxidation**: This wear is caused by oxidation of the tool binder material. It occurs near the free surface where severe wear is localized at the location of the maximum depth of cut. Oxidation wear causes depth-of-cut notch wear.

## 2.6 Tool wear modelling

Experimental measurement of tool life and analysis of the tool wear mechanism is a laborious, time consuming and costly procedure. If both tool life and tool wear can be predicted, the numerical estimation can mitigate the costs.

**Tool life model**

This type of model represents the relationship between the tool life and the cutting parameters. The well-known Tylor's tool life equation is expressed as follows:

$$\mathrm{T}V^{\frac{1}{n}}t^{\frac{1}{m}}b^{\frac{1}{l}} = C \qquad (16)$$

which is a function of the cutting speed (V), feed rate (t), depth of cut (b) and several constants (C, n, m, l). The constants are obtained from the experimental tool wear data for a given combination of tool and workpiece material.

**Tool wear rate model**

The wear rate models were developed based on the wear mechanism observed in a specific cutting process. These models represent the relation between the rate of volume loss on the rake and flank faces and cutting process variables. The cutting process variables must be experimentally determined.

Takeyama and Maruta [63] proposed a two-part tool wear model based on the effects of both abrasive and diffusion wear. The first part characterizes the abrasive wear as a function of speed and feed rate, while the second part shows that the diffusion wear depends exclusively on the temperature of the tool interface.

$$\dot{w} = AVs + B\exp\left(-\frac{E}{RTint}\right) \qquad (17)$$

Usui's model was established based on a diffusion wear mechanism. However, it gives a good prediction for both abrasive and diffusion wear [64]. This model incorporates the effects of contact pressure ($\sigma_n$), sliding velocity ($V_s$) and interface temperature (T) on the wear behaviour into the single following expression:

$$\dot{w} = A\,6n\,Vs\exp\left(-\frac{B}{Tint}\right) \qquad (18)$$

Attanasio et al. developed a combined model to efficiently increase the tool wear prediction accuracy [65]. Eqn. 19 represents the combined wear model, where D is a polynomial function of the material:

$$\dot{w} = A\,6n\,Vs\exp\left(-\frac{B}{Tint}\right) + D\exp\left(-\frac{E}{RTint}\right) \qquad (19)$$

The models can be summarized as follows:

Table 1: Tool wear analytical models

| Tool life model | Tool wear rate models |
|---|---|
| Tylor's tool life model<br>$$TV^{\frac{1}{n}}t^{\frac{1}{m}}b^{\frac{1}{l}} = C$$<br>where<br>T= tool life, V= material velocity, t= uncut chip thickness, b= depth of cut and n,m,l are cutting parameter constants. | Maruta and Takeyama<br>$$\dot{w} = AVs + B \exp\left(-\frac{E}{RTint}\right)$$<br>Usui<br>$$\dot{w} = A\,6n\,Vs \exp\left(-\frac{B}{Tint}\right)$$<br>Attanasio Model<br>$$\dot{w} = A\,6n\,Vs \exp\left(-\frac{B}{Tint}\right) + D \exp\left(-\frac{E}{RTint}\right)$$<br>where<br>$\dot{w}$ = wear rate, $6n$ = normal stress,<br>$Tint$ = interface temperature, Vs = sliding velocity.<br>R= Universal gas constant and A, B, D are experimental constants. |

### 2.6.1 Model calibration

The proper calibration of the tool wear model is essential, since the accuracy of the tool wear prediction depends solely on the calibrated constants. Usui et al. [66] calibrated the wear model using temperature and contact stress determined during different sets of orthogonal turning experiments.

Finite element modelling is one of the most effective ways of predicting the temperature and contact stress, since it allows tool wear models to be calibrated without expensive and labour -intensive procedures. Obtaining temperature, stress and velocity profile from the simulation and tool wear value from the experiment is known as the hybrid calibration method. This method has gained popularity among recent researchers [11], [20], [48], [67].

### 2.6.2 Tool wear prediction

Once the wear model constants are found, tool wear can be predicted from the thermo-mechanical properties found at different stages of tool wear. Therefore, it is important to achieve a worn tool geometry at each tool wear stage. An early pioneer of this approach, Yen et al. [19] introduced the mathematical concept of tool wear prediction based on the numerical simulation of the worn tool. The worn geometry was predicted by the individual nodal displacement method. With this method, the nodes on the cutting edge were displaced inward to the tool, normal to the neighboring nodes, based on the calculated wear rate value, see Fig. 13(a). Later, a number of studies were conducted to predict tool wear using the same method [68], [69], [65]. Since it is difficult to maintain a uniform wear rate value for each node due to the highly dynamic nature of the simulation, this method creates a zig zag profile of the worn tool. Therefore, an extra boundary smoothing function is needed to yield a uniform shape of the cutting tool [68], see Fig. 13(b).

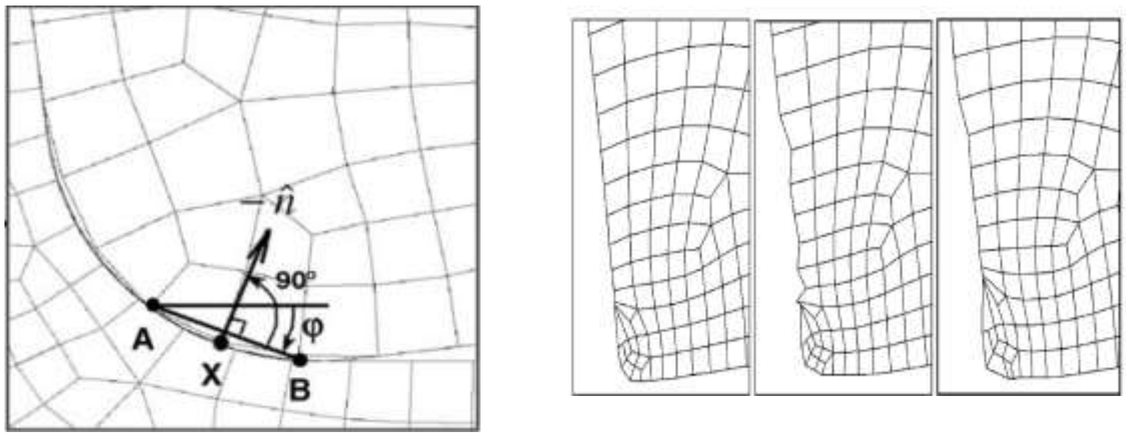


a) b)

Figure 13: updating of cutting edge by nodal displacement method (reprinted with permission [67])

Instead of updating the cutting tool based on nodal displacement method, Binder et al. [70] proposed a displacement vector near the tool tip, tangential to the machined surface (see Fig. 14). This displacement vector was updated normal to the machined surface for each time increment. This method was able to capture the flank wear trend with a fair degree of accuracy.

Malakizadi et al. [48] updated the Usui tool wear equation based on the flank geometry retrieved from the experiment .Tool wear prediction was found to be significantly improved. Hosseinkhani et al. [11] calibrated different tool wear equations using the experimentally measured worn tool. The latter study could model different wear mechanisms using numerical data from the simulation. Both studies observed that the worn tool geometry resembles a chamfered edge.

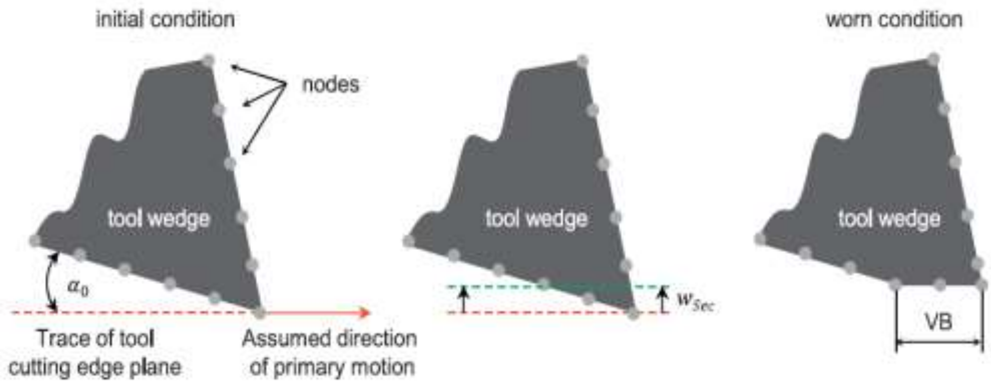


Figure 14: Updating of cutting edge based on assumed displacement vector (reprinted with permission [70])

The prediction of tool wear still requires significant research to obtain higher tool wear prediction accuracy with less computational time. Additionally, a more accurate worn tool geometry prediction method must be obtained by reducing modelling error.

## 2.7 Modelling of coated tools

Tool coating can significantly enhance machining quality by serving as a thermal barrier and strengthening wear resistance of tools [23]. The FEM modelling of machining with coated tools has been proposed in order to gain better understanding of the effect of coating on the tool performance [24], [14], [23], [71].

W. Grzesik et al. [24] used commercial AdvantEdge FE code to investigate the effect of different coating layers on the average and peak interface temperature. It was found that a coating layer reduced the maximum temperature on the tool surface. The simulation result showed a reasonable agreement with the experimental temperature measured by thermo-couple. F. Kone et al. developed a finite element model in the DEFORM 2D platform to investigate the thermo-mechanical behaviour of a coating under extreme contact loading in dry machining [52]. It was observed that coating with different layer thicknesses reduced thermal load on the substrate. However, the number of coating layers had insignificant effect on the substrate temperature and the coating showed a negligible effect in terms of contact pressure on the cutting tool. In addition, the coated tool showed reduced cutting forces because of a reduced co-efficient friction of the coating. Similar investigations were performed by others [14], [72], [73]. The influence of hard coatings on a milling tool was investigated by I. Krajinović [23]. This study was developed in an ABAQUS/EXPLICIT environment. The coating properties were defined in the elements adjacent to the workpiece. The tool substrate was designed as a plastic body. The study was able to show the influence of the different hard coatings on the plastic deformation of tool substrates.

Many papers discuss the effect of coating properties on the thermo-mechanical behaviour of the cutting process. A few studies have been performed to improve the technique of applying a coated tool in FEM. More research is required for the geometrical optimization of a coated cutting edge to yield better tool performance.

# CHAPTER 3. FE SIMULATION OF ORTHOGONAL CUTTING.

Machining refers to many complex cutting operations which are often difficult to model. However, orthogonal cutting theory can be applied to most of them. In the experimental set-up, the width of cut was more than 10 times of uncut chip thickness which provides insignificant deformation in the direction of width of cut .Therefore, a 2D orthogonal thermo-mechanical FE model with a plain strain element type was developed with FE ABAQUS/Explicit version 2018 to represent the actual experimental cutting mechanism. A standard FE modelling procedure was followed for developing the FE model. A plain strain, quadrilateral, linearly interpolated and thermally coupled (CPE4RT) element was used for the modelling. Coupled temperature-displacement analysis was performed. The following assumptions were made to simplify the model:

a) Chip formation is continuous. Discontinuous or segmented chips were not simulated.
b) The influence of workpiece microstructure was not considered.
c) The radiation and convection heat transfer were ignored.
d) Initial chip thickness was assumed for the ALE formulation, but it doesn’t affect the final chip shape.

Three formulation methods were simulated and validated with the experimental result. The validation test was performed in terms of cutting force and feed force. The ALE formulation approach was selected for future study because it is time-efficient and able to predict the feed force with a finite edge radius.

## 3.1 FE formulations

Three formulation methods were developed to simulate metal cutting. Each formulation method has different meshing technique. Meshing refers to the practice of creating a subdivision of a continuous geometry body into discrete cells. Proper meshing in metal cutting simulation helps to avoid mesh distortion and large computational time.

### 3.1.1 Updated Lagrangian (UL)

Fig.15 shows the meshing technique and boundary conditions for the Updated Lagrangian formulation. Cutting velocity was assigned to the cutting tool and the workpiece was fixed in both the x and y-axes. The workpiece was divided into three segments. The upper portion represents the uncut chip thickness or chip load (f). The material of this layer will be plastically deformed, and the chip will form by itself.

A very fine mesh was assigned in uncut chip thickness. The mesh convergence was performed in terms of mesh size assigned in uncut chip thickness. The chip layer was designed with an inclination angle of 25 degrees. This inclination angle was implemented to avoid element distortion. A sacrificial layer was assigned in the middle segment. The Johnson-Cook damage parameter was assigned to this layer. The sacrificial layer thickness depends upon the edge radius of the cutting tool. The thickness of the sacrificial layer should be large enough to avoid element distortion. It was found that if the sacrificial layer is not thick enough compared to the edge radius, elements of the sacrificial layer subjected to high compressive stress will eventually deform the elements and terminate the simulation [33].

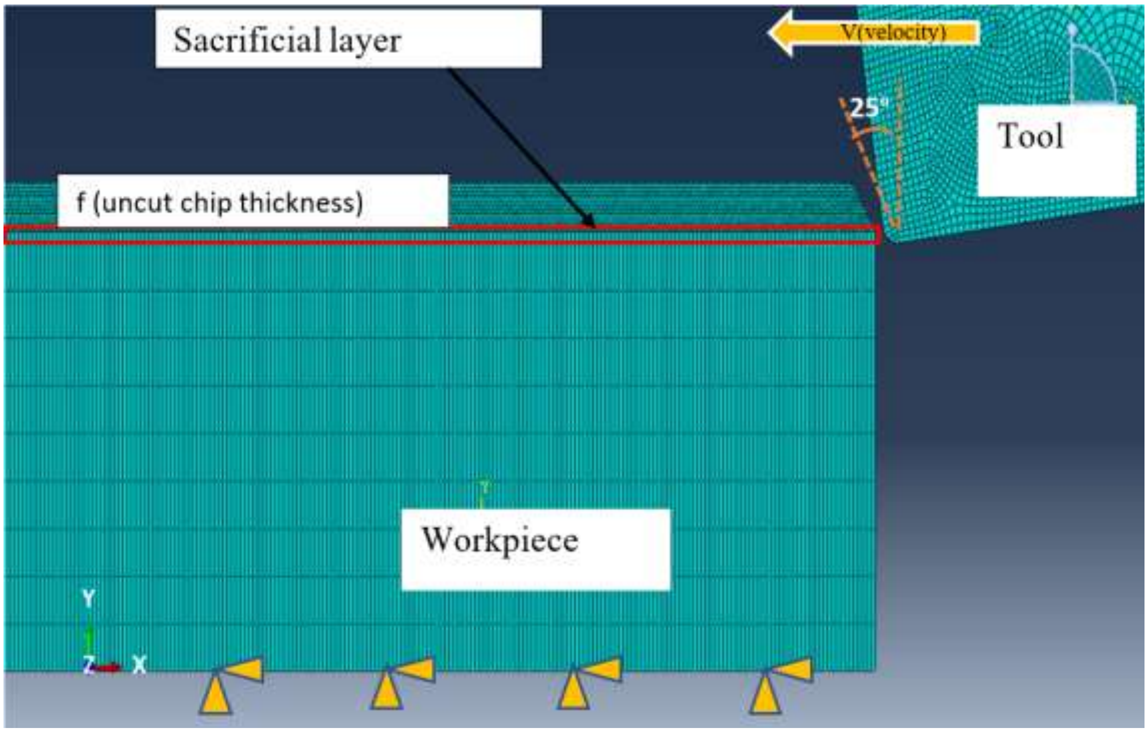


Figure 15: Mesh discretization of Updated Lagrangian technique

### 3.1.2 Coupled Eulerian-Lagrangian

Meshing of the coupled Eulerian-Lagrangian (CEL) method is identical to the Updated Lagrangian simulation model. The workpiece in the CEL formulation acts as a Eulerian body. The Eulerian body was filled with material up to the height of h using volume fraction coding in the FE software. Although the model was built in a 3D environment, it was kept close to the plain strain condition by setting the z axis constraint and workpiece width at least ten times larger than the feed rate. The Eulerian body was fixed in both the x and y-axes, and the chip was formed as the cutting tool moved in the negative x-axis at the given cutting velocity. Fig. 16 shows the boundary condition for the CEL approach. No initial chip thickness assumption was needed. Also, the sacrificial layer was not required in this approach. According to Ducobu et al. [74], the workpiece element size should be at least half of the edge radius. The cutting-edge radius for the tool is 35µm, and the minimum workpiece element size was maintained at 5µm by performing mesh convergence, which will be discussed later on. It has been suggested that the cutting tool should be inside the Eulerian body to minimize the computational time [74].

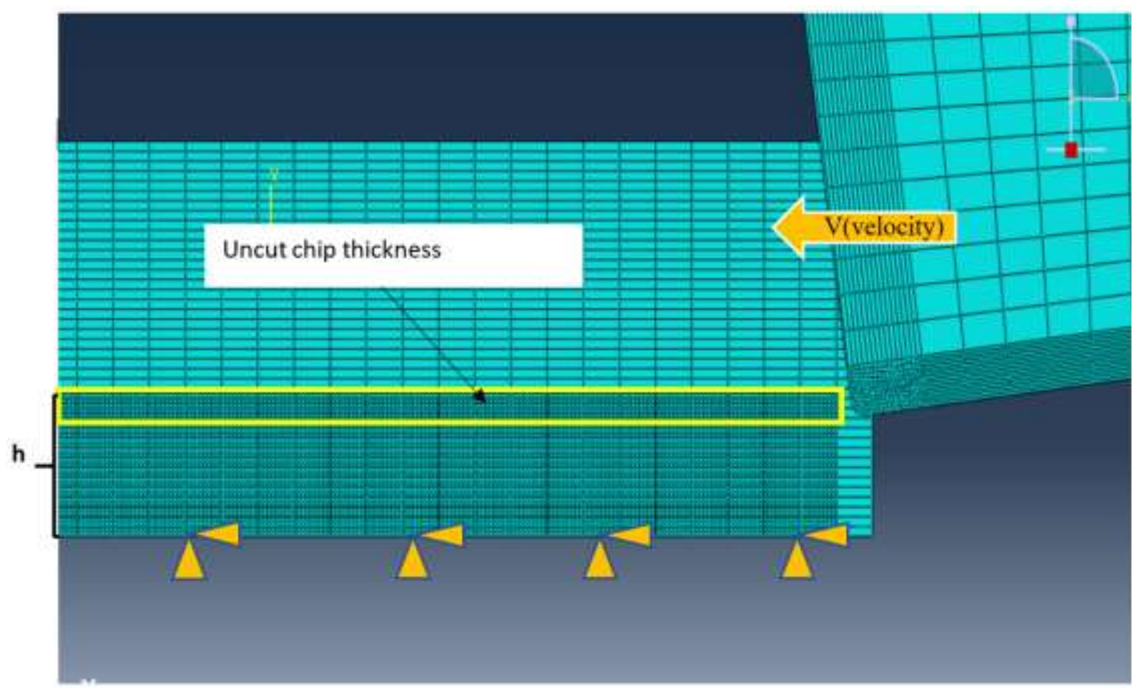


Figure 16: Mesh discretization of CEL method

### 3.1.3 Arbitrary Eulerian-Lagrangian

The ALE modeling was developed in a 2D environment based on the theory of orthogonal cutting. The cutting tool was fixed in both the y and x-axes. The workpiece was constrained in the y-axis having the cutting velocity in the x-axis. An initial chip thickness (t) was assumed in the workpiece to be such that the chip was able to grow uniformly, but did not have any influence on the final chip thickness [27]. The corner radius, as shown in Fig.17, has been applied to control the element distortion. Similar to the initial chip thickness, corner radius did not affect the simulation output result.

The mesh discretization of ALE was performed very carefully. The workpiece in front of the cutting tool (zone B) was kept as a Eulerian body, where the mesh was fixed but the material could flow through it. The element deformation was controlled because of this Eulerian body. The right (Zone C) and the left region mesh (Zone A) of zone B were fixed in the y-axis only. This allowed the simulation to remain stable as the chip was being formed. The other regions (Zone D) were kept pure Lagrangian so that the chip could grow itself. Mesh refinement was performed at the tool chip interface.

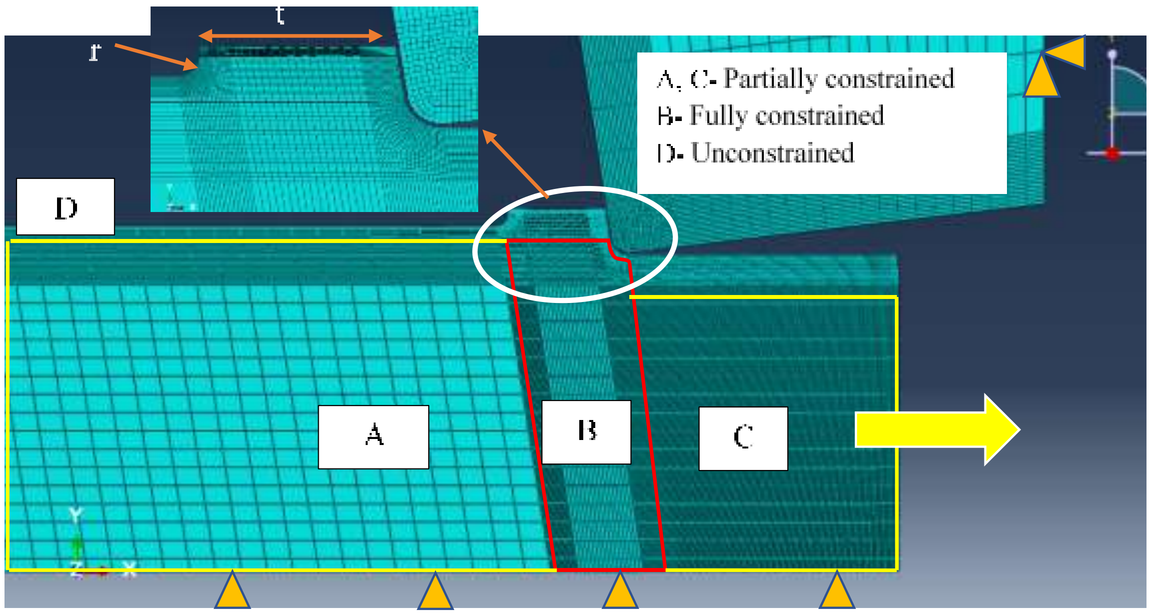


Figure 17: Mesh discretization of ALE formulation

## 3.2 Material modeling

The metal removal process involves very large plastic deformation with very high strain rate and high temperature. The strain rate is nearly $10^6$ $s^{-1}$. Simulating metal cutting is challenging for this kind of dynamic behaviour. To simulate metal cutting, it is necessary to have a material model developed at a higher strain rate and temperature. The Johnson-Cook material model seems to be the most applicable material model for the metal cutting simulation. The Johnson-Cook material model is shown in Eq. (20).

$$\sigma_{eq} = [A + B\varepsilon_P^n]\left[1 + C\,ln\left(\frac{\dot{\varepsilon}_p}{\dot{\varepsilon}_{p_0}}\right)\right][1 - (T^*)^m] \qquad (20)$$

Where,

$\sigma_{eq}$ = Equivalent plastic flow stress.

A = Initial plastic flow (yield) stress

B = Coefficient of strain hardening

n = Strain hardening exponent

C= Strain rate dependency coefficient

$\bar{\varepsilon}_p$ = Equivalent plastic strain

m = Thermal softening index

$\dot{\bar{\varepsilon}}_p$ = Equivalent plastic strain rate

$\dot{\bar{\varepsilon}}_0$ = Reference plastic strain rate

T = Current Temperature

$T_r$ = Room temperature

$T_m$ = Melting temperature

In this research two different kinds of workpiece materials were used. The AISI 1045 was used to validate the developed FE model. The AISI 4140 was used for rest of this study. The cutting tool was modelled as cemented carbide material. The Johnson-Cook parameter values used to simulate the behaviour of the AISI 1045 and AISI 4140 workpiece are specified in Table 2 and 3.

Table 2: Johnson-Cook material parameters for AISI 1045[75]

| ***A (MPa)*** | ***B (MPa)*** | ***C*** | ***n*** | ***m*** |
|---|---|---|---|---|
| 553.1 MPa | 608.1 MPa | 0.0134 | 0.234 | 1 |

Table 3: Johnson-Cook material parameters for AISI 4140 [76]

| ***A (MPa)*** | ***B (MPa)*** | ***C*** | ***n*** | ***m*** |
|---|---|---|---|---|
| 612 MPa | 436 MPa | 0.008 | 0.15 | 1.46 |

The damage property used in the updated Lagrangian formulation was selected from the literature [77]. In actual machining, the deformation in cutting tool compared to workpiece material is negligible. Hence, the cutting tool was considered as an elastic body.

Table 4: Material properties for AISI 4140, AISI 1045 steel and uncoated carbide

| **Material parameter** | **Units** | **Workpiece (AISI 4140)**[78] | **Workpiece (AISI 1045)**[79] | **Cutting tool (uncoated carbide)**[78] |
|---|---|---|---|---|
| Density | Kg/m$^3$ | 7,800 | 7870 | 15,290 |
| Young's modulus, E | GPa | 210 | 200 | 560 |
| Poisson's ratio, ν | - | 0.3 | 0.3 | 0.23 |
| Yield strength | MPa | 415 | 310 | |
| Tensile strength | MPa | 655 | 565 | |
| Specific heat capacity | J/kg°K | 473@200ºC | 220 | 178 |
| | | 519@ 400ºC | | |
| | | 561@600ºC | | |
| Thermal expansion coefficient, α | μm/m°K | 12.2 @ 20ºC | 10.0@ 20ºC | 7.1 |
| | | 13.7 @ 250ºC | 12@200ºC | |
| | | 14.6 @ 500ºC | 15.3@600ºC | |
| Thermal conductivity | W/m°K | 42.6 @ 20ºC | 52@0ºC | 24 |
| | | 42.3 @ 200ºC | 51@100ºC | |
| | | 37.7 @ 400ºC | 38@500ºC | |
| | | 33.0 @ 600ºC | 30@700Cº | |
| Melting temperature, $T_m$ | °K | 1709 | 1793 | 2800 |
| Bulk Temperature, $T_r$ | °K | 300 | 298 | 300 |

## 3.3 Contact properties

The combination of the Coulomb's and shear friction model was used to model the interaction at the tool-workpiece interface and is given in eq. (21).

$$\tau_f = min(\mu\sigma_n, \tau_{max}) \qquad (21)$$

where,

$\tau_f$ : frictional stress
$\mu$ : coefficient of friction
$\sigma_n$ : normal stress
$\tau_{max}$: limiting shear stress($= \frac{\sigma_y}{\sqrt{3}}$)
$\sigma_y$ : uniaxial yield stress

The limiting shear stress ( $\tau_{max}$) for AISI 1045 and AISI 4140 was calculated as 180 MPa and 240 MPa respectively .A coefficient of friction μ=0.15 was used to simulate AISI 1045 steel according to the literature [80]. In the case of AISI 4140, the COF μ was calibrated with measured experimental forces, which will be discussed later.

The percentage of energy converted to heat during frictional slip was considered as $\eta_f$ = 0.9 [42]. The gap conductivity between the workpiece and the cutting tool was applied according to the literature as 1000 $W/m^2/^oC$ [17]. The fraction of heat ($\beta_H$) distributed to the workpiece (chip) is calculated as 0.53 for AISI 1045 and 0.67 for AISI 4140 steel.

## 3.4 Cutting conditions

To validate the developed simulation model, the cutting force from orthogonal machining of 1045 steel was taken from the literature [80]. The following cutting conditions were used for the experimental set up of orthogonal machining with the simulation being performed according to them.

| **Cutting conditions** | |
|---|---|
| Tool | |
| Edge radius (µm) | 30 |
| Rake angle | -9 |
| Clearance Angle | 7 |
| Workpiece | |
| Disk diameter (mm) | 100 |
| Disk width(mm) | 3 |
| Plunging depth(mm) | 17.5 |
| Cutting fluid | Dry |

## 3.5 Mesh convergence test

The mesh convergence test is a method to find a time-efficient FE model without compromising modelling accuracy. Element size has a significant effect on the prediction of cutting force and temperature for the metal cutting simulation [74]. In all the proposed computational models, the mesh convergence tests were carried out on the basis of the force result. For example, figure 18 shows the mesh convergence in a CEL formulation. The magnitude of cutting force variation was tested at different element sizes. When the element size reached 20μm, a higher fluctuation in force magnitude (standard deviation of 3.5% from mean value) was observed. As the element size decreased, the fluctuation in cutting force reduced as well. At 5 μm and 2.5 μm, the force variation was not significant (less than 1.52% of standard deviation from mean value).

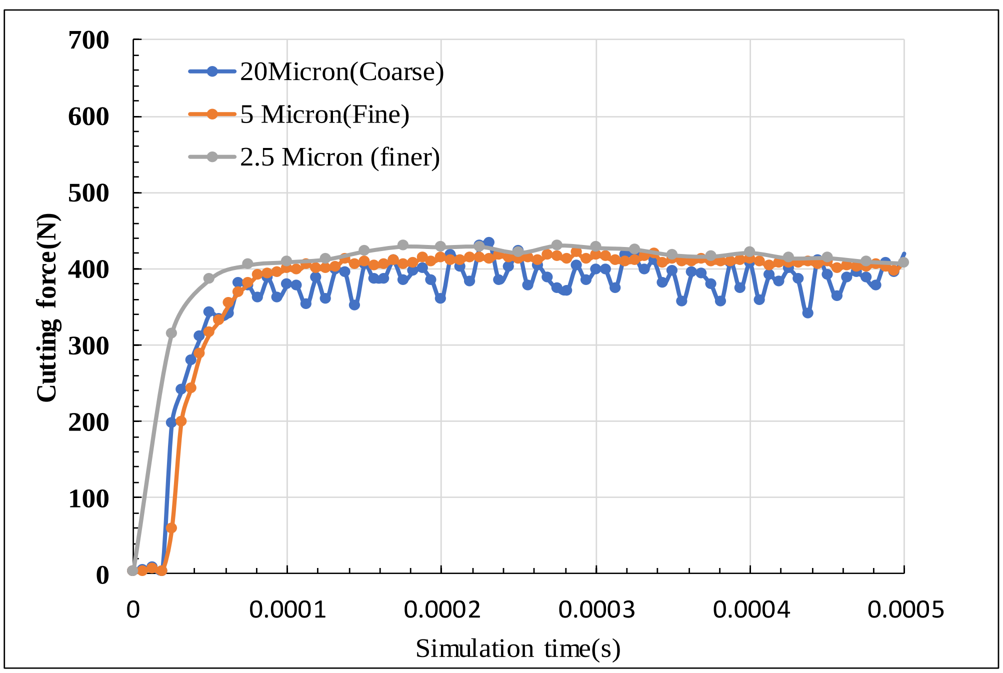


Fig. 18: Mesh convergence test in CEL with different element size, S=150 m/min, f =.05mm/rev

An element size of 2.5µm required greater computation time than 5µm. Therefore, a 5 µm element size was recommended for further analysis.

## 3.6 Comparative study of formulation techniques

A comparison was made among the three most commonly used formulation methods (UL, ALE, CEL), based on time efficiency. Fig. 19 shows the comparison of computational time for the three different formulation methods. A constant step time (2e-9) was used for all three approaches with the same computer configuration. Computational time was considered when both the temperature and the cutting force became stable. The updated Lagrangian required the least amount of computational time to achieve a stable simulation result. ALE took a little longer but CEL was the longest out of all formulations.

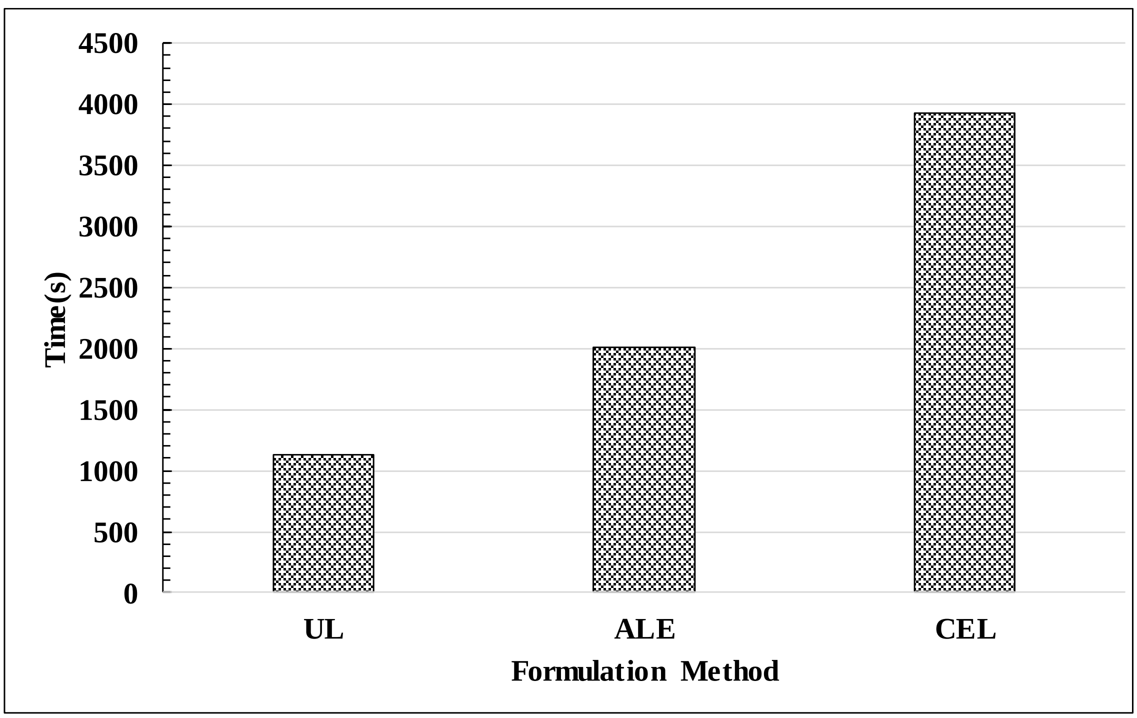


Figure 19: Comparison of computation time of formulation methods at S=150 m/min f=.05mm/rev

An ALE sample chip formation simulation is presented in Fig 20. Fig. 21 shows the graph of the calculated cutting and feed forces. The cutting forces are collected as a sum of reaction forces in the cutting tool nodes. It was observed that cutting force becomes stable after 450μs. The following results were collected at a cutting speed of 150 m/min and a feed rate of .07mm/rev.

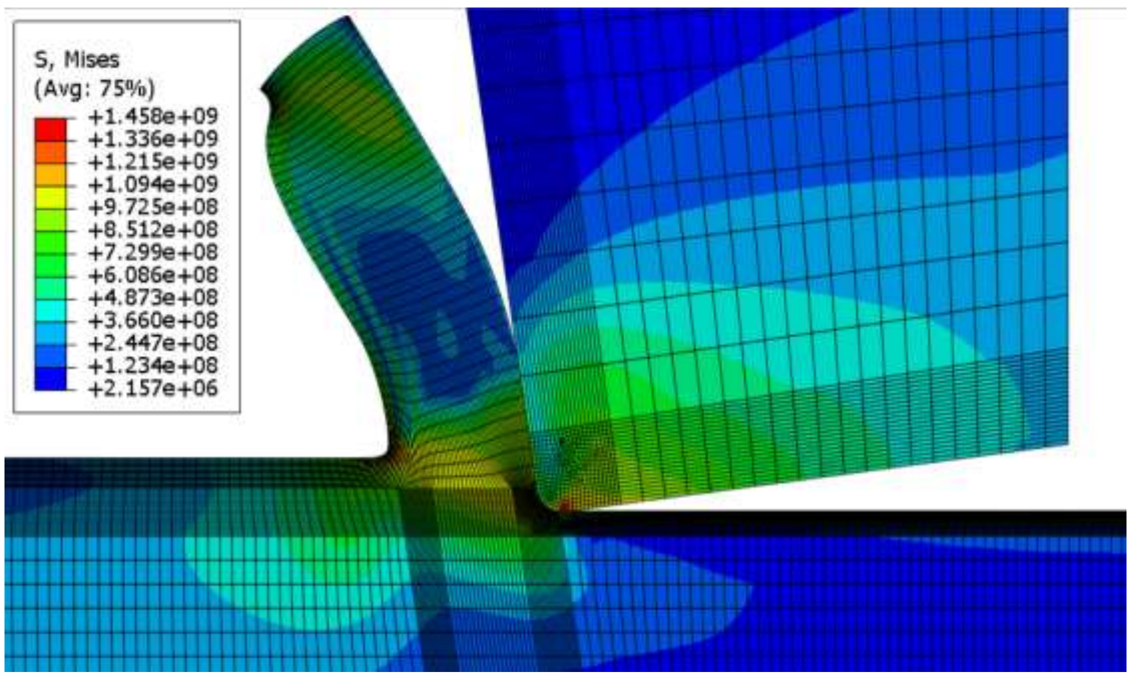


Figure 20: ALE sample simulation result of chip formation, S=150 m/min, f=.07mm/rev.

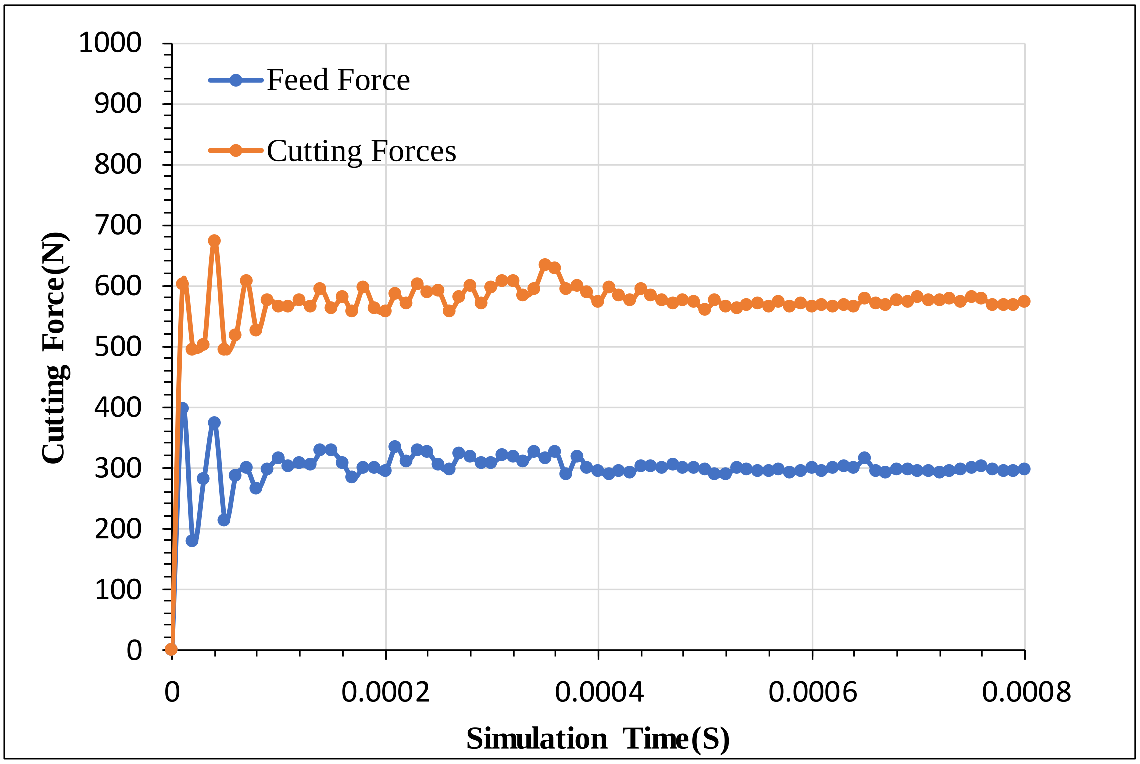


Figure 21: The change in cutting forces with simulation time, S=150 m/min, f=.07mm/rev

The validation was performed in terms of cutting force ($F_c$) and feed force ($F_t$) at three different formulations and three different feed rates.

| | |
|---|---|
| Cutting speed(m/min) | 150 |
| Feed rate(mm/rev) | 0.05,0.07,0.1 |

Cutting forces were measured in the simulation as an average value of stabilized readings. The cutting speed was 150 m/min, which remained constant throughout the measurements. The simulated cutting force results showed a good agreement with experimental cutting forces, with a maximum error of 6.7% in all three formulation methods, see Fig 22.

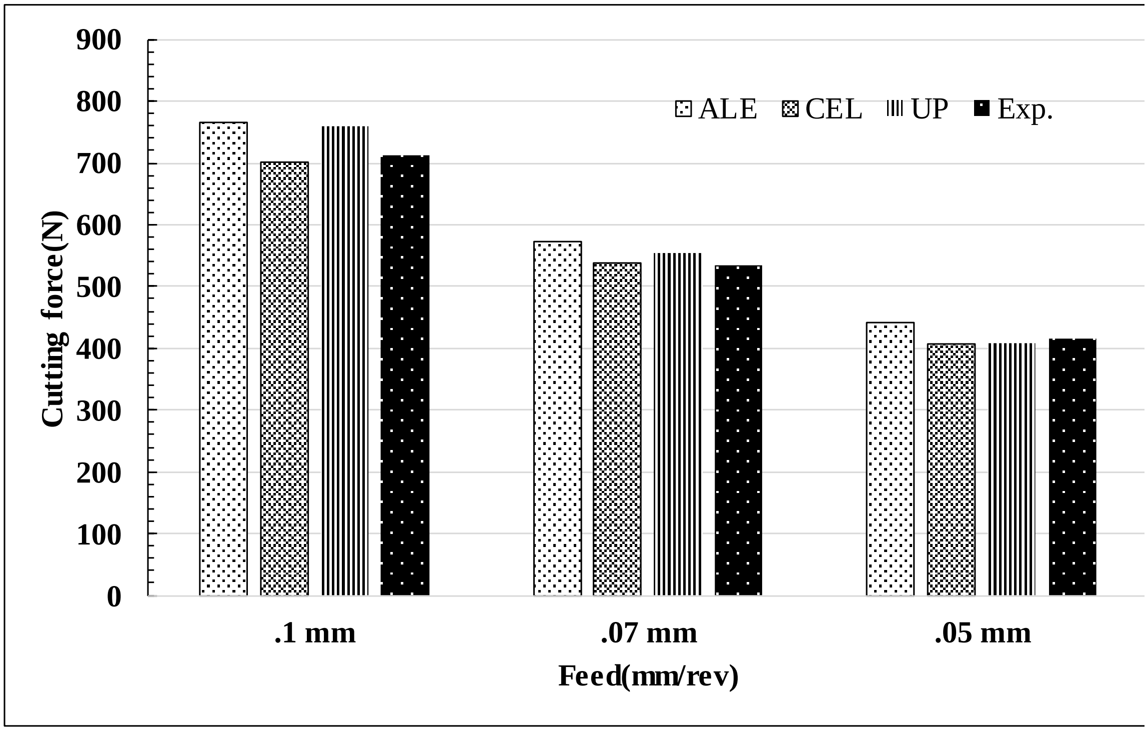


Figure 22: Cutting force validation with experimental result, S=150 m/min

The predicted feed force agreed less with the experimental result than the cutting force in all three formulation methods. The UL formulation showed a maximum prediction error of 49%. It has been argued that the sacrificial layer used in UL reduces the feed force [27]. The feed force prediction errors were recorded as 18% and 26% for ALE and CEL respectively. It was also reported by Ducobu [45] that ALE and CEL feature almost identical force predictability. In case of simulating AISI 1045, up to 45% of feed force prediction error was reported using ALE formulation [49]. High prediction error of feed force has always been a challenge while simulating orthogonal cutting in Abaqus [49], [51].

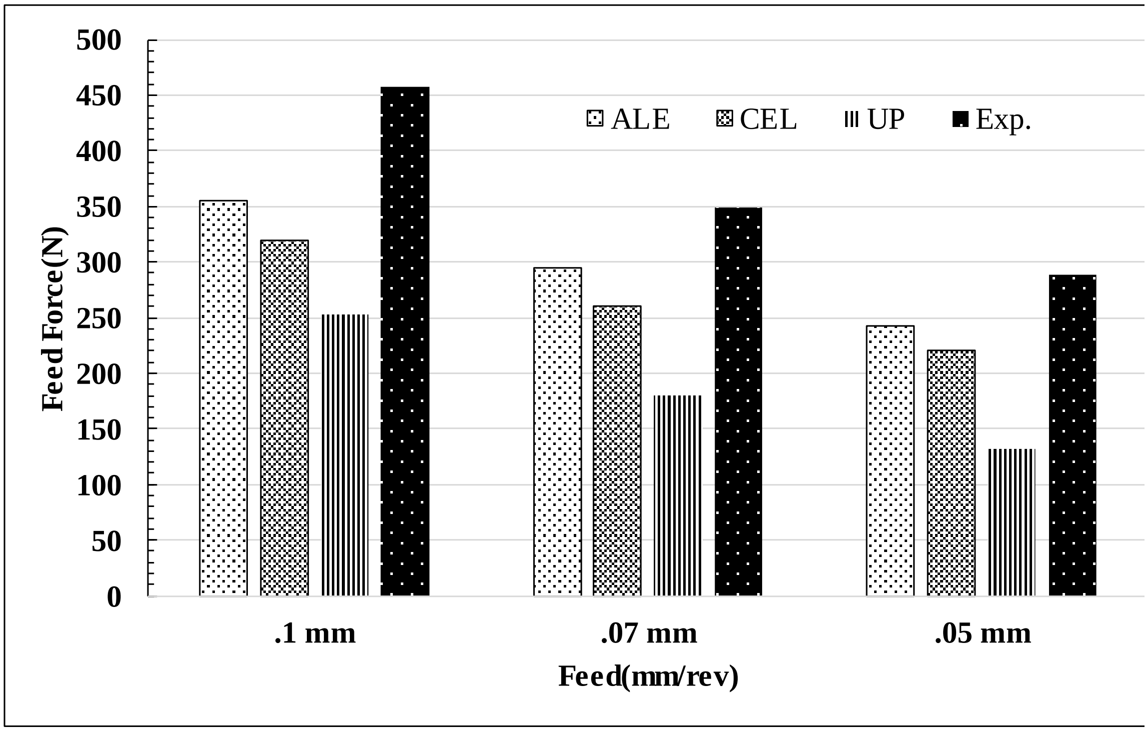


Figure 23: Feed force validation with experimental result, S=150 m/min

Table 5: Percentage of error for force prediction

| | UL | CEL | ALE |
|---|---|---|---|
| Cutting force | 3.9% | 1.03% | 6.7% |
| Feed force | 49% | 26.1% | 18% |

Out of the three formulation methods, one was selected for future study based on the analysis of the current investigation and previous work reported in literature. Although UL was the most time-efficient, it was also the least accurate in predicting feed force. UL also requires an additional sacrificial layer and is unable to predict valuable information such as ploughing, stagnation zone and size effect near the tool tip. In comparison, the CEL method yielded better accurate prediction of feed force than UL but was time-consuming. The ALE formulation was found to have an optimal balance between feed force prediction and computation time. The computation time of ALE was slightly higher (a few extra minutes) than UL. ALE can predict the material stagnation zone for different cutting-edge geometries [42] and is widely used to predict the thermo-mechanical behaviour at the tool-chip interface [44].

Investigations of cutting force, feed force, temperature, stress, and material velocity were carried out in the current work for different cutting-edge configurations. In conclusion, the ALE method is recommended for further studies in this field.

# CHAPTER 4. THERMO-MECHANICAL BEHAVIOUR OF EDGE GEOMETRIES

This chapter presents a detailed study of thermo-mechanical conditions in differently prepared tools as well as a worn tool. The thermo-mechanical behaviour of prepared edges was compared with an unprepared cutting edge. The experimental results of different prepared edge geometries in the orthogonal finish turning of 4140 low alloy steel were collected from previously reported literature [81]. The turning operation was performed at a cutting speed of 300 m/min with a feed rate of 0.1mm/rev in dry condition. The cutting tool used had a rake angle and clearance angle of 3º and 8º, respectively. The simulation was conducted with similar cutting conditions.

## 4.1 Experimental Results

### 4.1.1 Cutting edges prepared by AJM

The cutting-edge samples were prepared through a wet abrasive jet machining (AJM) technique in the experimental study [81]. One unprepared and 5 different prepared cutting edges were measured, as shown in Table 6. The cutting tools are denoted as $E_i$, where "i" identifies the edge number. $E_0$ is the unprepared or sharp edge of the as-received insert. $E_1$-$E_5$ represent the symmetrical cutting edges with variations in radius.

Table 6: Edge geometry parameters of unprepared and prepared edges [85]

| **Cutting edge** | **Measured parameters for K-factor method** | | | | **Edge radius** |
|---|---|---|---|---|---|
| | $K$ | $\bar{S}$(μm) | $S_\alpha$ ($\mu m$) | $S_\gamma$ ($\mu m$) | $r_\beta$($\mu m$) |
| $E_0$ | 1.20 ± 0.110 | 4.69 ± 0.23 | 4.25 ± 0.27 | 5.12 ± 0.37 | 3.61 ± 0.16 |
| $E_1$ | 1.02 ± 0.010 | 14.70 ± 0.12 | 14.56 ± 0.17 | 14.83 ± 0.09 | 11.82 ± .09 |
| $E_2$ | 0.99 ± 0.016 | 21.26 ± 0.06 | 21.33 ± 0.19 | 21.20 ± 0.18 | 17.09 ± 0.16 |
| $E_3$ | 1.08 ± 0.012 | 27.26 ± 0.26 | 26.14 ± 0.15 | 28.38 ± 0.40 | 21.89 ± 0.29 |
| $E_4$ | 1.05 ± 0.003 | 47.85 ± 0.38 | 46.61 ± 0.38 | 49.08 ± 0.39 | 38.58 ± 0.37 |
| $E_5$ | 1.01 ± 0.003 | 68.56 ± 0.32 | 68.25 ± 0.27 | 68.87 ± 0.39 | 55.37 ± 0.25 |

The results of the tool life study show that for most of the prepared inserts (except $E_5$), the overall tool life remained nearly the same; this suggests that the tool edges break after the same cutting length, as seen in Fig. 24. No significant improvement of the total cutting length was observed. However, the width of flank wear of most prepared inserts were much lower than the unprepared inserts, showing a gradual increase in contrast to the unprepared edge. This suggests a slower tool edge abrasion rate after edge preparation.

The cutting edges $E_2$ and $E_3$ showed the optimal combination of tool life and wear of all the studied cases. Tool performance began to deteriorate once the average edge radius exceeded $r_\beta$ = 21.2 μm. Since the $E_2$ edge showed more gradual flank wear and almost identical tool life to the $E_3$ edge, the $E_1$ edge was the first to fail of the three. Thus, it can be concluded for symmetric edges, the preferable range of edge radius( $r_\beta$ ) is between 17 - 22 μm.

Table 7: Flank wear and cutting length of failure [85]

| Cutting edge | Cutting length (mm) | Flank wear (μm) | Remarks on failure type |
|---|---|---|---|
| **$E_0$** | 49149.43 | 285 | Abrasion wear on flank face |
| **$E_1$** | 46782.24 | 125 | Gross chipping |
| **$E_2$** | 52023.99 | 135 | Gross chipping |
| **$E_3$** | 54033.04 | 146 | Gross chipping |
| **$E_4$** | 50861.60 | 180 | Gross chipping |
| **$E_5$** | 39741.93 | 266 | Gross chipping |

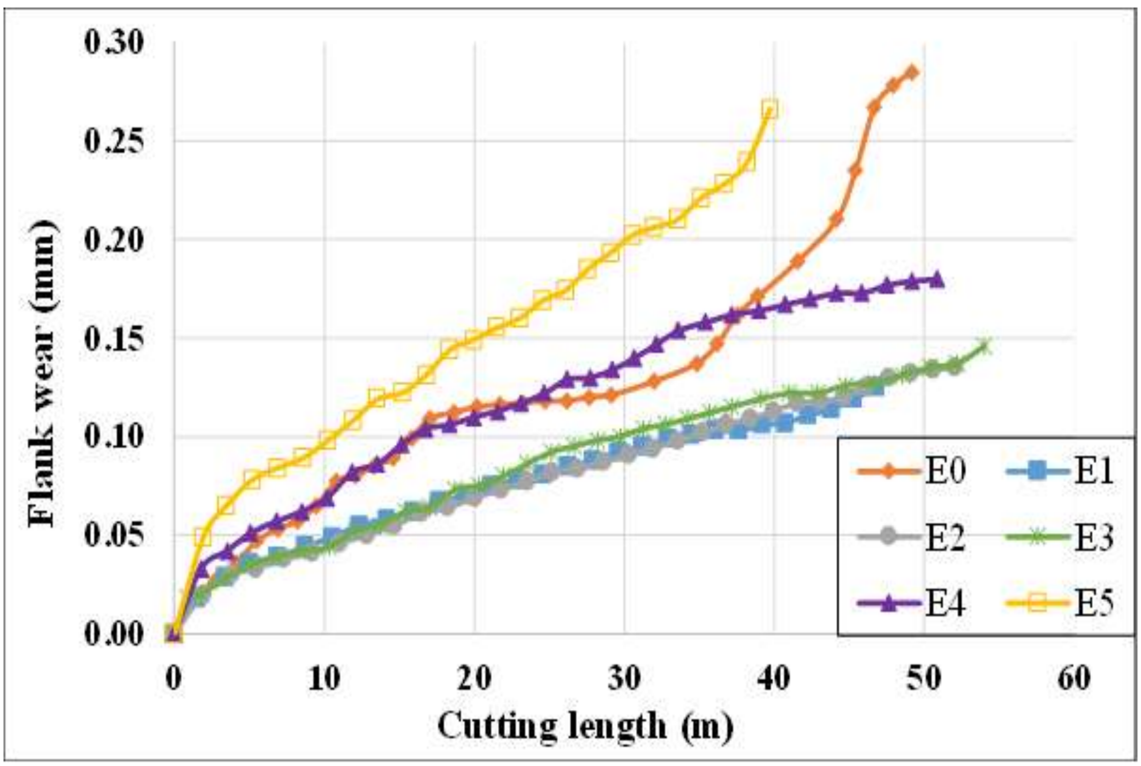


Figure 24: Measured Tool wear with different cutting tool(reprinted with permission [85])

### 4.1.2 Comparison of edge preparation methods

To compare the prepared cutting edges, the target edge geometry was made symmetric (K=1) with rounding of $\bar{S}$ = 20μm. The measured edge geometries of unprepared and prepared inserts are reported in Table 7. The produced rounded edges and radii of the three methods are very close (21.89 μm, 19.33 μm and 20.82 μm). However, both segments in the flank face ($S_\alpha$) and the rake face ($S_\gamma$) are smaller than those of other prepared edges in drag finishing.

Fig. 25 shows the comparison of tool wear under different edge preparation techniques. The cutting edge that underwent drag finishing showed the lowest tool wear at 50m of cut. Overall, the prepared edges performed better than the unprepared cutting tool. In contrast to the unprepared tool, wear on the prepared tools uniformly increased prior to failure.

Table 8: Measured K-factor parameters and edge radius of cutting tool sample edges.

| Edge condition | | Measurement parameters | | | | |
|---|---|---|---|---|---|---|
| | | K | $S_\alpha$ (μm) | $S_\gamma$ (μm) | $\bar{S}$ (μm) | $r_\beta$ (μm) |
| **Unprepared edge** | **U** | 1.20±0.110 | 4.25 ± 0.27 | 5.12 ± 0.37 | 4.69 ± 0.23 | 3.61 ± 0.16 |
| **Abrasive jet machining** | **AJM** | 1.08 ± 0.012 | 26.14 ± 0.15 | 28.38 ± 0.40 | 27.26 ± 0.26 | 21.89 ± 0.29 |
| **Brushing** | **B** | 1.18 ± 0.040 | 26.04 ± 0.77 | 30.72 ± 0.80 | 28.38 ± 0.78 | 19.33 ± 0.44 |
| **Drag finishing** | **DF** | 1.12 ± 0.030 | 23.56 ± 0.52 | 26.48 ± 0.96 | 25.02 ± 0.68 | 20.82 ± 0.69 |

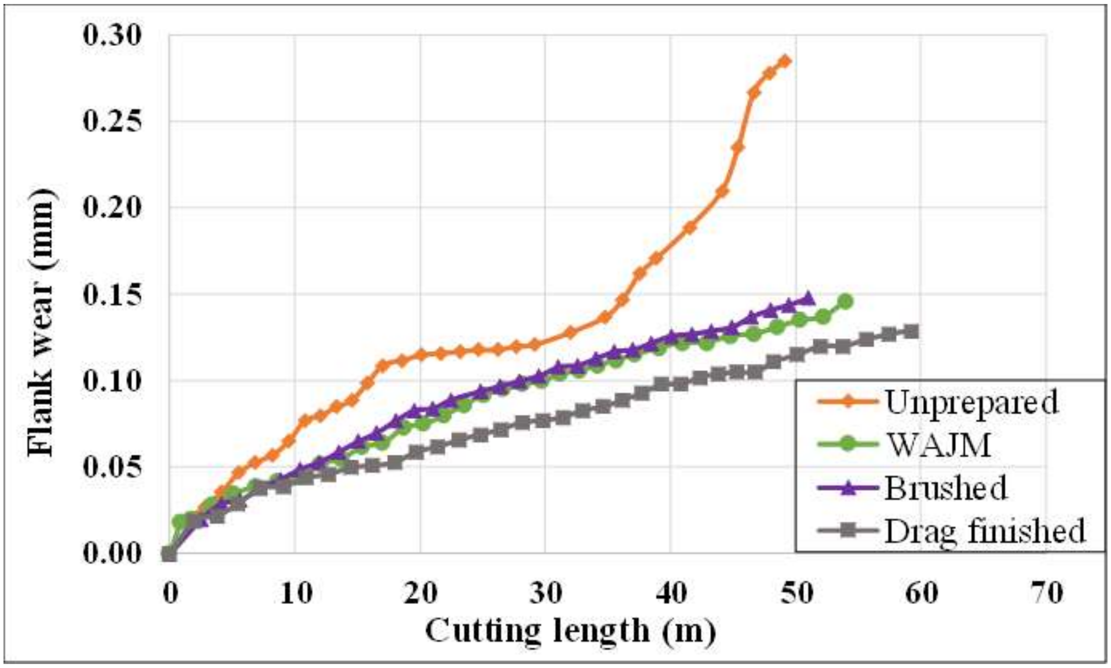


Figure 25: Effect of edge preparation technique on tool life (reprinted with permission [85])

## 4.2 Finite element model calibration

The FEA model can be calibrated by adjusting the friction coefficient [82]. Cutting and feed forces increased along with COF, thereby reducing the error between the experimental and predicted result, as shown in Fig. 26.

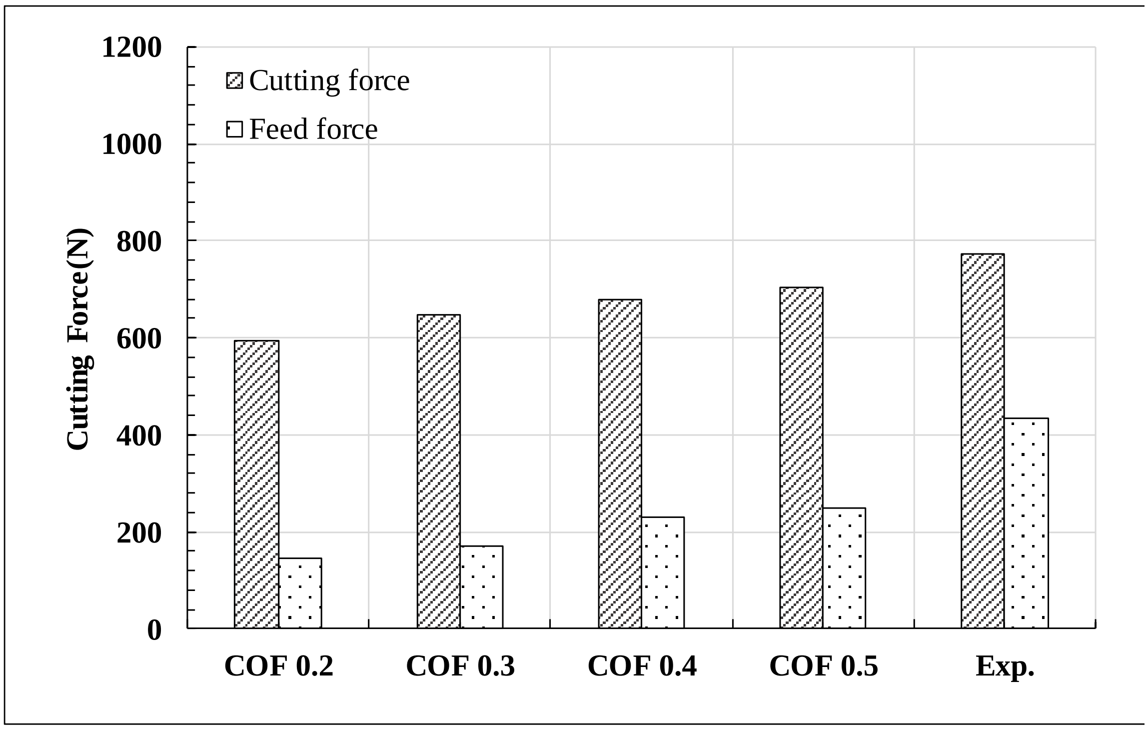


Figure 26: Calibration of cutting forces with respect of COF (a) Cutting force an (b) Feed force

However, when the COF (μ) changed from 0.4 to 0.5, the predicted cutting and feed forces had nearly equal values. COF μ=0.4 was used in the current study instead of μ=0.5, since a greater coefficient of friction generates a higher temperature, which delays the thermal convergence [83]. For a COF of μ=0.4, the error percentages of the cutting and feed forces with respect to the experimental mean values were 9.3% and 43.6%, respectively. The high error of feed force prediction was also reported in other studies [46], [45].

## 4.3 Effect of initial edge geometry

The thermo-mechanical properties of different prepared edges at the initial stage of tool wear are investigated in this section. Given that changes in thermo-mechanical behaviour are primarily dependent on flank edge geometry [6], this study is mostly focused on the thermo-mechanical behaviour changes at the flank face. The flank edge was determined by observing the negative contact shear stress value at the cutting edge. The negative direction of the contact shear stress value represents the movement of the workpiece underneath the flank face to form the machined surface [44].

### 4.3.1 Effect on cutting forces

Both experimental and numerical investigations confirmed that the cutting and feed forces increased along with edge radius, as shown in Fig. 27. The increments by which the feed force increased were greater than those of the cutting force. Similar force behaviour has been reported in previous studies [84], [3]. This behaviour is directly related to ploughing and the mechanism of chip formation. An incremental increase of edge radius produces an extended shear deformation zone. This leads to ploughing and severe deformation in the workpiece material near the tool tip [6], causing the cutting and feed forces to increase.

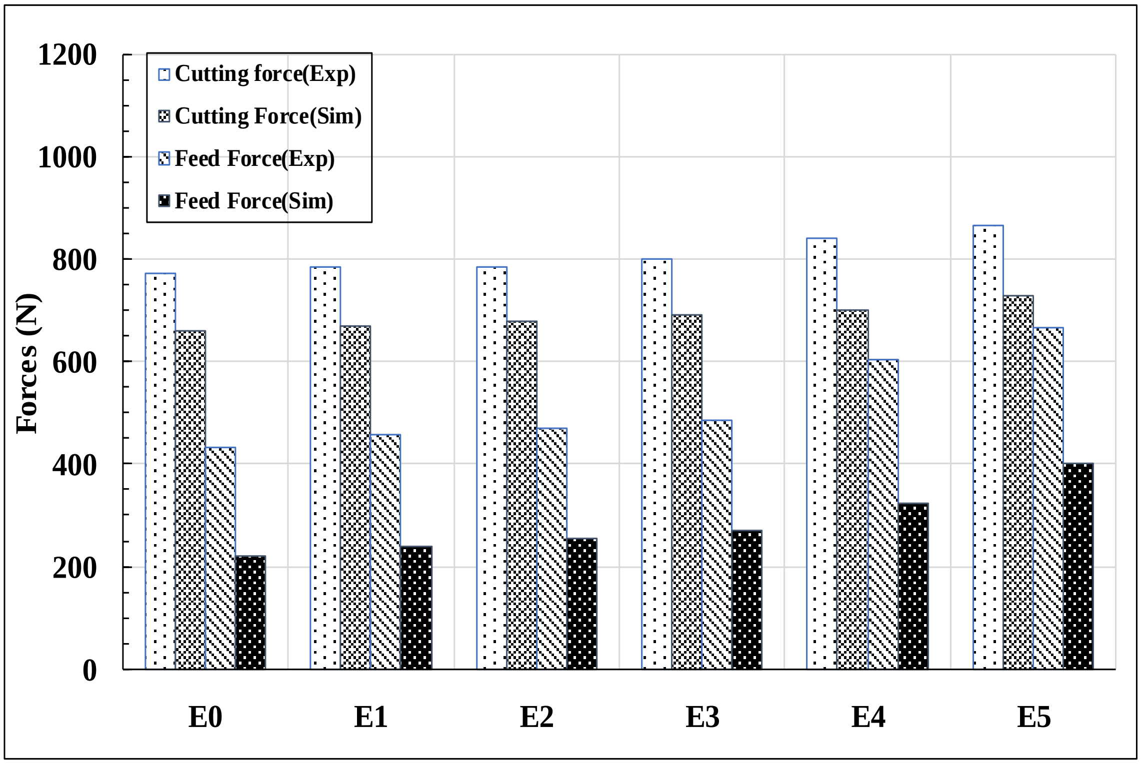


Figure 27: Effect of cutting-edge radius on Cutting force and Feed force

### 4.3.2 Effect on temperature and stress

Fig. 28 shows that the average flank temperature increased along with edge radius. The temperature of the unprepared tool was 660ºC, linearly increasing to 830ºC in $E_5$. This can be attributed to the extended friction area at the flank edge that induces higher temperatures [2]. However, a larger edge radius will also facilitate heat dissipation. Therefore, the edge radius has to be selected to provide optimum thermal load and heat dissipation. As the edge radius increases, the average temperature on the rake face remained almost constant, showing minimal growth. A similar pattern of increase in the overall cutting zone temperature caused by a larger edge radius was reported by Ng et al. [85].

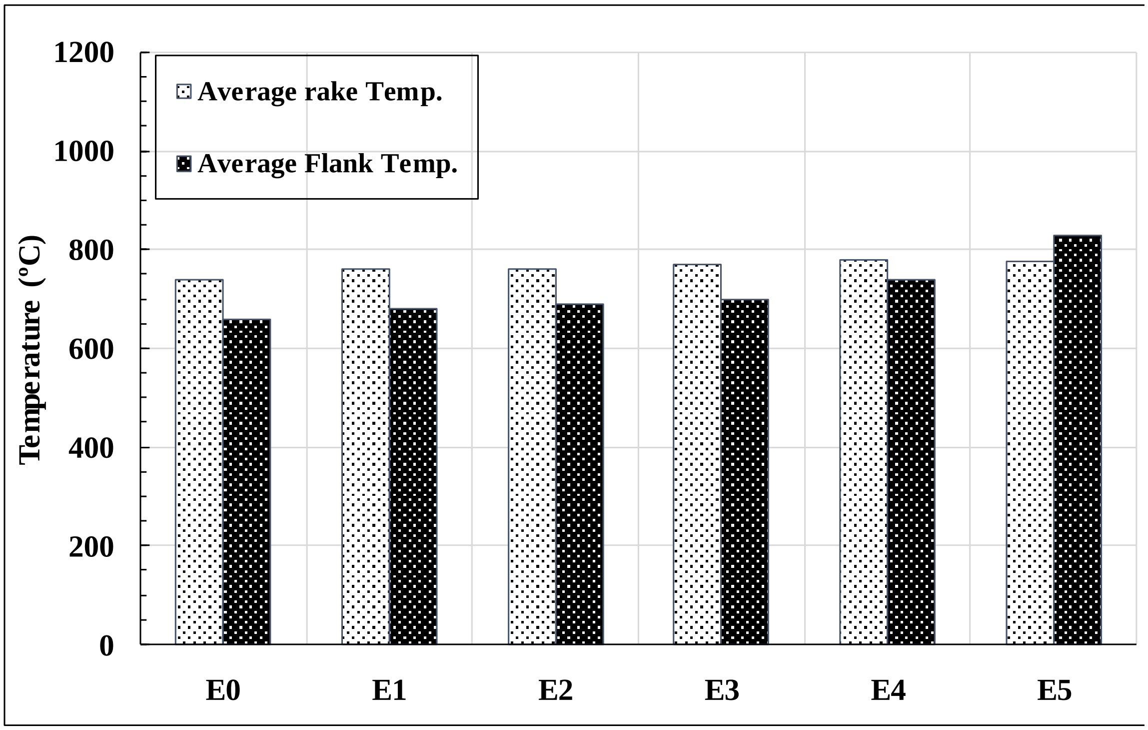


Figure 28: Changes in temperature at different edge radii

A shift in maximum temperature from the rake face to the flank face with increasing edge radius could also be seen in Fig. 29. An expanded tertiary deformation zone was formed with the growth of edge radius, generating a greater amount of heat. As a result, the maximum temperature shifted to the flank face. Examples of such behaviour were also reported in previous studies [6], [84].

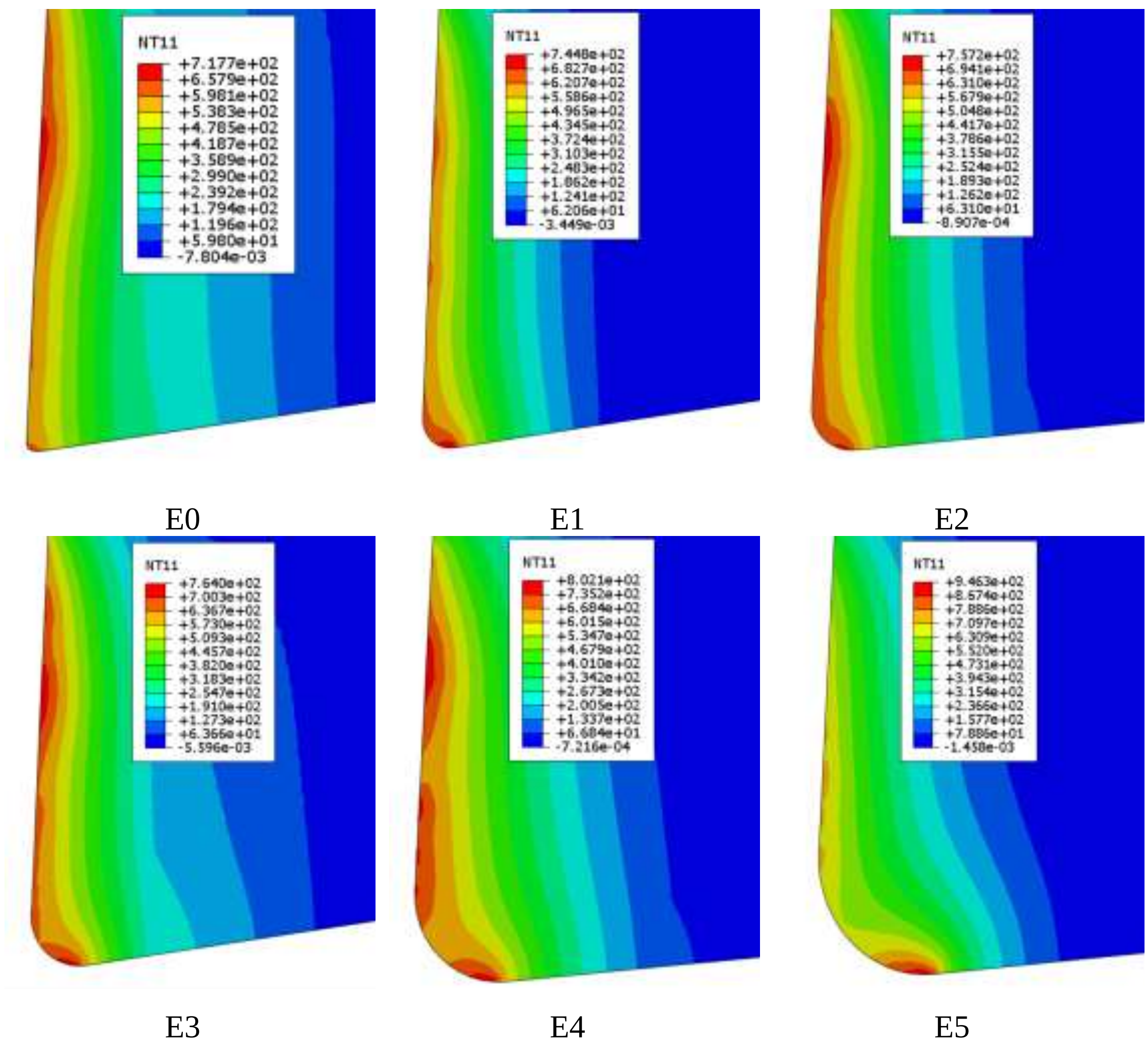


Figure 29: Spatial variation in cutting tool temperature (ºC) at different edge radii

Fig. 30 shows the stress behaviour on the flank face at different edge radii. The maximum VM stress in the unprepared tool was approximately 3000 MPa. The maximum VM stress was up to 23.3% lower in $E_1$-$E_3$ than in the unprepared cutting tool. However, maximum VM increased along with the edge radius in the prepared edges. The higher stress concentration on the unprepared edge occurs due to the very small contact area between the cutting edge and the workpiece at the tool tip. Uniform stress distribution with less stress concentration on the prepared tool edge provides the cutting tool with more stability. The average contact stress, however, remains almost the same at different edge radii.

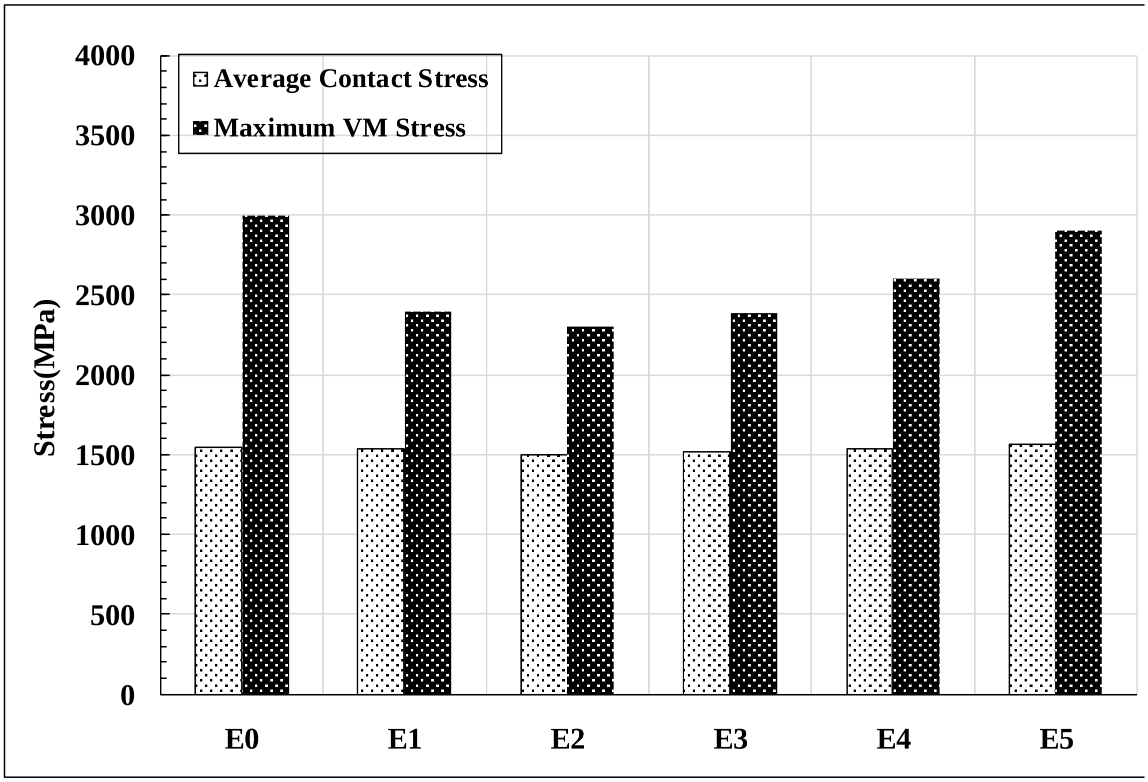


Figure 30: Change in contact stress and maximum VM stress at different edge radii

Fig. 31 shows the spatial distribution of VM stress at the edges. Maximum VM stress shifted to the flank face in E4 and E5. Similar phenomena of shifting maximum VM stress with increasing edge radius were also reported by Al-jekri et al [59].

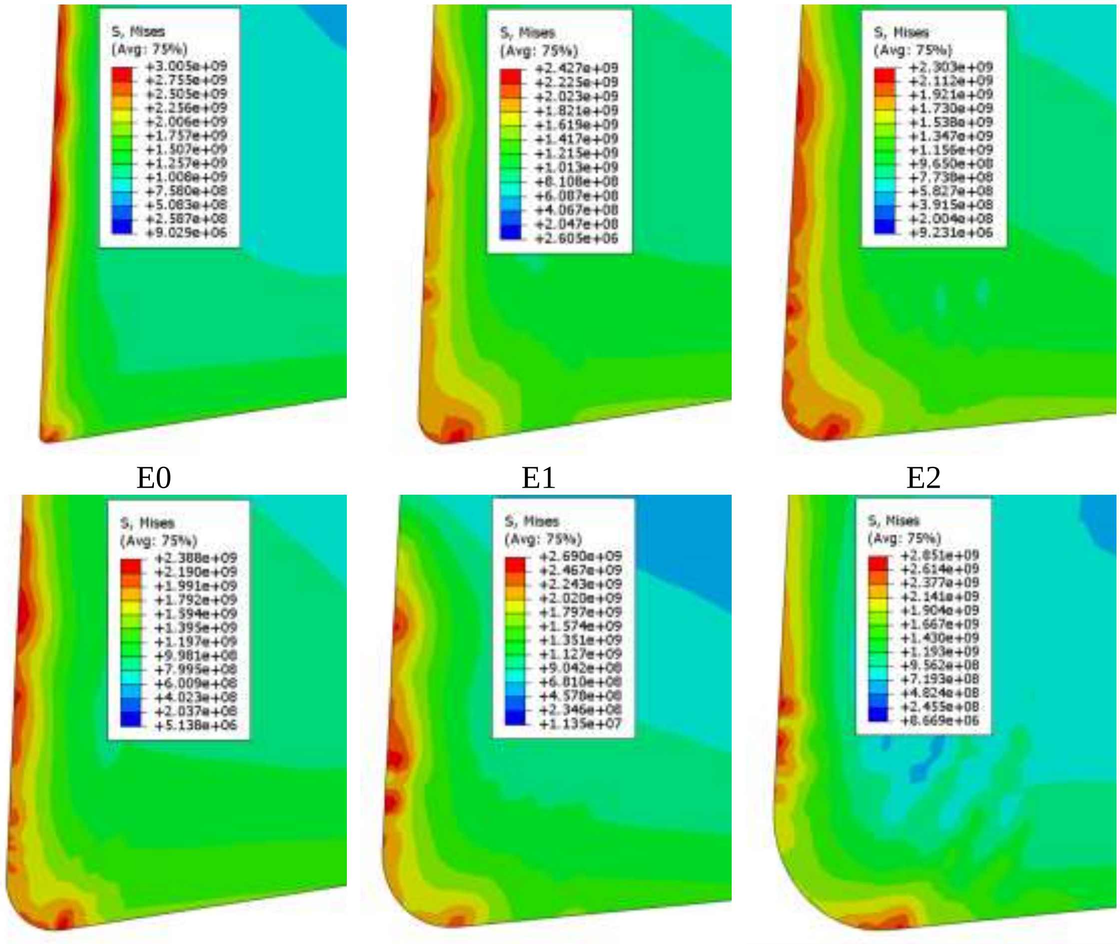


Figure 31: Spatial studies of VM stress (Pa) at different cutting-edge radii

### 4.3.3 Effect on Material Velocity

A stagnation zone forms when the workpiece material velocity around the tool tip approaches zero. The size of the stagnation zone is dependent on the ratio between the edge radius and the uncut chip thickness [3]. The uncut chip thickness was constant throughout all of the studies. Fig. 32 shows the variation in sliding velocities at the differently prepared edge radii. The stagnation zone was quantitatively calculated from the workpiece material sliding velocity adjacent to the flank face. It can be seen in Fig. 32 that the sliding velocity reduced by up to 71.29% in the prepared tool ($E_5$) compared to the unprepared tool, indicating the presence of a larger zone of stagnation near the tool tip, see Fig 33. The formation of a stagnation zone can be related to the probability of BUE formation [86].

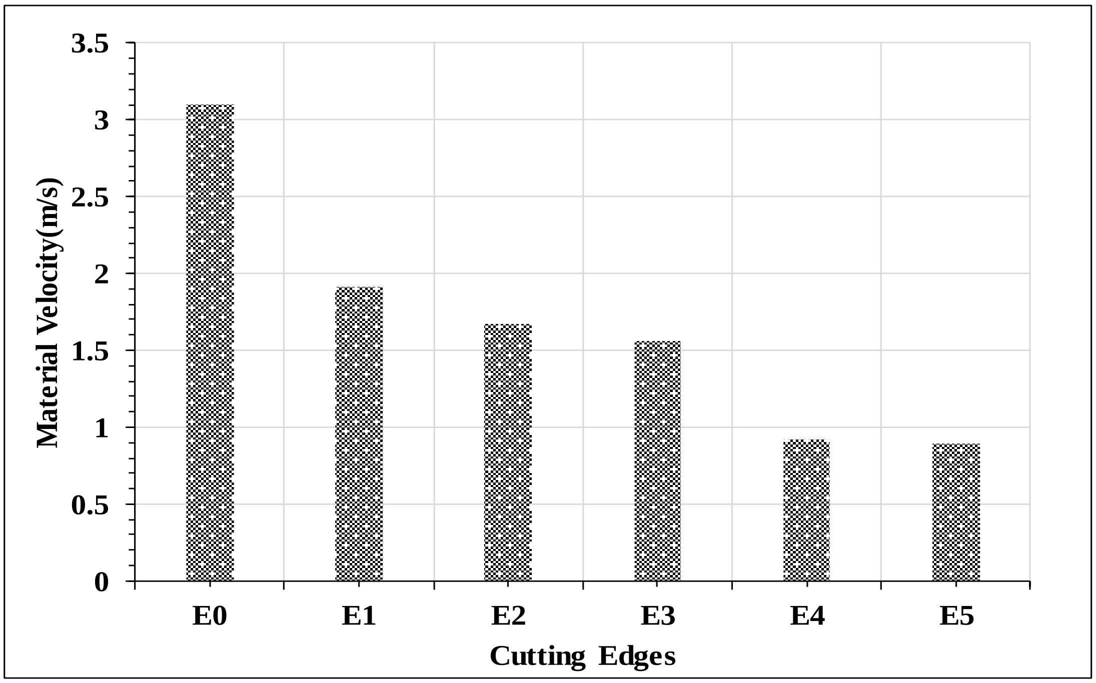


Figure 32: Material velocity near the tool tip at different prepared edges

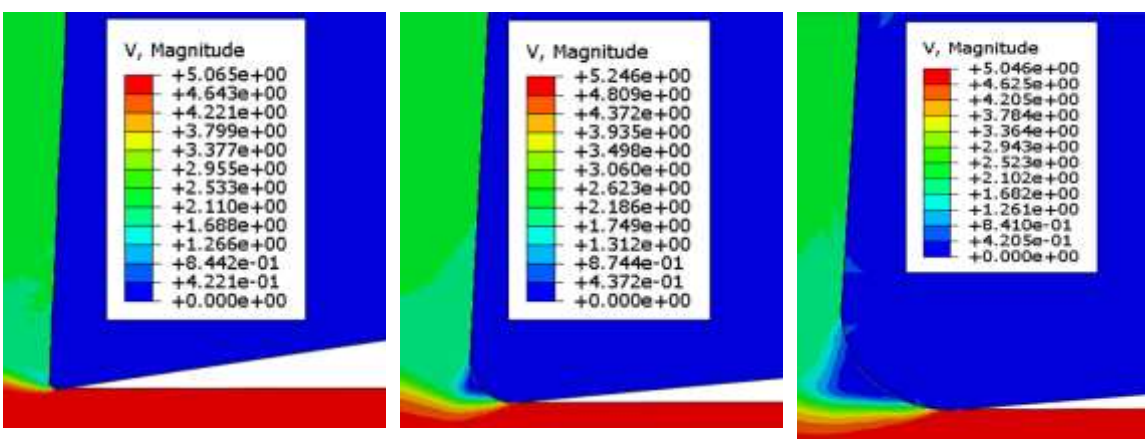


E0 E2 E5

Figure 33: Spatial studies of material velocity (m/s) at different cutting-edge radii

## 4.4 Effect of worn tool geometry

In this section, change in thermo-mechanical behaviour in cutting edge due to tool wear progression was investigated. The simulation was performed with a worn cutting tool. The worn cutting tool was obtained using a novel tool updating technique. The study was performed using unprepared cutting tool wear progression data.

### 4.4.1 Tool geometry updating

The prediction of worn tool geometry has always been challenging. In previous studies, tool geometry was predicted either based on a nodal displacement or by assuming a displacement vector parallel to the machined surface at the tool tip [19], [20]. Both approaches have computational limitations, such as mesh convergence and less realistic worn tool geometry. Hosseinkhani et al. directly exported worn tool geometry from an experimental study where the worn cutting edge resembled a chamfered edge [11].

In the current work, a simpler but novel approach was used to update the cutting edge by introducing a displacement vector at the flank edge as described in Fig 34(a). Considering the flank edge as an arc, the displacement vector was drawn tangent to it at the midpoint. Once the displacement vector was defined, it was displaced in the normal direction based on the experimental flank wear, Figure 34(b). The displacement vector made an inclination angle (β) with respect to the machined surface. These inclination angles vary in the different prepared edges.

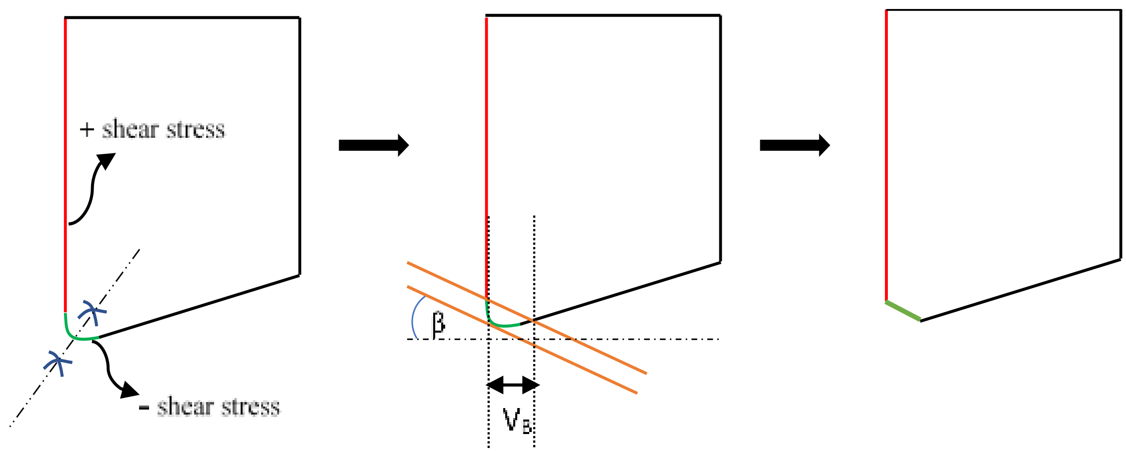


(a) (b) (c)

Figure 34: Methodology of updating the worn tool geometry. a) finding flank face b) drawing displacement vector c) Worn tool

### 4.4.2 Change in deformation zone

The effect of tool wear on workpiece flow stress is described in Fig. 35. High plastic stress was found in the new tool at the primary shear deformation zone (PSDZ), along the tool-chip interface (SSDZ) and a small deformation area beneath the flank face (TSDZ). Referring to Figure 35 (a) to (c), the tertiary deformation region expanded along the workpiece material and the flank face as the cutting length increased. A growing volume of workpiece material is pushed beneath the flank face as the tool wears out. As a result, more energy is required to move and deform the workpiece material in order to create the machined surface. This behaviour also causes the cutting forces to rise. However, it was found that neither PSDZ nor SSDZ were affected by tool wear.

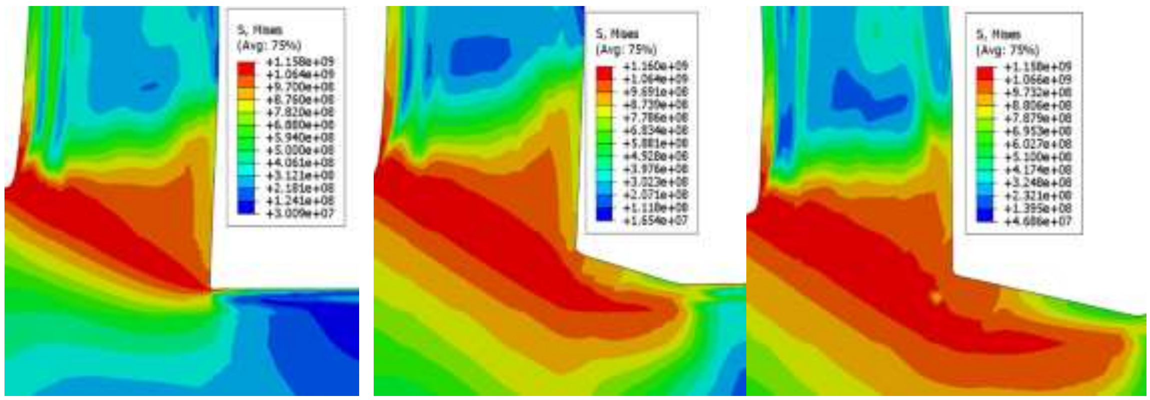

a) New b) 35m c) 50m

Figure 35:Plastic flow stress (Pa) distribution in workpiece at different cutting length

### 4.4.3 Stress behaviour

Fig. 36 displays the average contact stress at different stages of the cutting length in the flank face. The general trend suggests that the contact stress increased as the cutting tool wears out. However, the average contact stress increased by up to 15% in the worn tool (50m) compared to the new tool. The higher magnitude of average contact stress is caused by the formation of TSDZ by expanded contact area.

The maximum effective stress increased along with tool wear at different cutting lengths, as shown in Fig. 36. The maximum VM stress on the flank face of the new tool was found to be about 3000MPa, which further increased to 3400 MPa and 3900 MPa at cutting lengths of 30m and 50m.

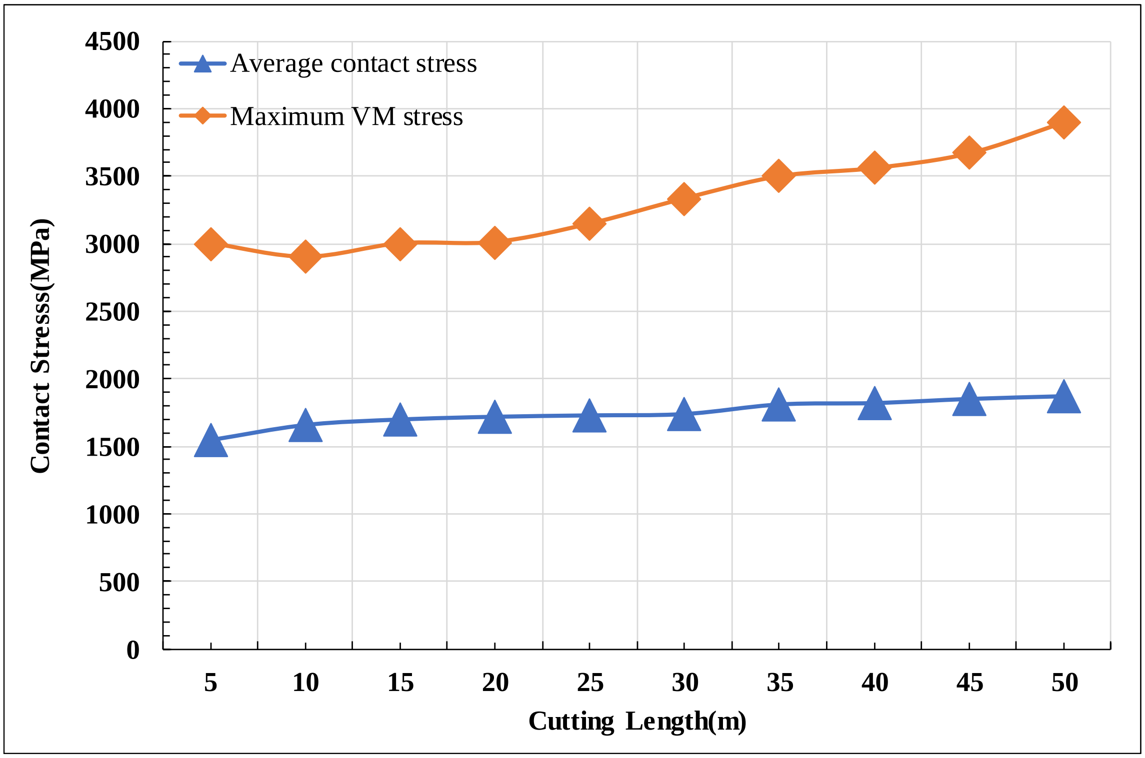


Figure 36: Temporal variation in stress on the flank face at different cutting lengths

Additionally, the initial stage of wear maximum stress was distributed on both the rake face and the tool tip. However, the location of maximum stress tended to change from the rake face to the flank face as tool wear progressed, as can be seen in Fig. 37. This can be explained as follows: as the tool wears out, the flank edge increases and the higher normal force intensifies its action on the extended flank face [49].

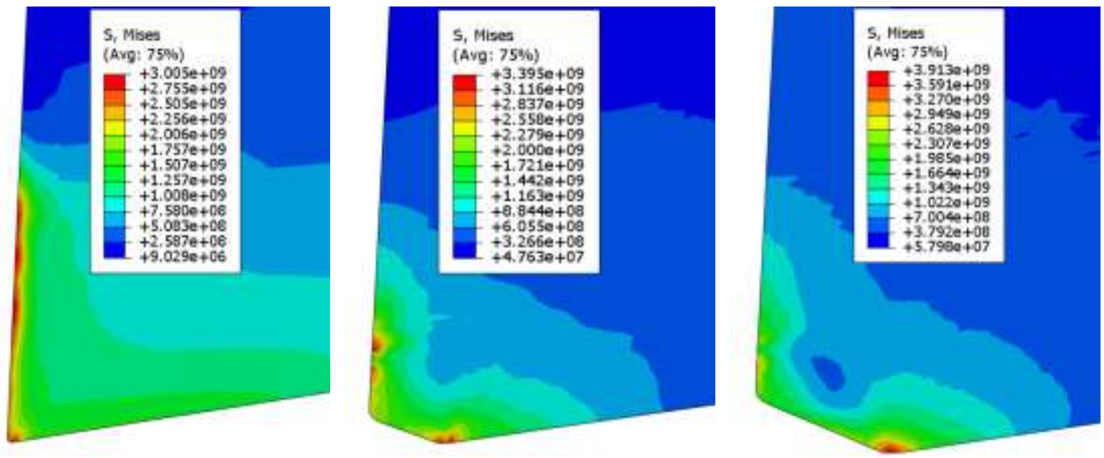


VM Stress (Pa) @new tool VM Stress (Pa) @30m VM Stress (Pa) @50m

Figure 37: Spatial variation in VM stress on the cutting edge

### 4.4.4 Temperature behaviour

Fig. 38 presents the variation in the average tool temperature on the flank and the rake face. The average cutting temperature increased along with tool wear. Once the tool wear stabilized, so did the cutting temperature. This phenomenon can be ascribed to the expanding flank edge, which causes rubbing against the machined surface. The simulated average temperature at the flank face was 660ºC, 780ºC and 880ºC at lengths of 0, 30, and 50 m, respectively. In addition, it was observed that maximum temperature on the cutting tool increased substantially as the tool wore out. However, the average temperature trend on the rake face was nearly constant, with only minor growth. Similar cutting temperature patterns in the flank and rake faces were also reported in different studies [59], [14].

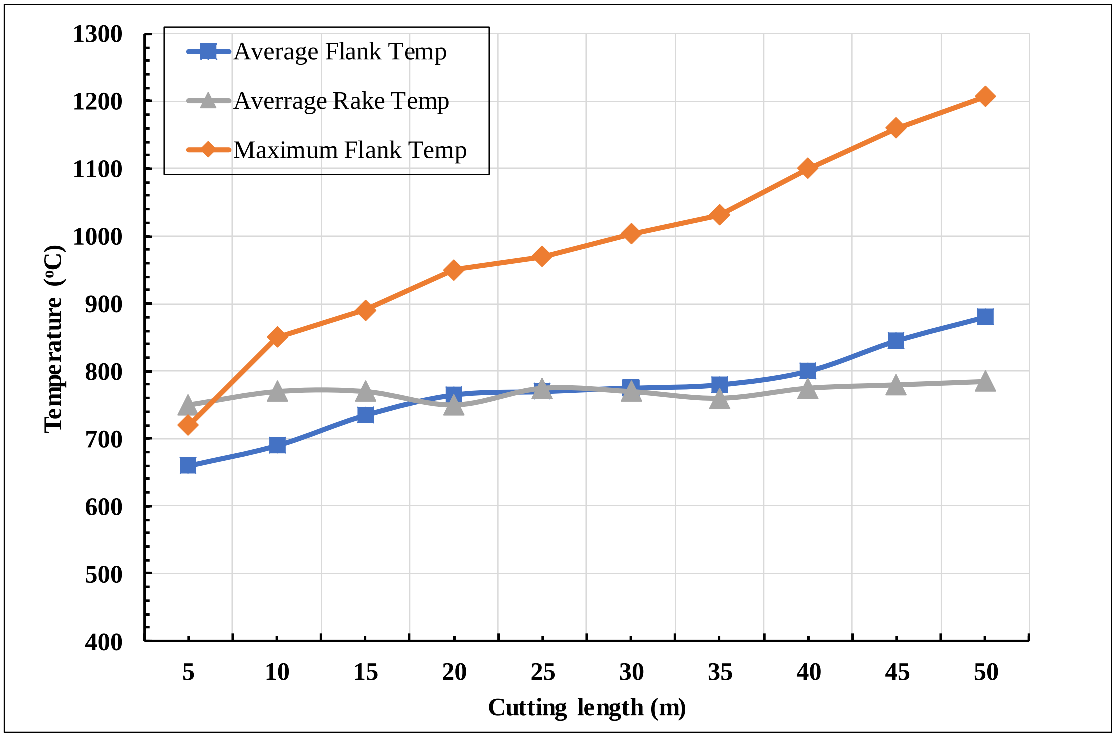


Figure 38: Relation between cutting temperature and cutting length at the rake and flank faces of the cutting tool

Fig. 39 represents the thermal behaviour of a new cutting tool where the maximum tool temperature was found at the rake face at a distance from the tool tip. Furthermore, the maximum heat flux was observed at the primary shear deformation zone where a high strain rate and plastic deformation are present, see Fig. 39 (a). Since the new cutting tool has a very small flank area, the deformation is limited to the primary and secondary shear deformation zones. Therefore, the highest tool temperature occurred at the rake face [87]. However, as shown in Fig. 39 (c) & (d), the location of maximum tool temperature shifted from the rake to the flank face as the tool begins to wear out. Additionally, the heat flux was distributed along the flank face of the worn tool, Fig.39 (b). A similar pattern of changing temperature due to tool wear has been reported in literature [44].

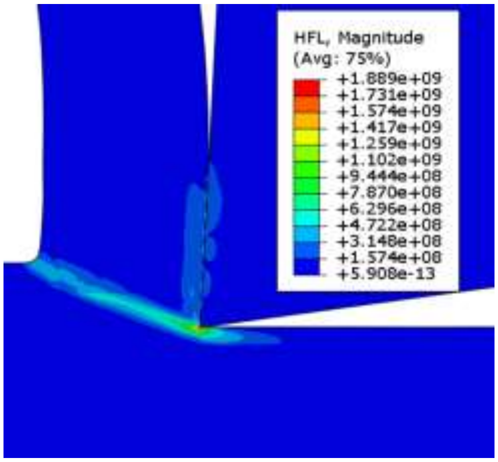


(a) Heat flux(W/m$^2$) – new edge

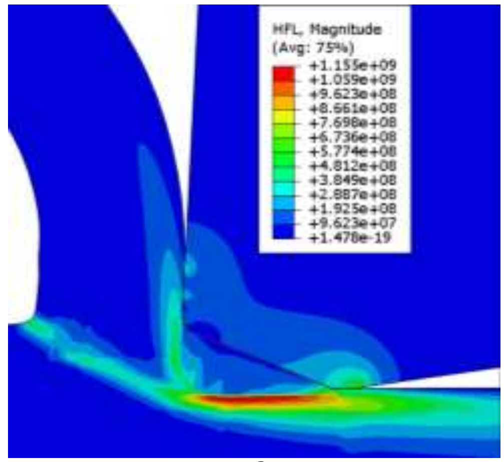


(b) Heat flux (W/m$^2$ )– worn edge at 50m

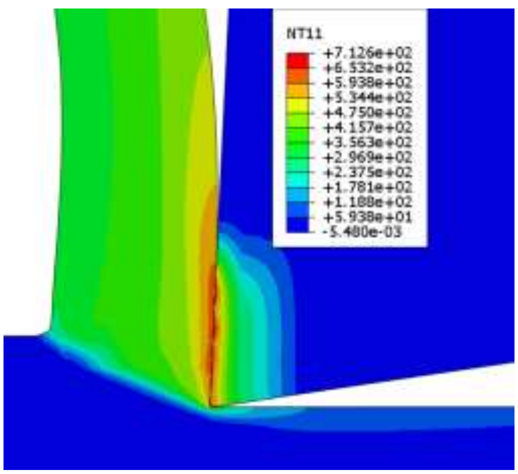


(c) Temperature (ºC)– new edge

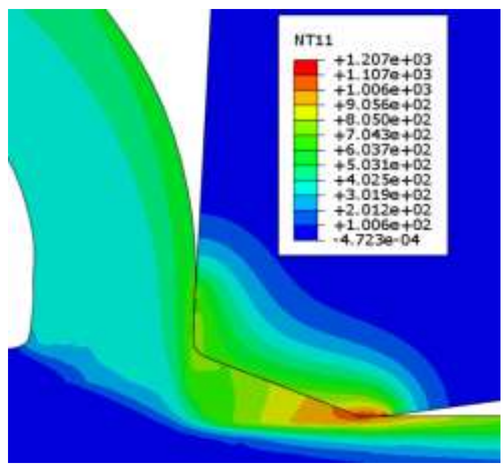


(d) Temperature (ºC)-worn edge at 50m

Figure 39: Heat flux distribution of the (a) new edge and (b) worn edge after a 50 m cutting length and temperature distribution of the (c) new edge and the (d) worn edge after a 50 m cutting length.

### 4.4.5 Cutting forces

Both the cutting and feed forces increased as the tool wore out. The feed force was more sensitive to wear than the cutting force, as seen in Fig. 40. The cutting force of the new tool was approximately 690N, increasing to 850N, while the feed force of the new tool was 220N, rapidly increasing up to 1280N at 50m of cutting length. The area of contact on the flank edge expands at longer cutting lengths. When the material moves over the flank face, the main force component acts perpendicular to the flank face in the same direction as the feed force. Consequently, the feed force increment is greater than that of the cutting force [44]. The increase of forces due to tool wear was reported earlier [88], [89].

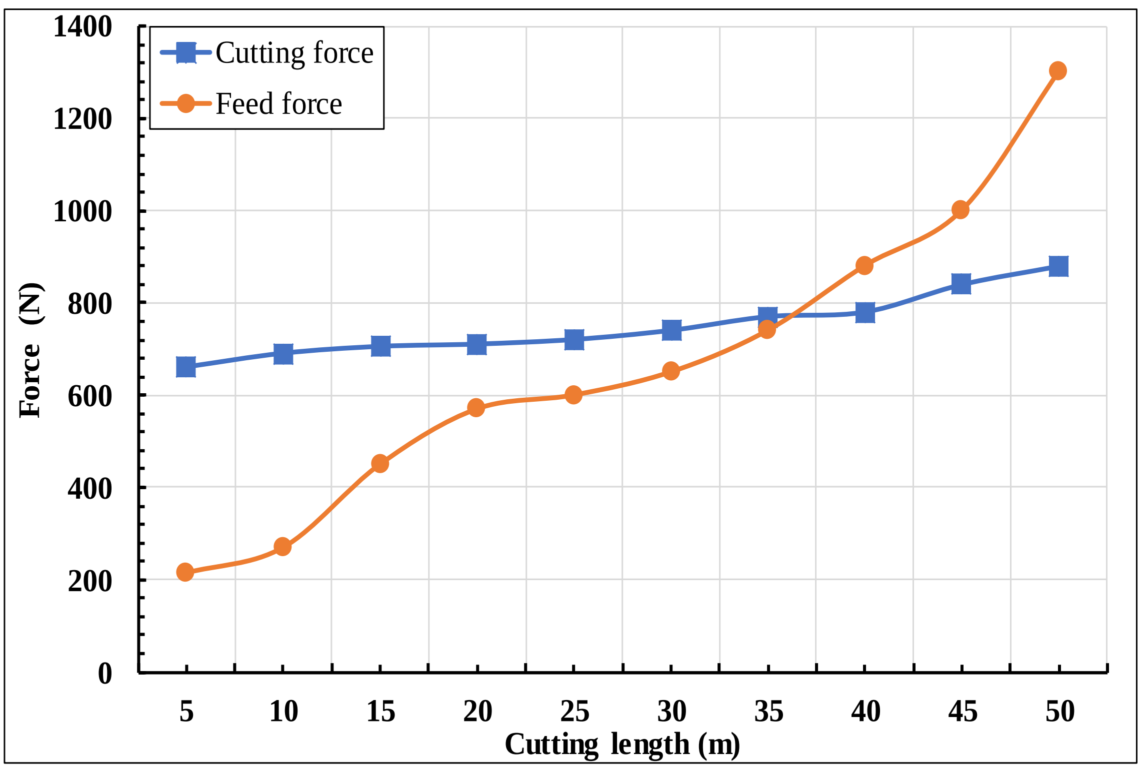


Figure 40 : Cutting force and feed force behaviuor at different cutting lengths

Although the current simulation agreed with the experimental trend, the incremental increase of feed force was greater than expected. The primary cause of this unrealistic feed force increase is the idealized flank wear geometry of the tool wear updating technique used by the FE model. Similar discrepancies in the feed force due to idealized flank geometry were previously reported [21], [44].

### 4.4.6 Tool-chip and tool-machined surface contact

The velocity profile in the cutting zone has been successfully simulated in the current study. Fig. 41 shows the trends of sliding velocity and tool-chip contact length as the tool wears out. Flank sliding velocity sharply dropped at the beginning of cutting due to rapid initial wear followed by a near steady flank sliding velocity as the tool wear reached the steady-state region.

The chamfer area on the flank face increased with tool wear. This caused the stagnation zone to expand and, consequently, decreased the sliding velocity at the flank face, see Fig. 42. The expansion of the stagnation zone due to the blunt and chamfered shape of the cutting tool has been mentioned in previous studies [90], [91]. However, the sliding velocity on the rake face remained stable throughout the cut. The change in rake face geometry had an insignificant effect on material velocity near the tool tip [6]. The tool/chip contact length decreased slightly with cutting distance. This diminishing tool-chip contact behaviour was confirmed by the experimental study [92].

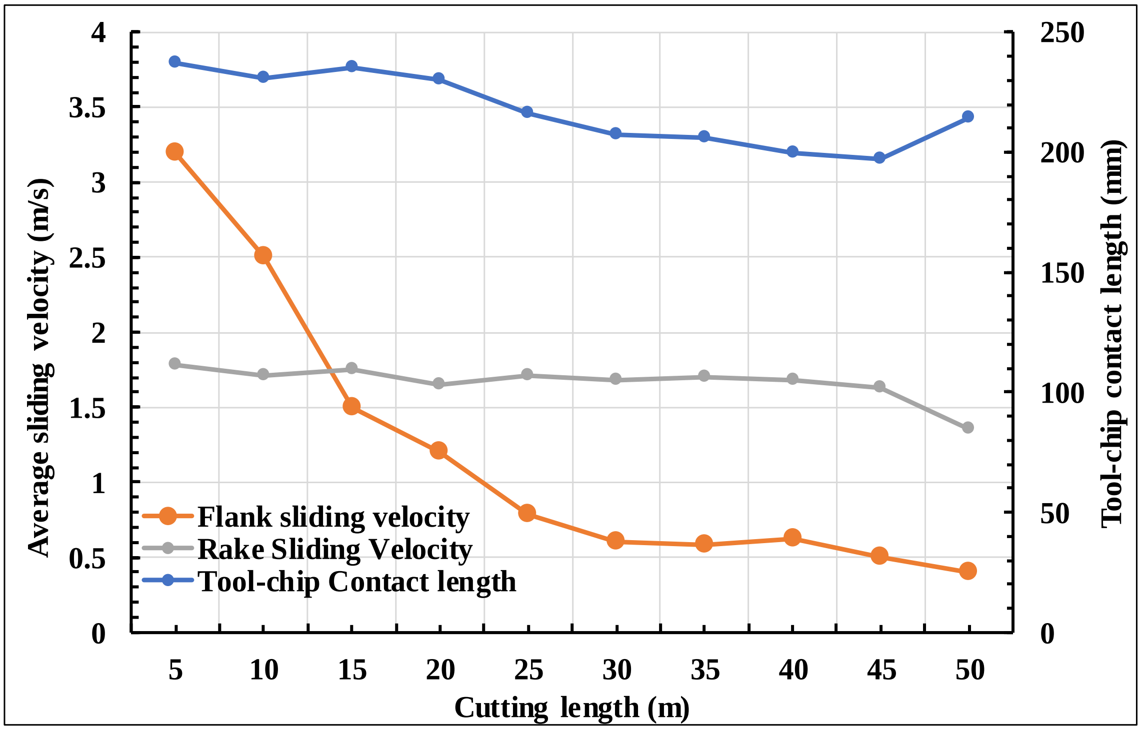


Figure 41: Temporal variation of average sliding velocity on the flank and rake faces

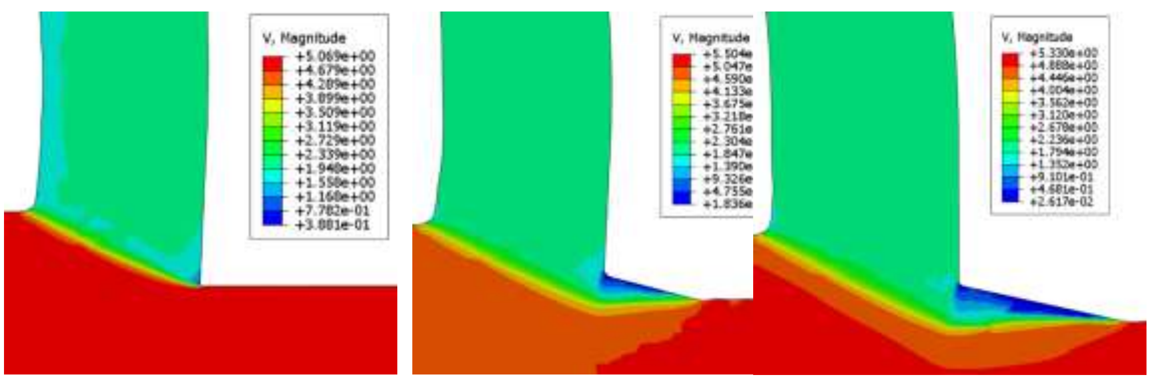


New Worn (35m) Worn(50m)

Figure 42: Spatial distribution of material velocity (Workpiece only)

### 4.4.7 Plastic deformation

The plastic deformation of the machined surface directly affects the surface quality of the workpiece. Fig. 43 shows plastic deformation along the depth of the machined surface in both the new and worn tools. As the cutting tool wore out, the deformation remained high on the machined surface, becoming less within its depth. The maximum PEEQ value on the machined top surface of the worn tool (35 m) was about 12, and in the new tool, approximately 3.6. The plastic deformation inside the machined surface was greater when a worn tool was used compared to a new one. Higher plastic deformation due to the extended flank area was also observed by Nasr. et al [42].

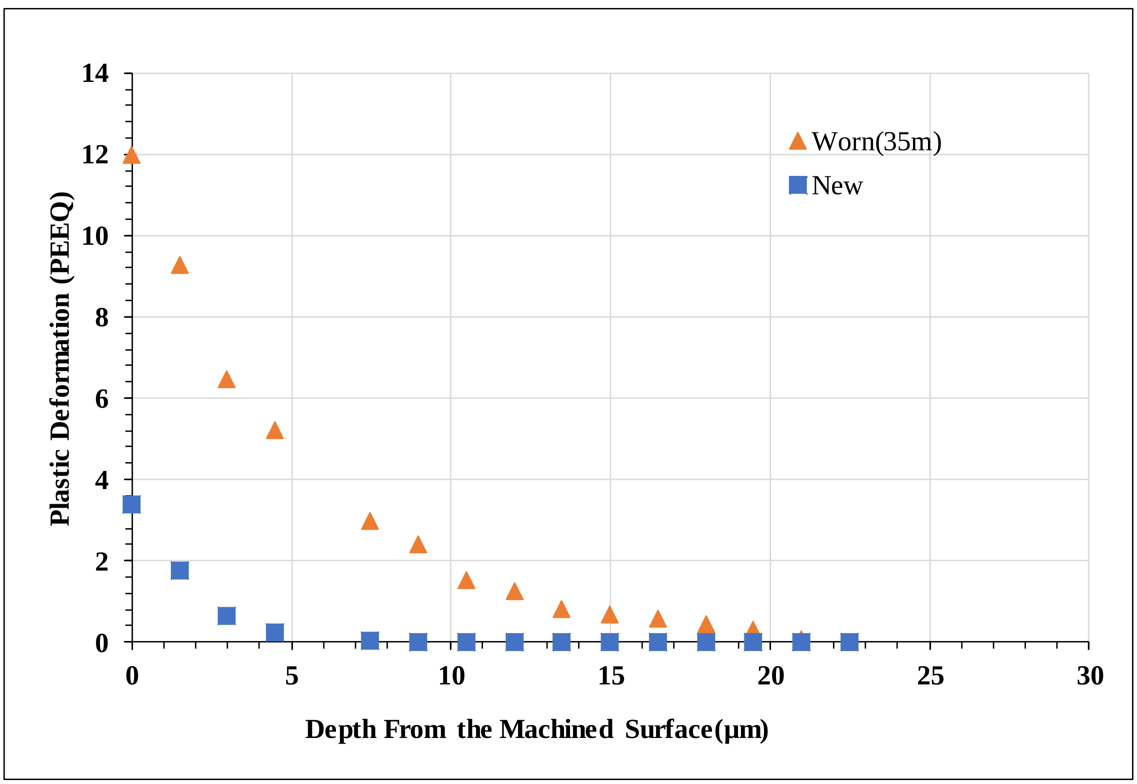


Figure 43: Comparison of plastic deformation in the worn and new tool.

## 4.5 Effect of edge preparation method

Different edge preparation methodologies influence cutting-edge properties. Orthogonal finish turning of AISI 4140 alloy steel reported by Wang [81] demonstrated the variation of tool wear due to different methods of edge preparation. The current model could simulate metal cutting at different lengths of cut. A finite element analysis was carried out to investigate the role of thermo-mechanical behaviour on the performance of the cutting edges prepared by different edge preparation technique.

### 4.5.1 Stress distribution

This section discusses the effect of edge micro-geometry produced by different preparation methods on the stress field. The new unprepared cutting tool has a comparatively smaller edge radius, causing more VM stress to accumulate near the tool tip. However, the maximum von Mises stress was reduced by nearly 20% in all the new prepared cutting tools. Maximum VM stress increased along with cutting length in all the cutting edges. Figure 44 shows that the worn unprepared tool had an effective stress of 3900 MPa after a 50 m cut. At the same cutting length, the maximum effective stress of the prepared cutting tools by AJM and Brushing was around 3300 MPa. The prepared tool by drag finish showed a reduced VM stress of 3160 MPa.

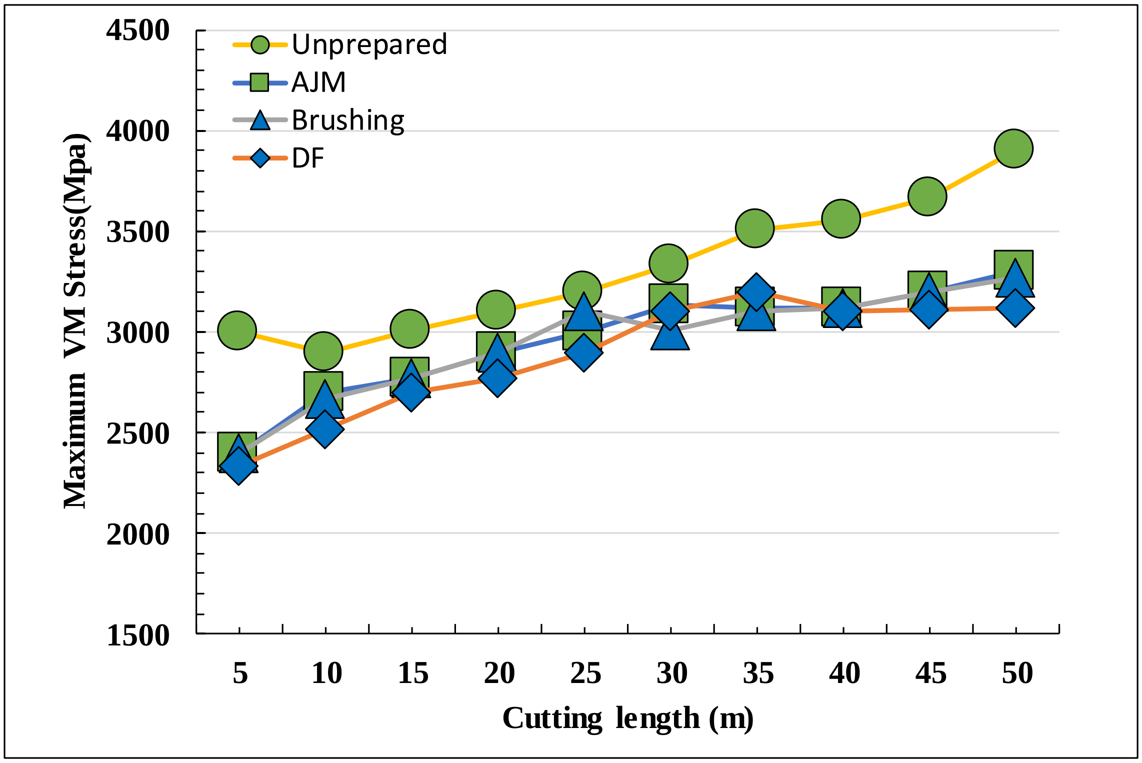


Figure 44: Temporal variation in VM stress on the flank face with cutting length.

Fig. 45 shows the spatial distribution of VM stress in cutting tool at 50 m of cut. The maximum VM stress of the unprepared edge was localized on the flank face, whereas in the prepared edges, the maximum VM stress was distributed on both the rake and flank faces.

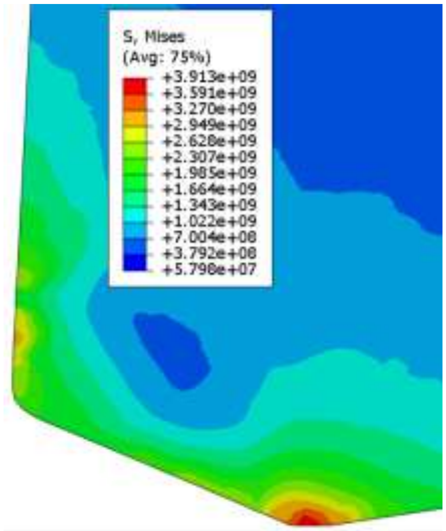


Unprepared VM Stress (Pa)@50m

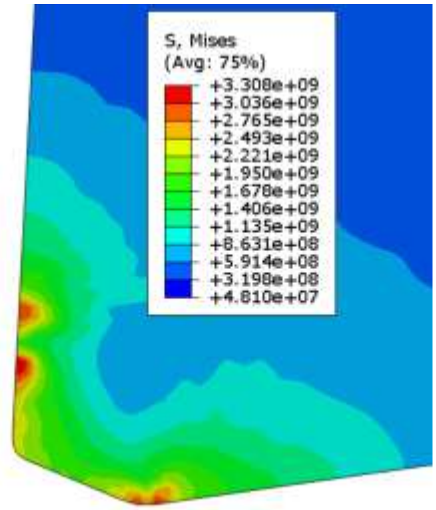


AJM VM Stress (Pa)@50m

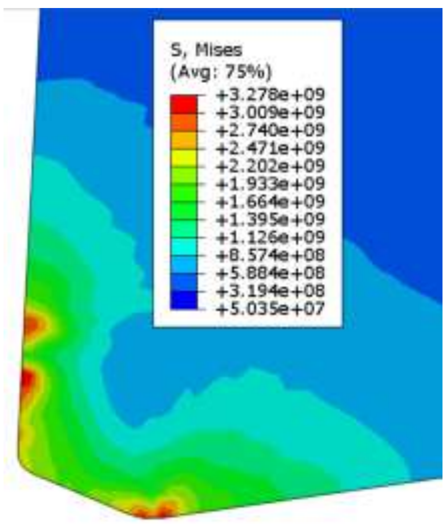


Brushing VM Stress (Pa)@50m

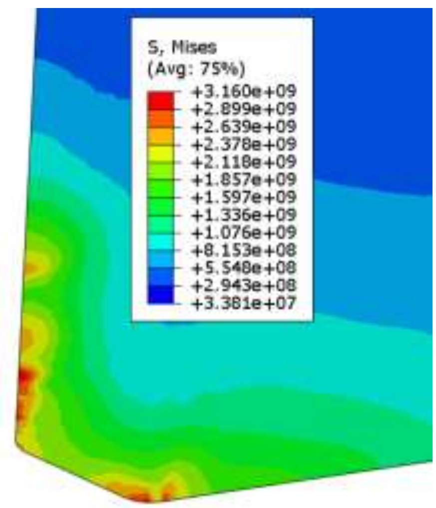


DF VM Stress (Pa)@50m

Figure 45: Spatial variation in VM stress on the cutting edge@50m.

### 4.5.2 Thermal behaviour

Fig. 46 shows that the maximum temperature on the flank face was the same in all of the edges during the initial wear stage. However, as the tool wear increased, the maximum temperature in all cutting edges did as well. The increase in the maximum temperature of an unprepared tool was greater than that of the prepared tools, by a magnitude of up to 70% at a cutting length of 50m. At the same cutting length, the temperature rise was around 38% for prepared tool by AJM and brushing and 32% in drag finishing.

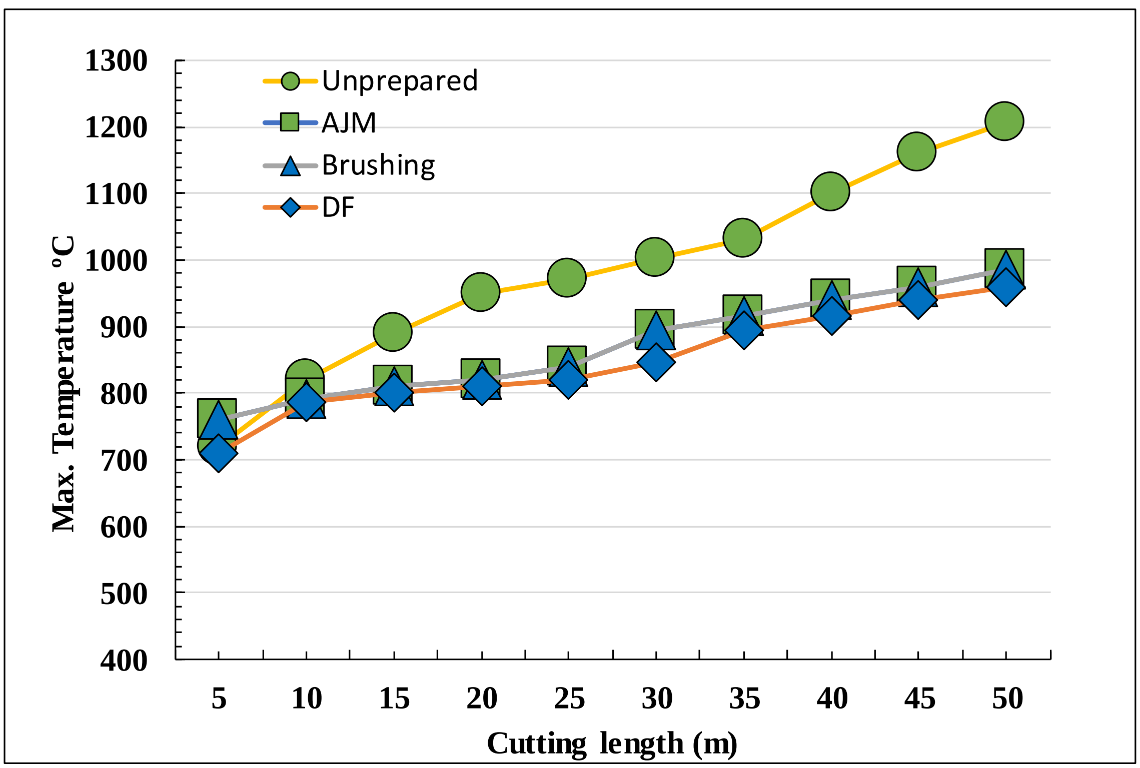


Figure 46: Temporal variation in maximum temperature on the flank face with cutting length

The spatial temperature distribution of the worn tool at a cutting length of 50m of all the tools has been shown in Fig. 47. The maximum temperature of the unprepared edge was localized on the flank face, whereas in the prepared edges, the maximum temperature was distributed on both the rake and flank faces.

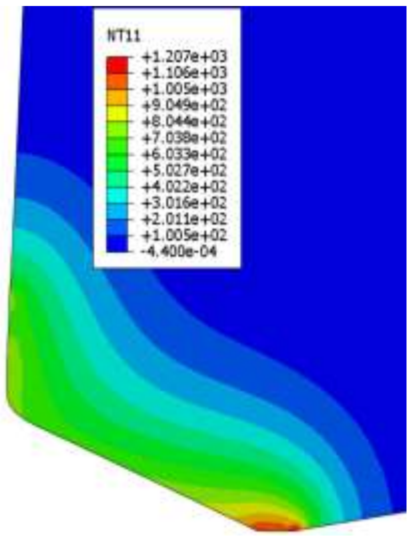


Unprepared Temperature(ºC) @50m

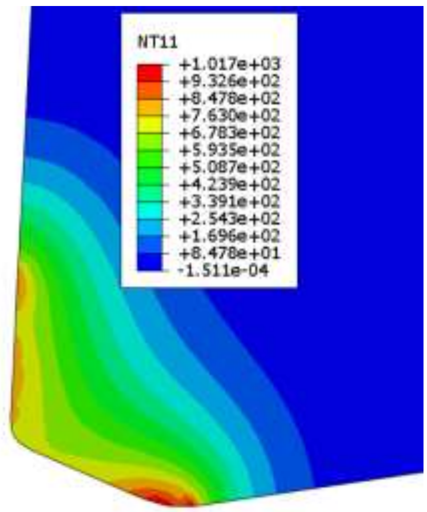


AJM Temperature(ºC) @50m

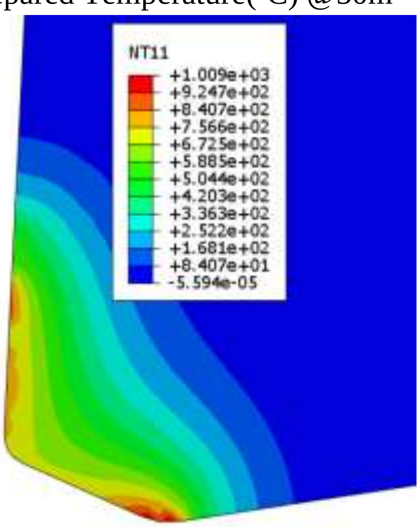


Brushing Temperature(ºC) @50m

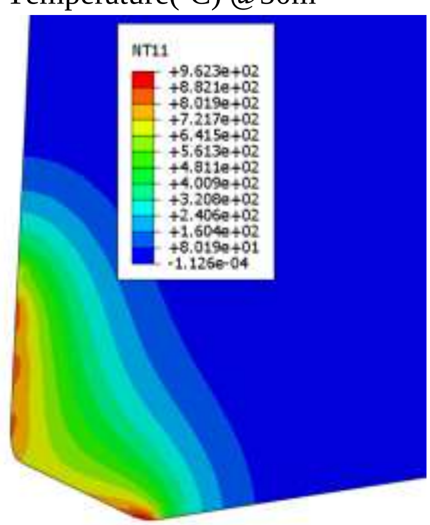


DF Temperature(ºC) @50m

Figure 47: Spatial variation in maximum temperature on the cutting edge @50m

## 4.6 Discussion

Thermo-mechanical behaviour at the tool-workpiece interface has a direct influence on the tool wear pattern and characteristics. An optimal edge radius can be selected on the basis of a numerical study of the differently prepared edges' thermo-mechanical properties.

The mechanical abrasion caused by hard abrasive particles and diffusion wear is a physio-chemical process heavily dependent upon temperature. In the current numerical study, the temperature increased along with edge radius. It can be seen in Fig.s 28 and 29, that the temperatures in edge ($E_1$-$E_3$) remained almost constant but increased in $E_4$ and $E_5$. However, average contact stress did not increase with increase in edge radius; stress distribution is uniform for all the prepared edges. The experimental study found that the flank wear of $E_1$-$E_3$ edge radii remained constant until the end of tool life but were 32% and 92.7% greater in $E_4$ and $E_5$ edges, respectively. By correlating the experimental result with the numerical analysis, it can be inferred that temperature driven wear mechanism commences at an edge radius of 40-55µm.

The size of the stagnation zone is directly related to the ploughing behaviuor of the cutting tool. As the stagnation zone grows, more material will be pushed into the flank edge to produce the machined surface [42]. At a constant uncut chip thickness, the larger edge radius will produce more ploughing instead of cutting, thus consuming more energy. The ploughing behaviour will also cause an undesirable surface finish. It was reported that the ratio between the edge radius and the uncut chip thickness should be at least (1/4$^{th}$ -1/3$^{th}$ )

to avoid ploughing [93]. Therefore, at an uncut chip thickness of 1mm, the edge radius should be below 25 μm.

When the temperature of the tool tip and the area near the cutting edge reach their limit, the tool will lose its cutting ability under extremely high temperatures and cutting pressure. This is caused by the tool material undergoing plastic deformation at the tip as well as at points adjacent to the cutting edge. It has been found that the temperature increases as the tool wears out in all the cutting tools [94]. Out of all the prepared edges, the drag finished edge had the lowest maximum temperature of 960 °C on the cutting edge after a 50 m cut. Conversely, the unprepared sharp edge had the highest temperature of 1207 °C. Furthermore, the temperature increase of the unprepared tool was greater than that of the prepared tools. The simulation results are consistent with experimental studies, demonstrating that the tool wear rate is much higher in the unprepared cutting tool. The drag finished edge was also shown to have the lowest flank wear rate and the best edge condition.

The increase of effective stress indicates a greater probability of deformation in the cutting tool. The effective stress on the cutting tool indicates the risk of plastic deformation and damage to the cutting tool [7]. The maximum effective stress in the drag finished prepared tool was lower than other cutting tools which corresponds to its lower probability of being damaged. The experimental study also revealed that the unprepared cutting edge underwent catastrophic failure at the end of the cutting, perhaps due to the maximum effective stress (von Mises) being present on the unprepared edge in the simulation. At the beginning of the cut, the stress on the unprepared cutting tool was concentrated on the tool tip. This stress behaviour could be a potential cause of higher tool wear at the beginning of the cut in the unprepared cutting tool. However, consistent excess cutting pressure along with vibration can substantially contribute to premature sudden tool failure. Finally, the prepared edges that were exposed to lower stresses tend to undergo a more stable cutting process and had a lower flank wear growth rate.

# CHAPTER 5. EFFECT OF PRE-COATING EDGE PREPARATION

As discussed in an earlier chapter, edge preparation can improve tool life to some extent during the machining of AISI 4140 with an uncoated carbide tool. It has been reported that the application of coatings during the turning of 4140 benefited tool life [95]. Therefore, it is highly likely that a combination of edge preparation and coating can further improve tool life. This chapter presents an experimental study on the prepared coated tool's effect on tool life. A numerical study has also been performed to understand the thermo-mechanical behaviour of the variously prepared coated tools.

## 5.1 Experimental set-up

An experimental study of the prepared edge was carried out using an abrasive jet machining edge preparation process. A PVD coating was deposited on the generated cutting edge, which was then evaluated. Tool life studies were conducted to identify the wear progression for prepared and unprepared coated tools. Detailed analyses were subsequently performed to assess the possible benefits of pre-coating edge preparation.

Orthogonal turning experiments were performed on a Nakamura-Tome SC-450 CNC lathe center as Fig. 48(a) shows. The grooving process experimental setup is shown on the front view of Fig. 48(b). AISI 4140 steel whose chemical composition is given in Table 9, was used as the workpiece in all cutting experiments.

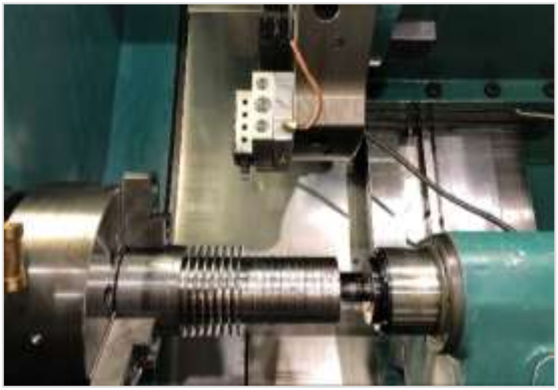

(a)

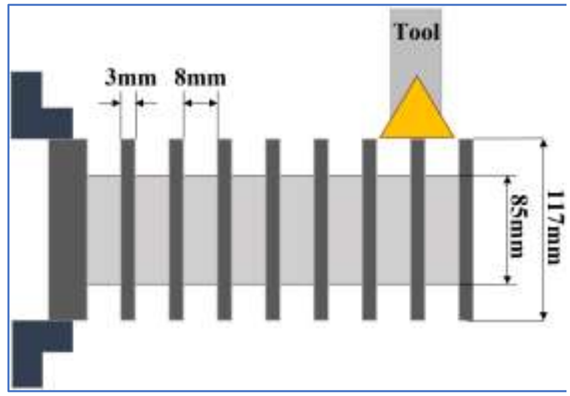


(b)

Figure 48: (a) Machining setup and (b) workpiece.

Edge preparation and coatings were applied on Kennametal TPG 322 uncoated cemented carbide inserts of grade K313 with 6% Co. Orthogonal turning tests were performed at a 0.2 mm/rev feed rate, a 3mm depth of cut and a 350 m/min cutting speed.

Table 9: Chemical composition and mechanical properties of AISI 4140 steel. [96]

| **Chemical composition (%)** | | | | | | | | |
|---|---|---|---|---|---|---|---|---|
| ***Element*** | ***C*** | ***Si*** | ***Mn*** | ***P*** | ***S*** | ***Cr*** | ***Ni*** | ***Mo*** |
| **Weight %** | 0.38-0.43 | 0.15-0.32 | 0.75-1.00 | Max 0.035 | 0.04 | 0.80-1.08 | 0.16 | 0.15-0.25 |

## 5.2 Coated tool samples

The cutting-edge samples were prepared by pressurized air wet abrasive jet machining in collaboration with the Institute of Machining Technology, TU Dortmund University, using a Nicolis technology wet abrasive jet machine with an adapted 6-axis robot control. The abrasive is mixed in water and pressurized with compressed air.

The microstructure of the cutting-edge surface changes during edge preparation, influencing coating adhesion. This study examines the benefit of edge preparation on the cutting tool as a pre-treatment prior to physical vapour deposition. AlTiN coatings with a thickness of 1 μm were produced by a cathodic arc ion plating process using a Kobelco AIP-S20 deposition system. Coatings were deposited on both unprepared and AJM prepared uncoated inserts using an arc evaporation source produced by powder metallurgy composed of 50% Ti and 50% Al. The uncoated inserts were cleaned and mounted inside the deposition chamber, before being preheated to 450 °C. The Ar-$N_2$ etching pressure was 3.2 Pa. Other parameters of the deposition process are listed in Table 10.

Table 10: Coating deposition process parameters

| **Table rotation speed** | **Bias voltage** | **Arc source current** | **Total deposition time** | **Coating thickness** |
|---|---|---|---|---|
| 3 rpm | -15 V | 150 A | 25 min | 1 μm |

The edge geometry of all unprepared and prepared inserts was measured with an Alicona microscope. The sample edges were labeled as Tool 1, Tool 2, and Tool 3. Tool 1 represents the unprepared coated edge used as a benchmark in this study. The measured values of all edge geometry parameters for the form factor method are given in Table 11.

Table 11: Measured K-factor parameters and edge radius of the cutting tool sample edges.

| | **Actual measured parameters for the K-factor method** | | | | **Edge radius** |
|---|---|---|---|---|---|
| | $K$ | $\bar{S}$(μm) | $S_\alpha$ ($\mu m$) | $S_\gamma$ ($\mu m$) | $r_\beta$ ($\mu m$) |
| **Tool 1** | 1.11 ± 0.06 | 7.31 ± 0.37 | 6.93 ± 0.33 | 7.68 ± 0.50 | 5.83 ± 0.23 |
| **Tool 2** | 0.94 ± 0.01 | 24.40 ± 0.30 | 28.30 ± 0.30 | 26.49 ± 0.42 | 21.85 ± 0.41 |
| **Tool 3** | 0.96 ± 0.01 | 48.38 ± 0.11 | 49.30 ± 0.12 | 47.47 ± 0.16 | 38.82 ± 0.26 |

## 5.3 Experimental results

### 5.3.1 Tool life comparison

The results of the tool life study are presented in this section. First, a set of tool life tests was performed on coated unprepared tungsten carbide inserts as the benchmark. Next, machining tests were conducted on inserts with different prepared edges, and their performance was compared with the benchmark tool. During these orthogonal turning tests, maximum tool flank wear was monitored and measured after each pass (at lengths of cut of around 1.4 m to 1.8 m) using a Keyence VHX-5000 digital microscope. Fig 49 shows the tool life studies of all the cutting inserts.

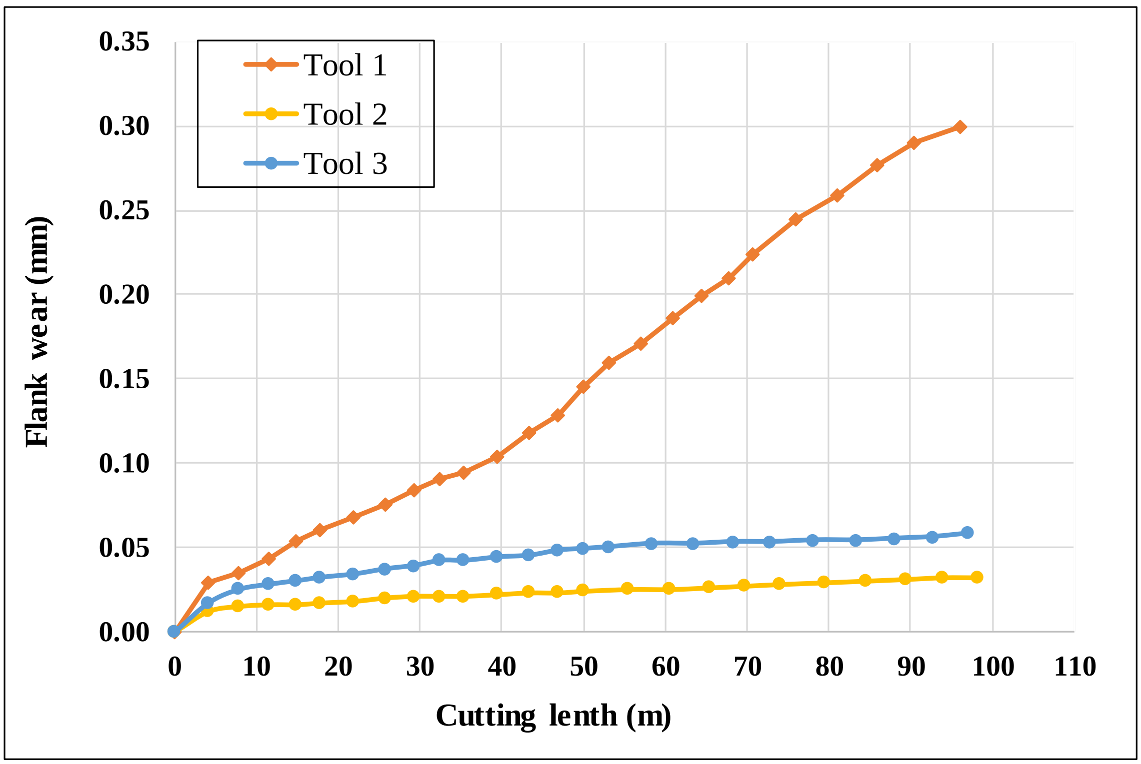


Figure 49: Flank wear progression along the cutting length for coated tool

The tool life study demonstrated that the unprepared coated edge (Tool 1) flank wear reached 300 µm after a cutting length of 100m, indicating the end of tool life. Moreover, there was no stable stage during the entire tool lifespan, with flank wear continuing to grow at a high rate. Tool 2 and Tool 3 edges had negligible flank wear rate compared to the Tool 1 edge. The prepared coated tool (Tool 2) with an edge radius of 21.85 had the lowest flank wear until 100 m of cut was reached.

### 5.3.2 Cutting forces analyses

The change in cutting force during tool wear was measured by a KISTLER dynamometer with the root mean square results of cutting force being recorded. All the cutting forces exhibited an incremental trend as the tool wears out, as can be seen in Fig. 50.

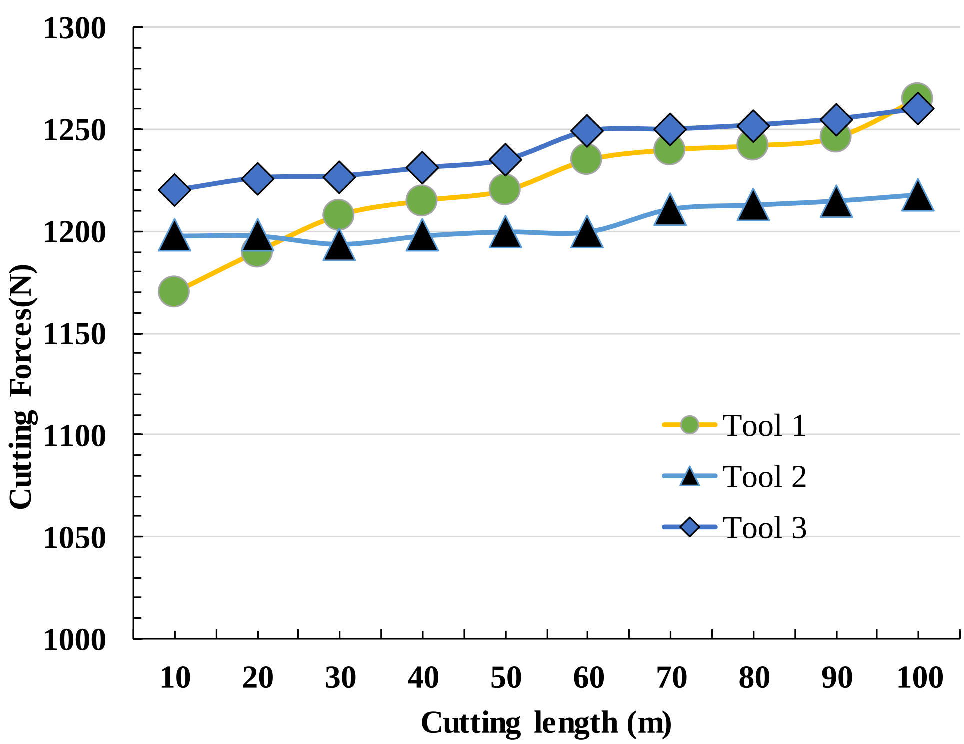


Figure 50: Cutting force variation along with tool wear for coated tools

However, the cutting force of Tool 1(unprepared) showed a higher increment (1165N-1265N) than the other prepared tools. This behaviour corresponded to the greater tool wear observed in Tool 1.

## 5.4 FE modelling of the coated tool

The cutting tool was modeled as one part containing two different sections. The lower part of its mesh will be in contact with the workpiece. As such, it was represented with a very fine mesh, so that effect of the coating on the cutting tool could be assessed. The first section contains two sets of thin elements on the cutting tool top surface adjacent to the workpiece. Each element had a thickness of 0.5μm starting from rake face to flank face, see Fig 51. The second section had the definition of the substrate material. The entire tool has 4765 elements. The coefficient of friction was assumed to be μ= 0.4 [23] for all the simulation performed in this study. Since comparison was made among the coated tools, the value of COF (μ) didn't affect the objective of this study.The material properties of the coating were applied with references from literature as shown in Table 12.

Table 12: TiAlN coating properties [76]

| Density | Young's modulus, E | Poisson's ratio, ν | Specific heat capacity[97] | Thermal conductivity |
|---|---|---|---|---|
| $Kg/m^3$ | GPa | - | J/kg°K | W/m°K |
| 5400 | 557 | 0.25 | 779 | 5.6 |

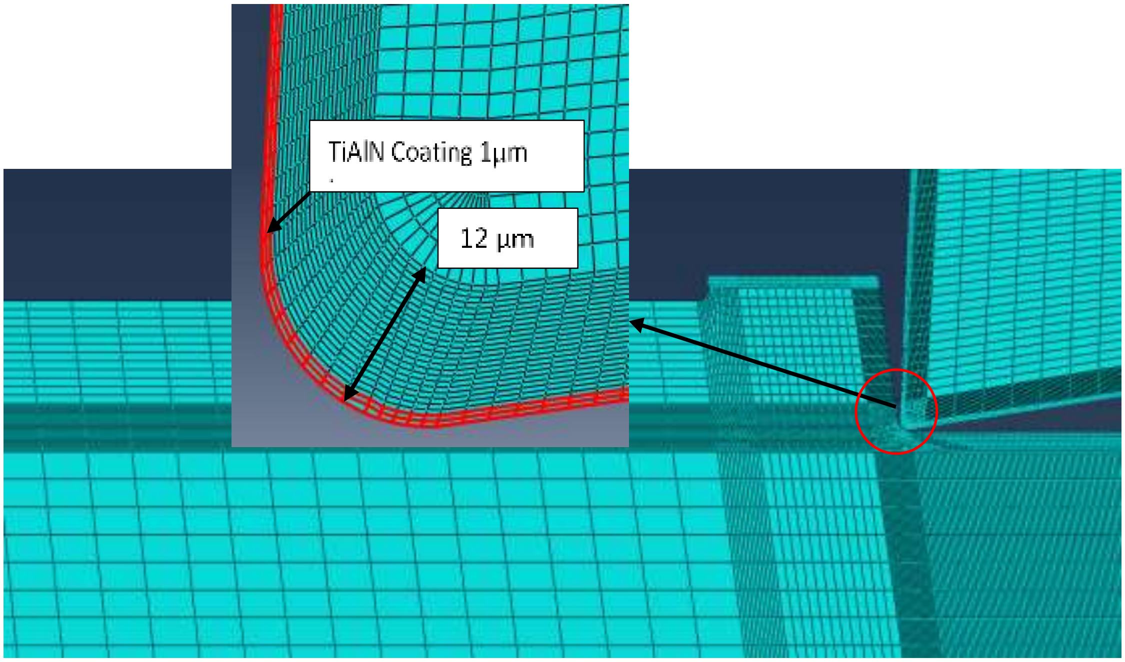


Figure 51: FE mesh of the workpiece and the tool with a 1µm thick mono-layer coating.

## 5.5 Thermo-mechanical behaviour

To understand the experimental tool wear behaviour, an FEA thermo-mechanical study was conducted in two steps based on a similar modeling technique used for the uncoated tool. First, the change in maximum effective stress (VM stress) and temperature over the course of Tool 1's cutting length was recorded. Next, a comparative study of the three tools thermo-mechanical behaviour was performed.

### 5.5.1 Coated tool with Tool 1 (unprepared) edge

The trend for maximum temperature was almost identical to that of von Mises stress as shown in Fig. 52. The flank maximum temperature found on the new tool was around 720 ºC. However, as tool wear increased, so did the maximum temperature of all the cutting edges.

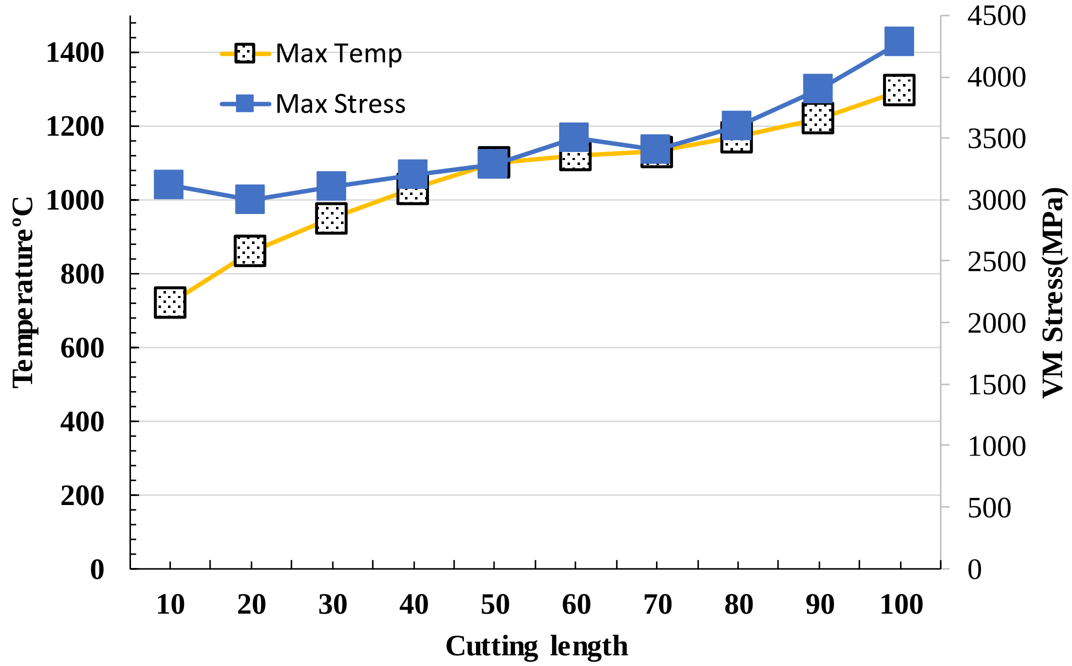


Figure 52: Temporal variation in maximum temperature and VM stress on the flank face.at different cutting length

The maximum temperature was found on the rake face during the initial stage of wear. The spatial temperature distribution showed that the maximum temperature shifted from the rake face to the flank face, see Fig. 53(a-c). Similar behaviour was reported in a different study [44] .Peak VM stress increased with tool wear at distinct cutting lengths, as shown in Fig. 50.The maximum stress on the flank face of the new tool was found to be about 3140

MPa, increasing to around 3400 MPa and 4300 MPa at cutting lengths of 50 and 100m, respectively. Also, the maximum stress of the new tool was found to be concentrated on the tool tip. At the initial stage of wear the maximum stress was distributed on both the rake face and the tool tip. However, the location of maximum stress tended to change from the rake face to flank face as the tool wear increases, see Fig. 53(d-f).

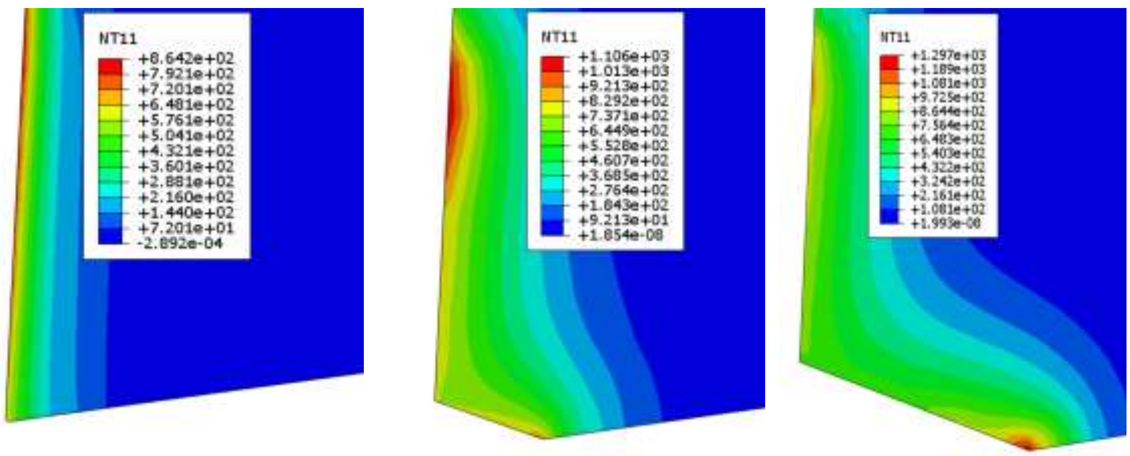


a) Temperature(ºC) new tool b) Temperature(ºC) @50m c)Temperature(ºC) 100

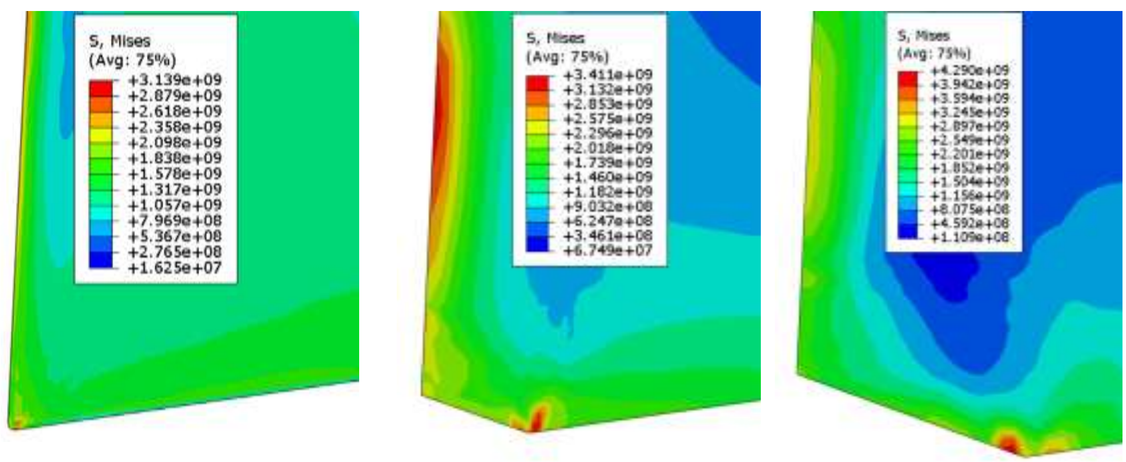


d) VM Stress (Pa) @new tool e) VM Stress (Pa) @50m f) VM Stress (Pa) @100m

Figure 53: Spatial variation in maximum temperature and VM stress on the cutting edge.

### 5.5.2 Coated tools with prepared edges

**Cutting forces:** The simulation result revealed that cutting forces were higher for higher edge radius, which was confirmed by experimental findings. The maximum error difference between the numerical prediction and experimental observation at the initial stage of wear was less than 5%. As the cutting tool wore out, the cutting force on Tool 1 increased rapidly. However, the change in cutting force was insignificant for Tool 2 and Tool 3, see Fig. 54. The numerical study showed that the cutting force increased by almost 20% at the end of Tool 1's life. However, the experimental observation was less sensitive than the numerical one.

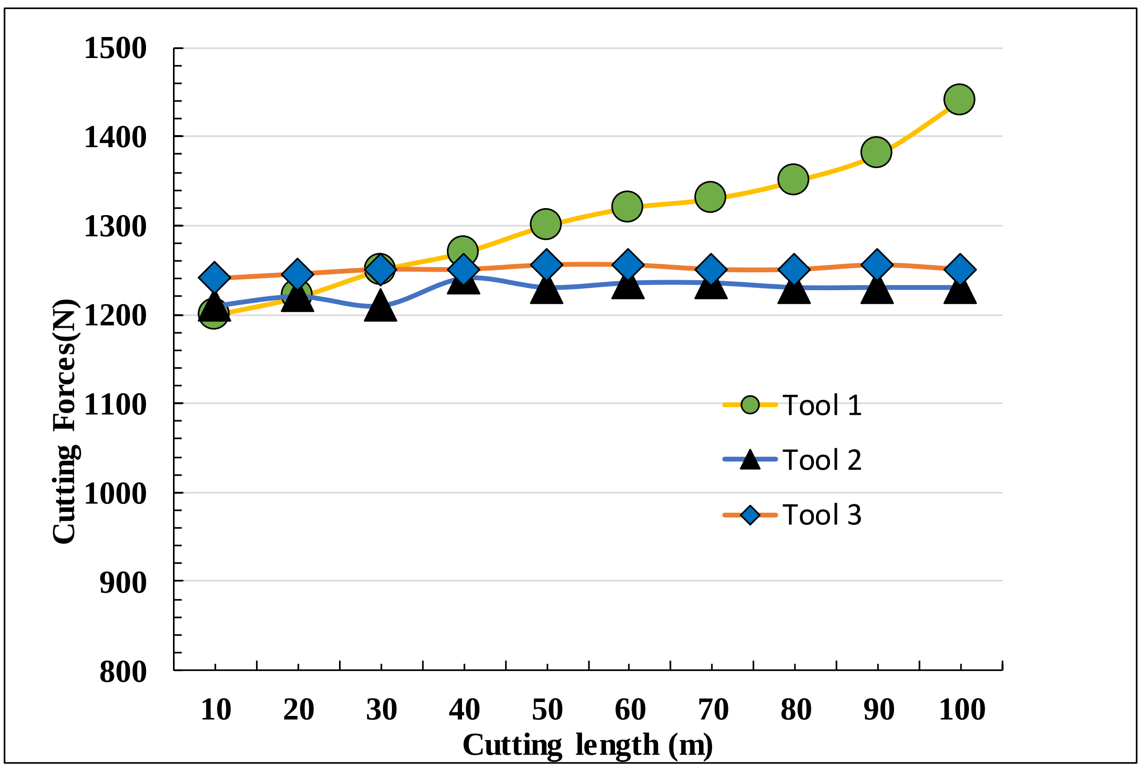


Figure 54: Temporal variation of cutting forces at different cutting length

**Thermal behaviuor:** The thermal behaviour of differently prepared coated tools was investigated in this study. At the beginning of the cut, Tool 1 and Tool 2 maximum temperature were lower than that of the prepared coated Tool 3, see Fig. 55.

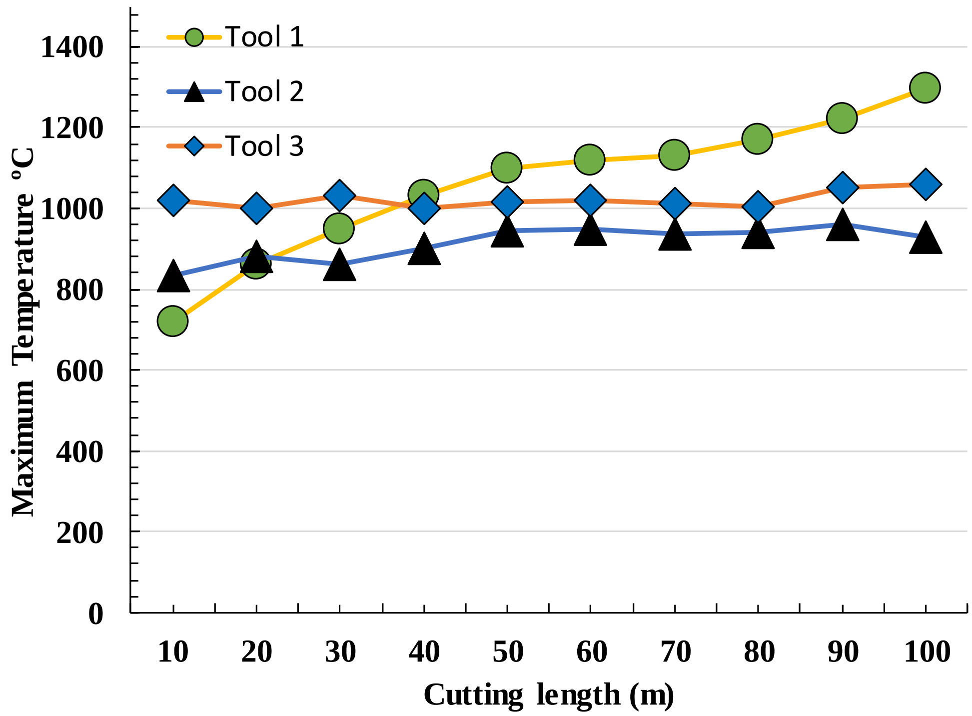


Figure 55: Temporal variation of Maximum temperature on flank edge at different cutting length

However, as wear in the cutting tool progressed, the maximum temperature growth on the unprepared tool was higher than that on the any other prepared tools. The simulated maximum temperature on the worn tool increased by nearly 82% at 100m compared to the new tool [60]. The temperature on the prepared cutting tools remained almost equal to that on the new tool throughout the entire cutting length.

**Stress field:** Figure 56 shows the predicted maximum von Mises stress along the cutting length. It has been observed that the maximum von Mises stress was higher in Tool 1 and Tool 3 than Tool 2 cutting tool at new tool.

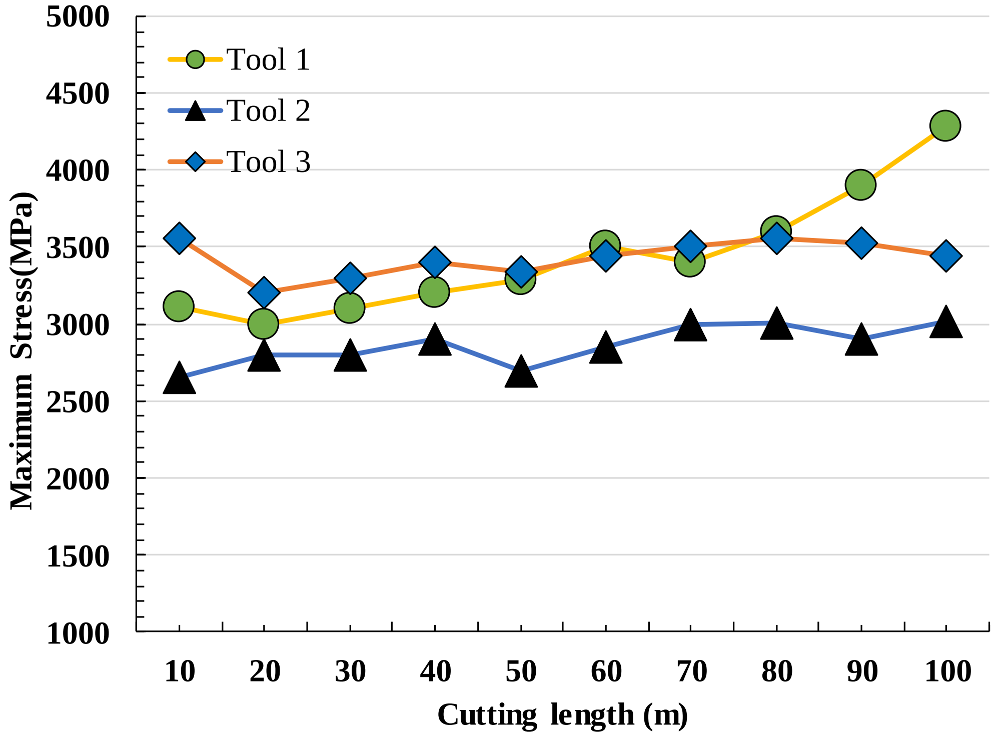


Figure 56: Variation of Maximum Stress at flank edge over the different cutting length

Although, the maximum von Mises of Tool 1 increased by almost 37% after a length of cut of 100m, the maximum stress for prepared edges remained almost the same in magnitude throughout the length of cut. Figure 57 shows the spatial view of the cutting tool at 100m of cut in both prepared and unprepared cutting tools. Changes in geometries of the prepared cutting tools were almost negligible with the proposed tool updating technique.

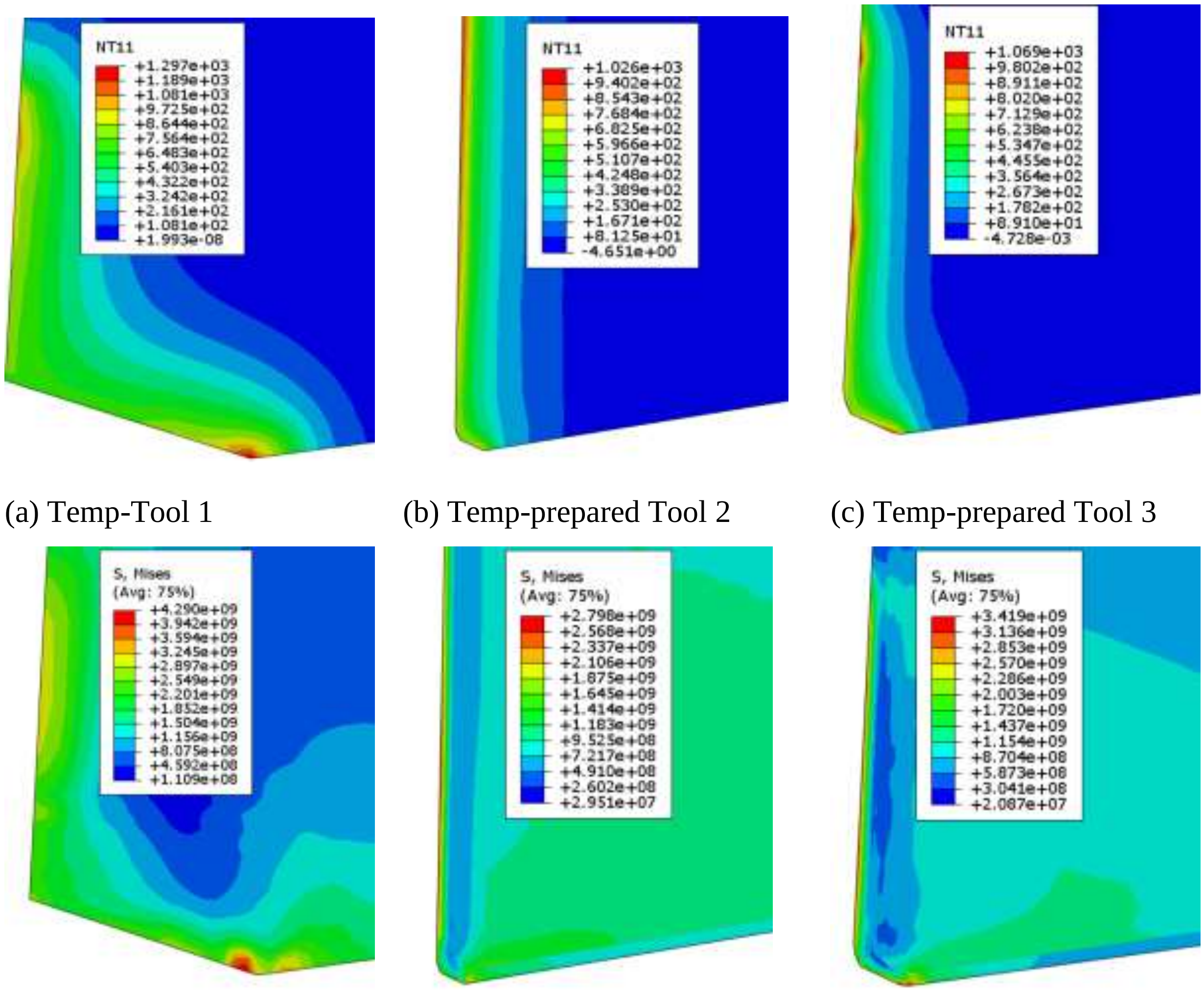


(d) VM stress (Pa)-Tool 1 (e) VM stress (Pa) -Tool 2 (f) VM stress (Pa) -Tool 3

Figure 57: Spatial variation in maximum temperature and VM stress on the cutting edge at cutting length of 100m

Fig. 58 shows the temperature distribution near tool tip. The flank face was represented by negative distance, whereas the rake face was denoted by the positive distance. It can be clearly observed that Tool 3's temperature was the highest and Tool 1's temperature was the lowest at the tool tip.

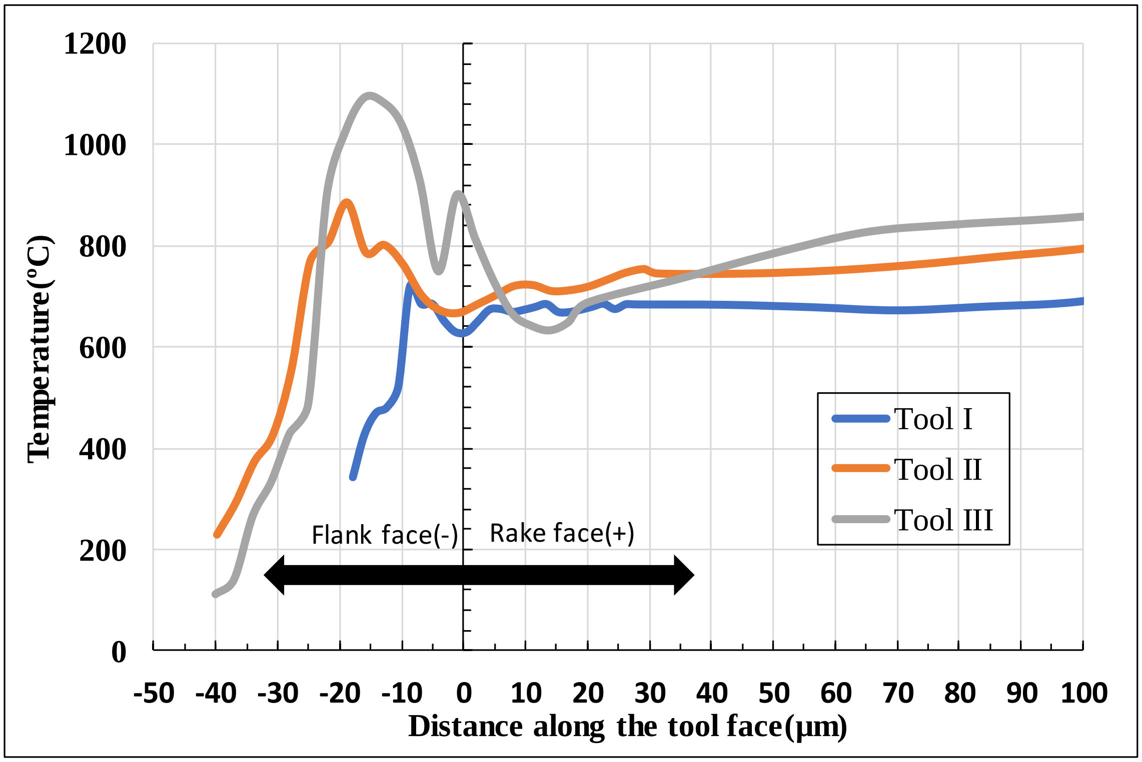


Figure 58: Spatial temperature profile on three different cutting tools

The von Mises stress profile on the flank edge was evaluated in all the new tools, see Fig. 59 and Fig. 60. The von Mises stress of the unprepared coated tool(Tool 1) was concentrated throughout the flank edge. However, the von Mises stress of Tool 2 was roughly lower at the tool tip than in other tools (Tool 1 and Tool 3). The stress was more evenly distributed in Tool 2 and Tool 3 than in the unprepared cutting tool (Tool 1).

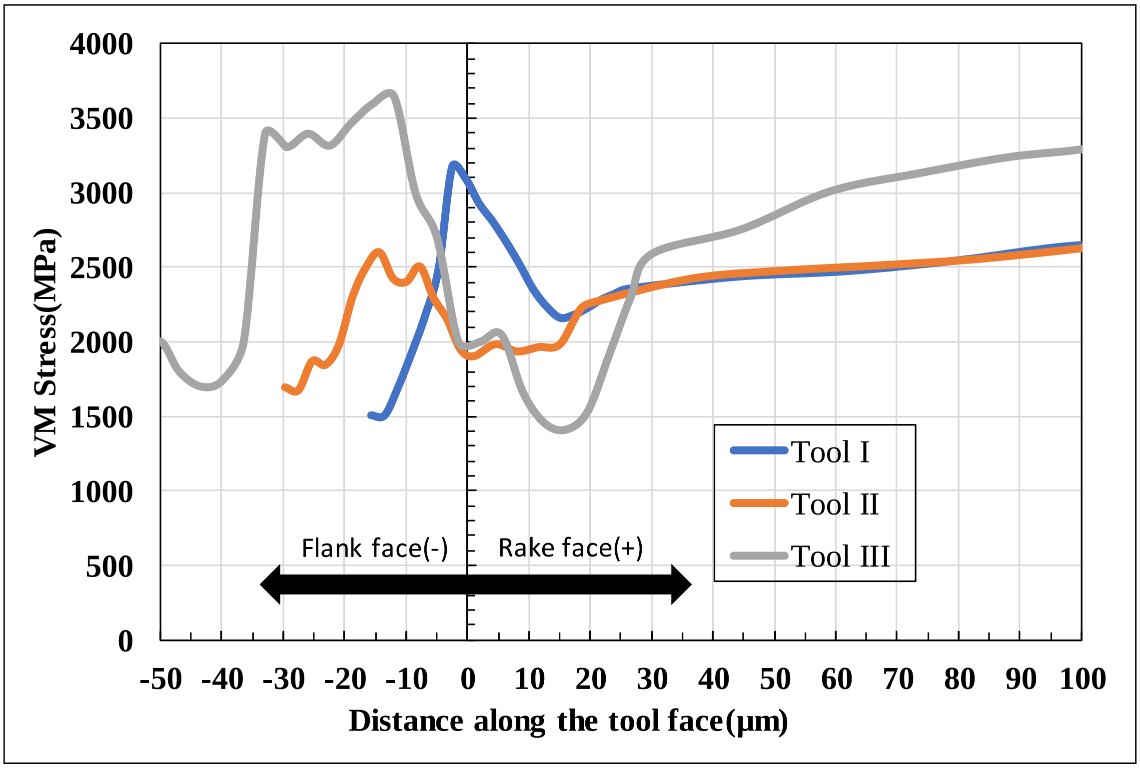


Figure 59: Spatial stress profile on three different cutting tools

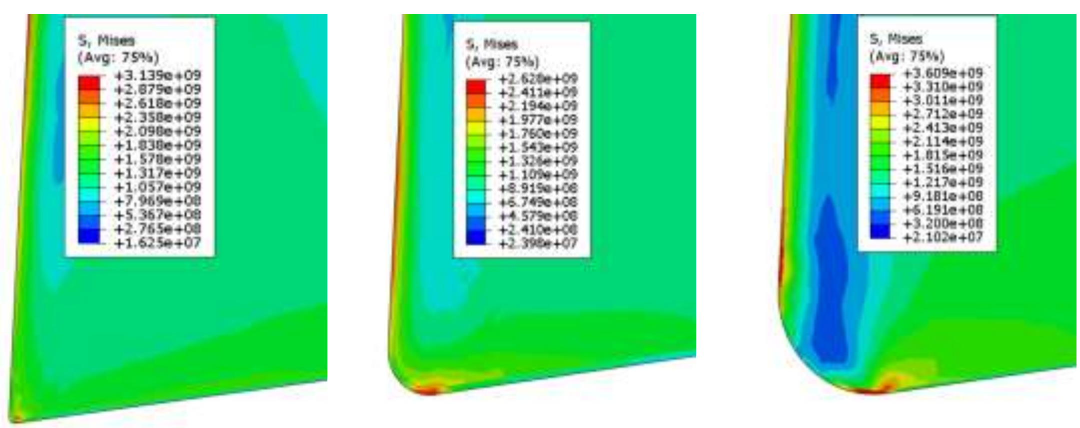


Tool 1 Tool 2 Tool 3

Figure 60: Spatial views of VM stress (Pa) of initial cutting edges

## 5.6 Coated Vs. Uncoated tool thermo-mechanical behaviour

The simulation of the uncoated tool was performed with the same interaction properties as coated tool (Tool 2) to compare the thermo-mechanical behaviour due to the added layer of coating. Fig. 61 shows the temperature and stress within the tool, starting at point P and proceeding inward. Point p was evaluated from the flank face. Temperature and stress reduced within the interior of the tool. The difference in tool surface temperature between the coated and the uncoated tool was almost 50 °C, the coated tool showing the higher temperature. The temperature of the coated tool significantly dropped in the second element row. The temperature decreased after two element rows (i.e. one μm) by 240 °C in the coated tool and 140 ºC in the uncoated tool. However, no significant difference in stress value was observed.

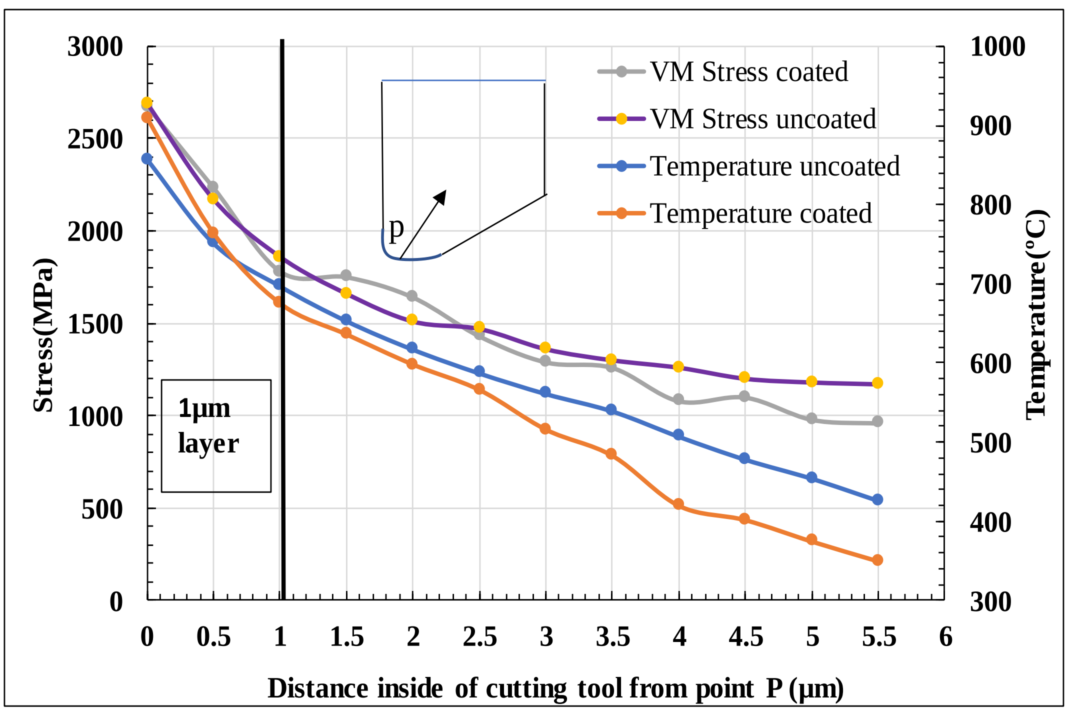


Figure 61: Temperature and stress distribution interior of the tool along with path p

## 5.7 Discussion

An orthogonal cutting model of machining AISI 4140 is presented in this study for two prepared and one unprepared coated tools. The cutting tools were coated with TiAlN coating of 1μm thickness. Tool life improved significantly for the coated tools with prepared edges. Numerically estimated cutting force results showed good agreement (less than 5% error) with the experimental result at the initial stage of tool wear. This chapter investigated the effect of edge preparation on the thermo-mechanical properties of the coated tool, from which the following conclusions can be drawn:

- The predicted von- Mises stress indicated that the unprepared tool (Tool1) tended to have greater stress concentration on the tool tip than the prepared (Tool 2) tool. The experimental study showed that the unprepared cutting tool has higher flank wear and tendency to chip. It can be inferred from the numerical study that the higher stress concentration on the tool tip of the unprepared cutting tool increased the possibility of cracking and delamination in the coating. Application of a prepared cutting tool bypassed the chipping tendency during the initial stage of tool wear. Since the industry standard edge radius is 25 μm, any edge radius close to that value might produce a lower stress concentration [60]. The present numerical study exhibited an almost identical low concentration of stress in Tool 2, which may account for its superior performance. The maximum temperature and VM stress increased in the unprepared cutting tool as it wore out, suggesting a higher probability of ultimate catastrophic failure.

- As edge radius increased, the temperature and stress also grew on the flank faces of the prepared edges. The experimental study found that the tool wear was higher for the 40 µm than the 20µm prepared cutting tool. The higher cutting temperature and stress of the 40 µm cutting tool might result in greater tool wear compared to the 20µm cutting tool.

- A comparative study of the thermo-mechanical behaviour revealed that the coating reduced the surface temperature on the tool substrate, which eventually improved the tool life of the coated tool.

# CHAPTER 6. TOOL WEAR PREDICTION

In this chapter, tool wear predictions were made based on the thermo-mechanical behaviour of the worn tool. The tool wear was calibrated using a hybrid calibration method. The predicted tool wear was validated at different cutting speeds. A parametric study was conducted to assess the thermo-mechanical tool wear behavior at different cutting parameters.

## 6.1 Wear model

The tool wear rate was calculated based on the thermo-mechanical load obtained from a 2D orthogonal cutting simulation using a tool wear equation. There are several standard tool wear equations mentioned in literature. However, tool wear models are not the sole focus of this chapter. The Usui tool wear equation (Equation 22) has been selected for this study due to its superior tool wear prediction accuracy [11], [70].

$$\dot{w} = A\sigma_n V_S exp\left(-\frac{B}{T}\right) \tag{22}$$

The Usui tool wear equation is a function of:

$\sigma_n$ = contact normal stress (MPa)

$V_S$ = Avergae sliding velocity on the flank face ($\frac{\text{m}}{\text{s}}$)

T = Average temperature generated at the cutting zone (ºC)

$\dot{w}$ = wear rate ($\frac{\text{m}}{\text{s}}$)

A, B = Calibrated Modelling Constant

## 6.2 Tool wear calibration

A hybrid calibration method was used in this study to calibrate the tool wear model on the basis of both simulation outputs and experimental results. Figure 62 shows the schematic diagram of the hybrid calibration method. As mentioned in the previous section, Usui's model has been calibrated to predict the tool wear.

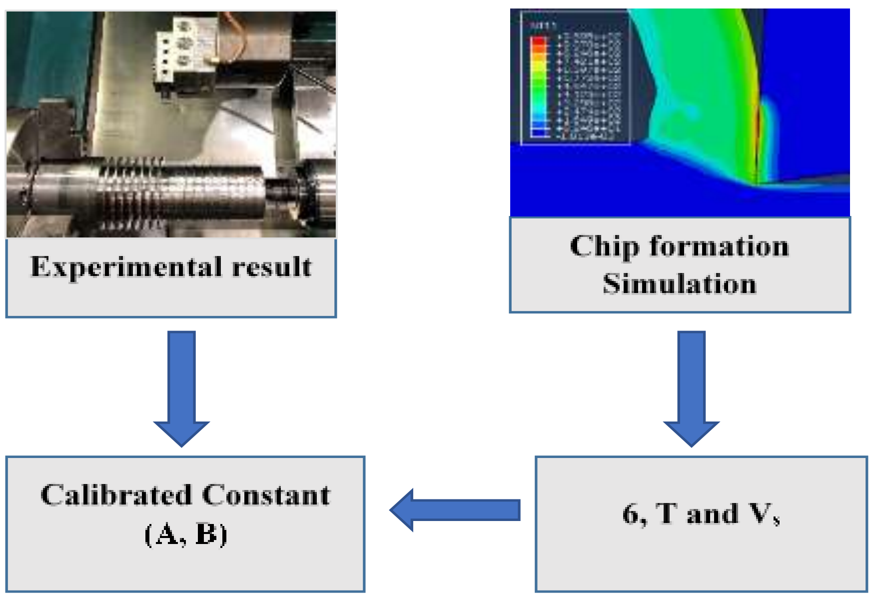


Figure 62: Schematic diagram of the hybrid calibration technique

The Usui model has two constants, A and B, which must be calibrated for a specific combination of the workpiece and the cutting tool. To obtain the values of A and B, a semi-logarithmic function (Eqn.23) will be approximated by a straight-line using regression analysis.

$$\ln(K) = ln\left(\frac{\dot{w}}{\sigma_n V_s}\right) = ln(A) - B\left(\frac{1}{T_{int}}\right) \quad (23)$$

Fig. 63 represents the relationship between the specific wear rate (K) and inverse temperature (1/T). The specific wear rate is a function of the experimentally measured wear rate ($\dot{w}$), numerically estimated contact stress ($\sigma_n$) and sliding velocity ($V_S$) at a user defined discrete time interval (Δt). The experimental tool wear corresponds to the changes in cutting tool geometry and mechanical properties of the cutting edge [81]. The thermo-mechanical output of the chip formation simulation was the main source of the change in cutting edge geometry. Since, the constants A and B were calibrated in terms of both tool wear and simulation output at different prepared edges, they account for the individual mechanical properties and the geometry of prepared edges. The constant A represents the impact of stress and sliding velocity and the constant B effect of temperature on tool wear progression. Table 13 summarizes the calibrated wear model constants for the unprepared and all four prepared tool inserts.

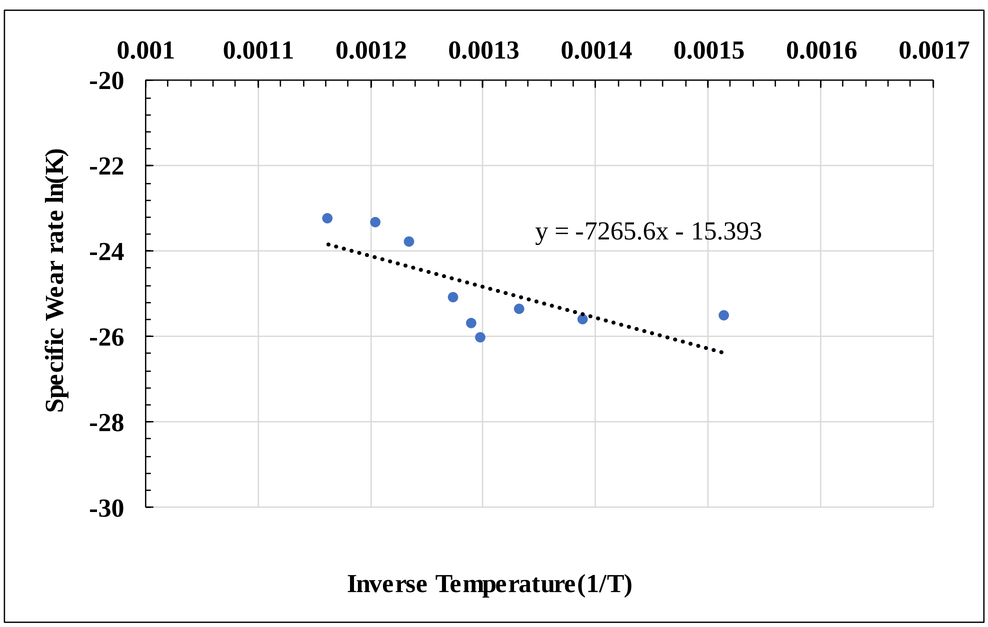


Figure 63: Hybrid calibration of Usui's model for the unprepared tool.

Table 13: Calibrated Co-efficient for unprepared and 5 different prepared edges

| | $E_0$ | $E_1$ | $E_2$ | $E_3$ | $E_4$ | $E_5$ |
|---|---|---|---|---|---|---|
| **A** | 2.06e-7 | 1.08e-7 | 1.33e-7 | 1.97e-7 | 1.153e-9 | 4.48e-9 |
| **B** | 7265 | 6915 | 7312 | 7312 | 4109 | 3604 |

## 6.3 Tool wear prediction

Fig. 64 represents the flow diagram of tool wear prediction. The temperature, stress and sliding velocity in the cutting zone were obtained from the chip formation simulation once it arrived at the steady state. The measured simulation output estimated the flank wear using the Usui model with the calibrated constant at a user-defined time step (Δt). The time step Δt was set to be 1s in the current study.

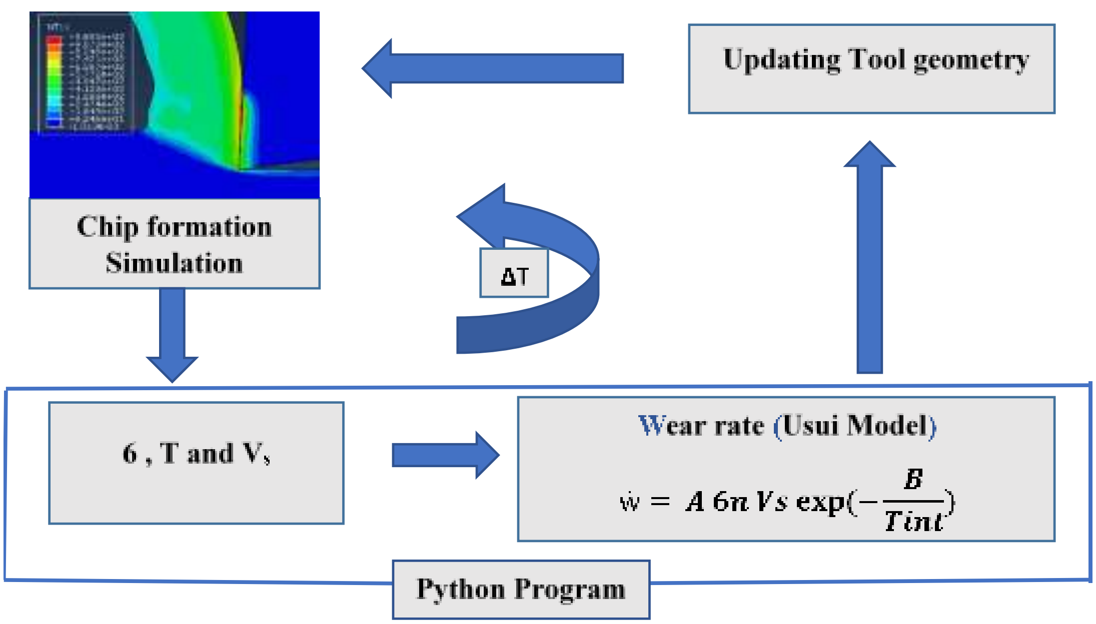


Figure 64: Schematic diagram of tool wear prediction

Once the predicted flank wear value was found, the cutting tool geometry was updated based on the tool geometry updating technique described earlier. After each cycle of time increment Δt, the flank wear ($V_{Bi}$) at a machining time $t_i$ was computed from:

$$V_{Bi} = V_{\mathbf{B(i-1)}} + \dot{w} * \Delta t \tag{27}$$

Where, $V_{\mathbf{B(i-1)}}$ is the flank wear at the beginning of the time increment (Δt). Fig. 65 shows the comparison of numerically predicted and experimentally determined tool wear results with respect to the cutting length. It is evident that the simulation can successfully predict the tool wear trend in the unprepared cutting tool. However, a deviation in magnitude exists. The RMSE (Root mean square error) and MAPE (Mean absolute percentage Error) value for the unprepared tool are 19 µm and 11.09% respectively. The prepared tool (E2) the RMSE and MAPE value are found to be 4.5 µm and 4.9%.

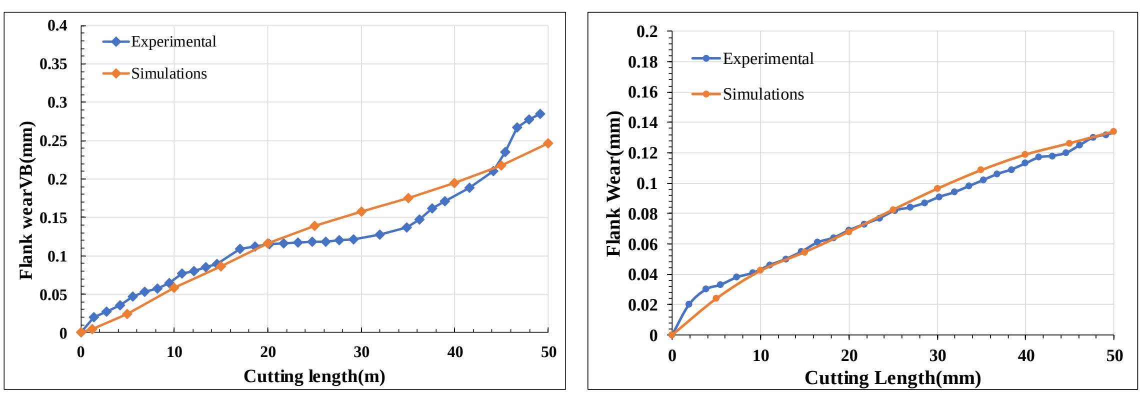


Figure 65: The comparison between experimentally and numerically measured tool wear at 300 m/min f=0.1 mm/rev for a) unprepared b) Prepared E2

Although the Usui model showed good agreement with the initial stage of tool wear, it showed poor prediction ability at the stable wear zone. This can be explained as the cutting tool was considered as an elastic body, it is unable to simulate thermo-mechanical effect damage mechanism at different stage of wear.

## 6.4 Validation of flank wear

The tool wear validation test was performed at a speed of 350 m/min with the results reported by Deng [98]. A similar cutting tool was used in that study to observe tool wear progression at a speed of 350 m/min. It was found that the progress of flank wear can be predicted with an RMSE and MAPE value of 25.7 µm and 14.16% compared to the experimental result using the same A, B wear model constants found for unprepared tool, see Fig. 66. The discrete-time step for predicting tool wear was kept at 1.0 s.

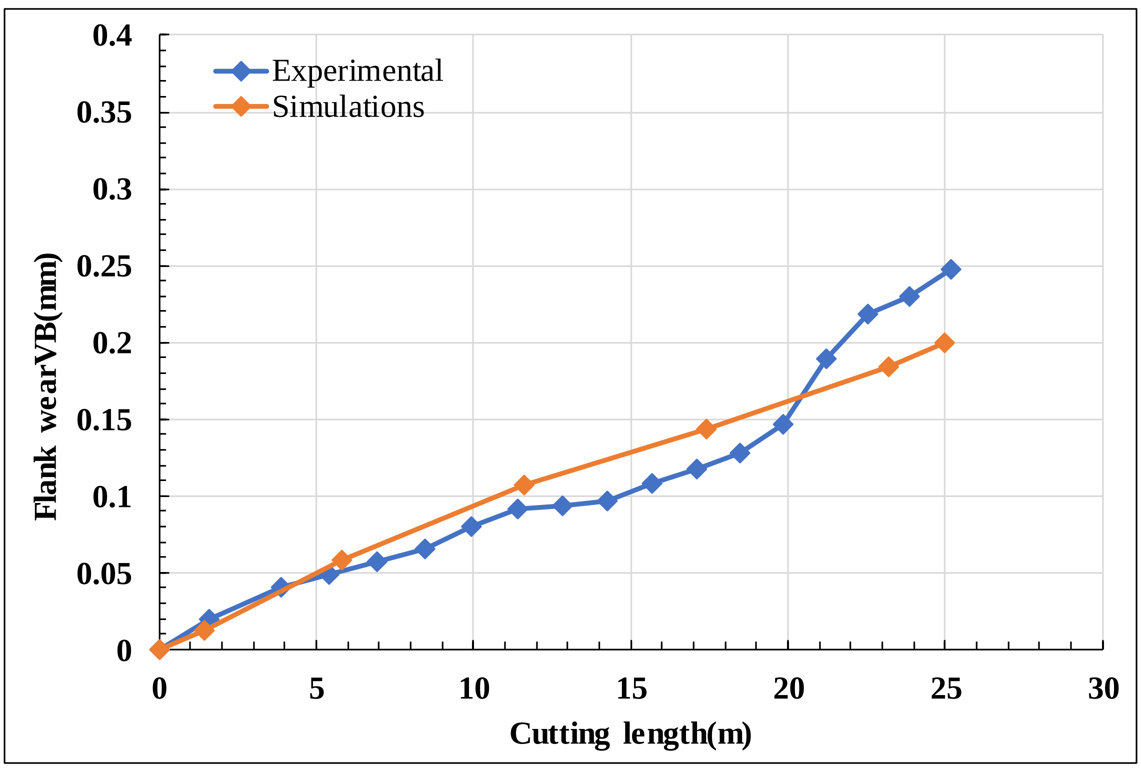


Figure 66: Prediction of Flank wear at speed of 350 m/min and feed rate of 0.1 mm/rev

## 6.5 Effect of process parameters on tool wear

In this chapter, the changes in tool wear due to different cutting parameters were evaluated by observing the thermo-mechanical behavior on the cutting edges. To investigate their effect on tool wear, five different cutting parameters were simulated. Since, the tool wear prediction was already validated, no further validation tests were needed under the current cutting parameters.

Table 14: Simulation tests with various cutting speed and feed

| Number of simulation test | Cutting speed (m/min) | Feed rate(mm/rev) |
|---|---|---|
| 1 | 250 | 0.1 |
| 2 | 300 | 0.1 |
| 3 | 350 | 0.1 |
| 4 | 300 | 0.15 |
| 5 | 300 | 0.2 |

**Tool wear progression**

The tool wear was predicted at three different cutting speeds and feeds up to a cutting length of 30m see Fig. 67, which is the experimental end of tool life at a speed of 350 m/min. Tool wear was found to significantly increase with cutting speed. At 350 m/min, cutting tool reached a flank wear value of VB=230µm. As speed was reduced to 300 m/min, the flank wear value subsided to 155 µm. At 250 m/min, tool wear significantly decreased to a flank wear value of 75 µm.

Tool wear also increased along with the feed rate. When the feed rate changed from 0.1mm/rev to 0.15 mm/rev and 0.2 mm/rev, flank wear reached 200µm and 240µm respectively after 30m of cut. At the same material removal rate (MRR), the tool wear was more sensitive to cutting speed than feed rate.

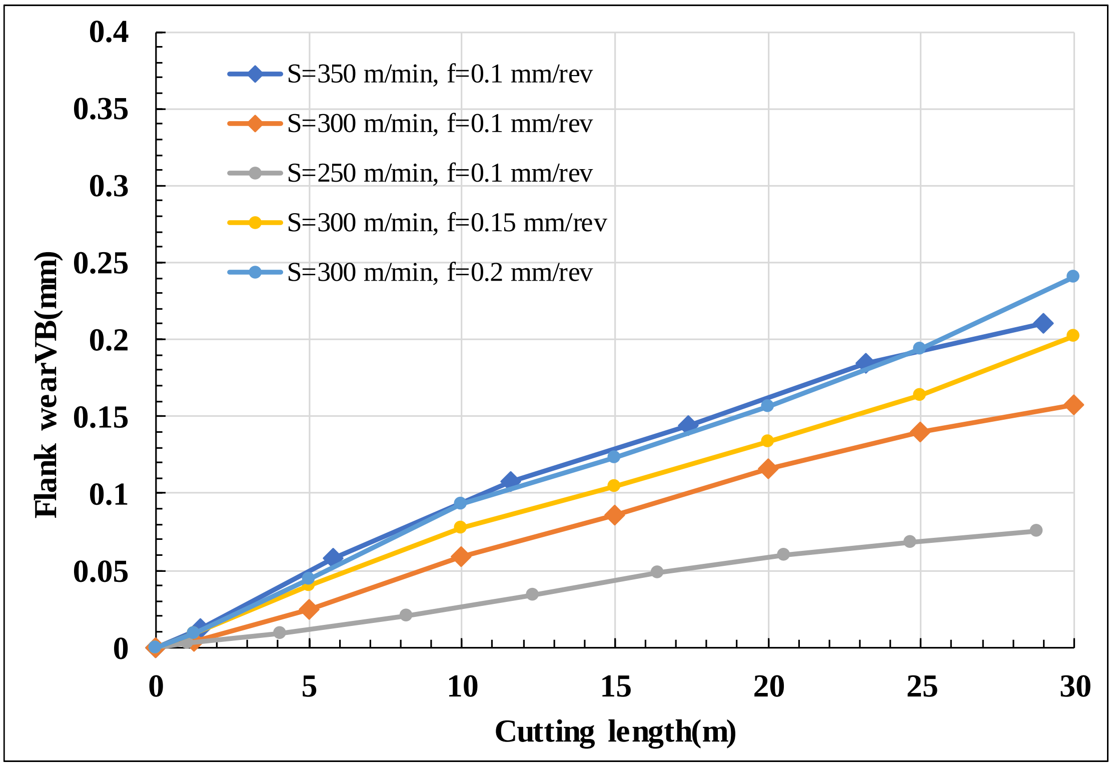


Figure 67: Simulated effect of cutting speed and feed rate on the tool wear

**Temperature and Stress behavior**

Fig. 68 shows the extracted average interface temperature on the tool flank face at different cutting speeds. The average cutting temperature increased with cutting length in all cases. Although the interface temperature was found to significantly increase along with cutting speed , it was less sensitive, with the increase of the feed rate.

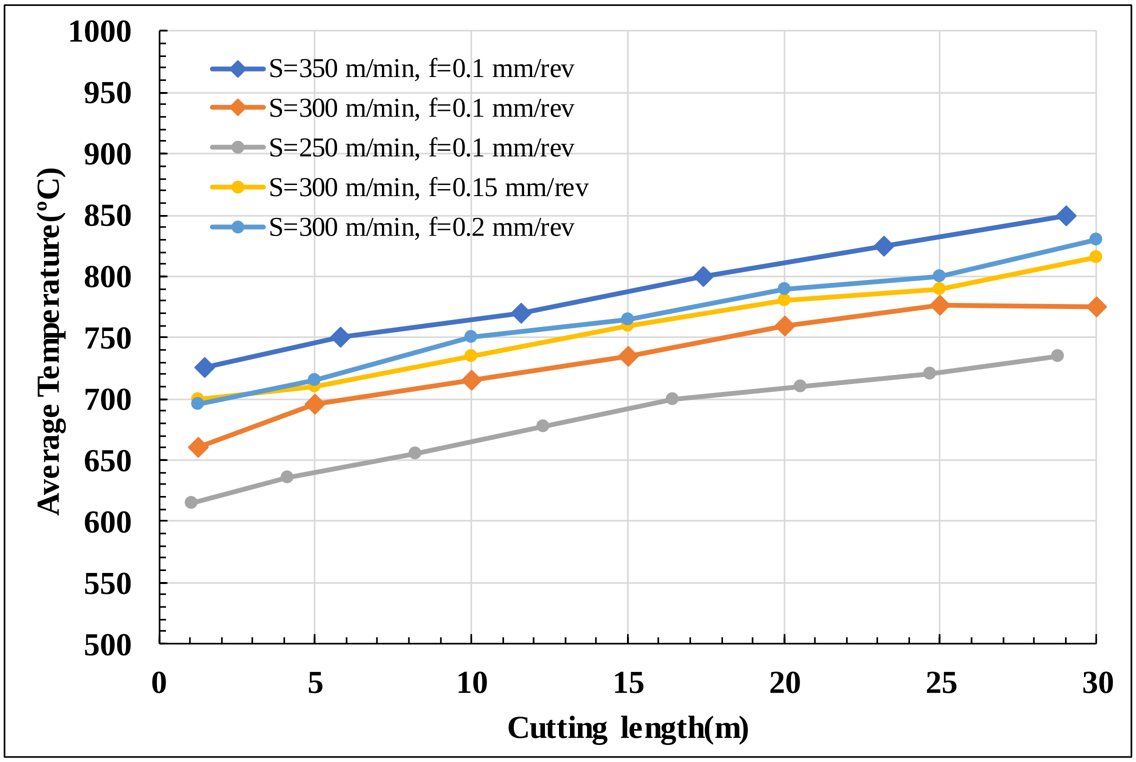


Figure 68 : Effect of cutting speed and feed rate on the temperature at different cutting length

Fig. 69 shows the change in temperature behavior due to change in cutting parameter at 75 μm of tool wear. At higher feed rate, the maximum temperature was shifted on the rake face of the tool. On the other hand, the position of maximum temperature didn't change with increasing cutting speed.

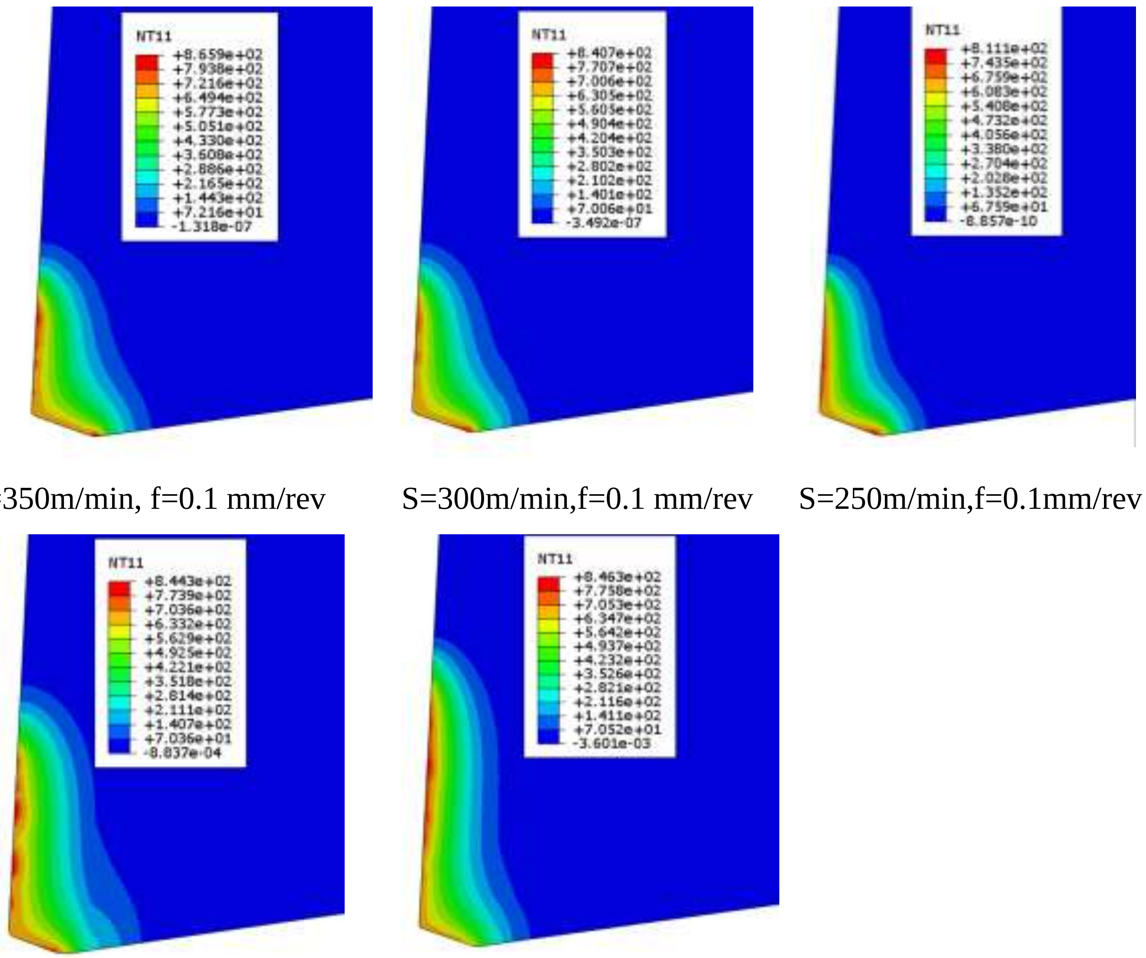

S=350m/min, f=0.1 mm/rev S=300m/min,f=0.1 mm/rev S=250m/min,f=0.1mm/rev

S=300m/min,f=0.15mm/rev S=300m/min, f=0.2 mm/rev

Figure 69: Spatial view of temperature(ºC) recorded at flank wear 75µm at different cutting parameters

In Fig. 70, the average contact stress increased with cutting length at all cutting speeds. The magnitude of contact stress at the beginning of the cut was less at a lower cutting speed of 250 m/min. Overall, no significant change in contact stress was observed as the cutting speed changes. However, the average contact stress increased as the feed rate grew from 0.1 to 0.2 mm/rev. This is due to the higher mechanical loads acting on the cutting tool at a higher feed rate.

The increase of average temperature and contact pressure along with feed rate was also reported in an earlier study [64].

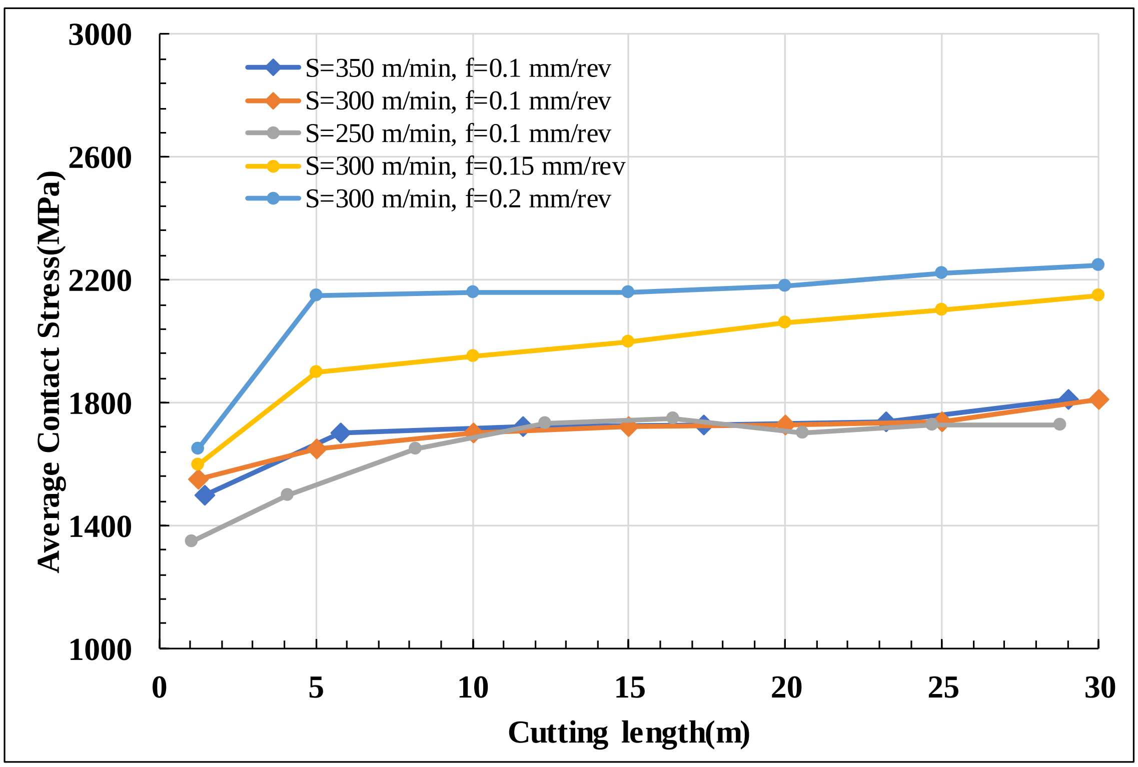


Figure 70: Effect of cutting speed and feed rate on contact stress at different cutting length

## 6.6 Discussion

In the previous study of FEA, up to 25% error of predicting tool wear was reported [67].By comparing previously reported literature with present study, it can be concluded that the hybrid calibration method presented in this study predicted tool wear with a reasonable agreement with experimental tool wear. It was found that tool wear increases significantly with cutting speed. The effect of cutting speed was higher than the feed rate at the same material removal rate. Therefore, a lower cutting speed and a higher feed rate was suggested in the current case to improve productivity. Additionally, it was observed that temperature was the driving factor in tool wear. An increase in temperature was more sensitive to cutting speed than feed rate.

# CHAPTER 7. CONCLUSIONS AND FUTURE STUDIES

## 7.1 Conclusions

This research is focused on the numerical study of thermo-mechanical properties of the tool wear during orthogonal machining. The thermo-mechanical properties were evaluated based on the study of temperature, stress, and material velocity. In this work effort made to establish proper prediction of experimental tool wear.

The major findings of this study are listed below:

- An efficient FE formulation was established to investigate the thermo-mechanical behavior of prepared edges and compared with other similar methods.
- A novel technique of predicting tool geometry in relation to tool wear has been implemented successfully, and the effect of worn tool geometry in the machining process has been investigated. It was found that tool wear progression is affected by high temperature, larger stagnation zone, and higher stress at the flank face. This simulated behavior observed agreed with earlier studies.
- Usui tool wear model was used to predict the tool wear and calibrated with a hybrid calibration method. The predicted results have maximum MAPE of 11.09% with experimental flank wear values with a similar pattern of wear. The tool wear prediction accuracy was better for the prepared cutting tool.

- The effect of the different cutting-edge radius was investigated on cutting force, temperature, stress, and material velocity. It was concluded that the temperature is the driven factor in the tool wear progression for prepared edges, and stress concentration is the primary reason for higher tool wear in the unprepared cutting tool. Based on the phenomena of temperature and stress and the probability of ploughing, the optimized cutting tool should be ($E_1$-$E_3$).
- Experimental study showed that prepared coated tools had the best tool wear performance. Numerically, it was found that coating improves the tool performance by reducing the surface temperature on the tool substrate and prepared edges bypassed initial chipping by having a uniform stress distribution on the tool tip, resulting in a significant enhancement in tool life.

## 7.2 Future study

The result of this work showed the efficacy of the developed FE model in predicting thermo-mechanical behavior on the cutting tool. Prospects of study in this subject are the following:

1. Current model was built in 2D environment to simulate orthogonal turning operation. In future, a 3D FEM can be developed to predict more realistic thermo-mechanical behavior in turning operation.

2. The current research investigated the effect of a symmetric cutting edge on thermo-mechanical behavior. A future study could be extended to an asymmetric cutting edge.
3. Characterization of coating properties in order to understand the wear mechanism involved in machining with the coated tool.
4. Develop a computational approach to model coating using micro-mechanical properties (hardness, toughness, plasticity etc.) for coating design and optimization.

**References:**

[1] B. Denkena, J. Koehler, and M. Rehe, "Influence of the honed cutting edge on tool wear and surface integrity in slot milling of 42CrMo4 steel," *Procedia CIRP*, vol. 1, no. 1, pp. 190–195, 2012.

[2] B. Denkena, a. Lucas, and E. Bassett, "Effects of the cutting edge microgeometry on tool wear and its thermo-mechanical load," *CIRP Ann. - Manuf. Technol.*, vol. 60, no. 1, pp. 73–76, 2011.

[3] C. F. Wyen and K. Wegener, "Influence of cutting edge radius on cutting forces in machining titanium," *CIRP Ann. - Manuf. Technol.*, vol. 59, no. 1, pp. 93–96, 2010.

[4] K. D. Bouzakis *et al.*, "Effect of dry micro-blasting on PVD-film properties, cutting edge geometry and tool life in milling," *Surf. Coatings Technol.*, vol. 204, no. 6–7, pp. 1081–1086, 2009.

[5] K. D. Bouzakis *et al.*, "Optimisatioin of the cutting edge roundness and its manufacturing procedures of cemented carbide inserts, to improve their milling performance after a PVD caoting deposition," *Surf. Coatings Technol.*, vol. 163–164, pp. 625–630, 2003.

[6] B. Denkena and D. Biermann, "Cutting edge geometries," *CIRP Ann. - Manuf. Technol.*, vol. 63, no. 2, pp. 631–653, 2014.

[7] M. Agmell, A. Ahadi, O. Gutnichenko, and J. E. Ståhl, "The influence of tool micro-geometry on stress distribution in turning operations of AISI 4140 by FE analysis," *Int. J. Adv. Manuf. Technol.*, vol. 89, no. 9–12, pp. 3109–3122, 2017.

[8] D. Biermann and A. Baschin, "Influence of cutting edge geometry and cutting edge radius on the stability of micromilling processes," pp. 375–380, 2009.

[9] K. S. Woon, M. Rahman, F. Z. Fang, K. S. Neo, and K. Liu, "Investigations of tool edge radius effect in micromachining: A FEM simulation approach," *J. Mater. Process. Technol.*, vol. 195, no. 1–3, pp. 204–211, 2008.

[10] T. H. C. Childs *et al.*, "CIRP Annals - Manufacturing Technology Surface finishes from turning and facing with round nosed tools," vol. 57, pp. 89–92, 2008.

[11] K. Hosseinkhani and E. Ng, "A hybrid experimental and simulation approach to evaluate the calibration of tool wear rate models in machining," 2018.

[12] J. A. Arsecularatne and L. C. Zhang, "Assessment of Constitutive Equations Used in Machining," *Key Eng. Mater.*, vol. 274–276, no. 2004, pp. 277–282, 2004.

[13] T. Özel and T. Altan, "Determination of workpiece flow stress and friction at the chip-tool contact for high-speed cutting," *Int. J. Mach. Tools Manuf.*, vol. 40, no. 1, pp. 133–152, 2000.

[14] A. Thakare and A. Nordgren, "Experimental Study and Modeling of Steady State Temperature Distributions in Coated Cemented Carbide Tools in Turning," *Procedia CIRP*, vol. 31, pp. 234–239, 2015.

[15] V. Schulze and F. Zanger, "Development of a Simulation Model to Investigate Tool Wear in Ti-6Al-4V Alloy Machining," *Adv. Mater. Res.*, vol. 223, pp. 535–544, 2011.

[16] M. Calamaz, D. Coupard, and F. Girot, "A new material model for 2D numerical simulation of serrated chip formation when machining titanium alloy Ti-6Al-4V," *Int. J. Mach. Tools Manuf.*, vol. 48, pp. 275–288, 2009.

[17] M. N. A. Nasr, E. G. Ng, and M. A. Elbestawi, "A modified time-efficient FE approach for predicting machining-induced residual stresses," *Finite Elem. Anal. Des.*, vol. 44, no. 4, pp. 149–161, 2008.

[18] K. Jacobus, R. E. DeVor, and S. G. Kapoor, "Machining-Induced Residual Stress: Experimentation and Modeling," *J. Manuf. Sci. Eng.*, vol. 122, no. 1, p. 20, 2000.

[19] Y. Yen, J. Söhner, B. Lilly, and T. Altan, "Estimation of tool wear in orthogonal cutting using the finite element analysis," vol. 146, pp. 82–91, 2004.

[20] M. Binder, F. Klocke, and B. Doebbeler, "An advanced numerical approach on tool wear simulation for tool and process design in metal cutting," *Simul. Model. Pract.*

*Theory*, vol. 70, pp. 65–82, 2017.

[21] A. Malakizadi, H. Gruber, I. Sadik, and L. Nyborg, "An FEM-based approach for tool wear estimation in machining," *Wear*, vol. 368–369, pp. 10–24, 2016.

[22] W. Grzesik, "Experimental investigation of the cutting temperature when turning with coated indexable inserts," *Int. J. Mach. Tools Manuf.*, vol. 39, no. 3, pp. 355–369, 1999.

[23] I. Krajinović *et al.*, "Finite element study of the influence of hard coatings on hard metal tool loading during milling," *Surf. Coatings Technol.*, vol. 304, pp. 134–141, 2016.

[24] W. Grzesik, M. Bartoszuk, and P. Nieslony, "Finite element modelling of temperature distribution in the cutting zone in turning processes with differently coated tools," *J. Mater. Process. Technol.*, vol. 164–165, pp. 1204–1211, 2005.

[25] M. C. Shaw, *Second Edition*. 2005.

[26] M. E. Merchant, *Mechanics of the cutting process i*. 2017.

[27] S. M. T. HALIM, "Finite Element Modeling of the Orthogonal Metal Cutting Process : Modeling the Effects of Coefficient of Friction and," *McMaster Univ.*, p. 144, 2008.

[28] A. Raczy, M. Elmadagli, W. J. Altenhof, and A. T. Alpas, "An Eulerian Finite-Element Model for Determination of Deformation State of a Copper Subjected to Orthogonal Cutting OF LOCAL STRESSES AND STRAINS," vol. 35, no. August, pp. 2393–2400, 2004.

[29] T. D. Marusich and M. Ortiz, "Modelling and simulation of high speed machining," *Int. J. Numer. Methods Eng.*, vol. 38, no. January, pp. 3675–3694, 1995.

[30] Y. Zhang, J. C. Outeiro, and T. Mabrouki, "On the selection of Johnson-Cook constitutive model parameters for Ti-6Al-4V using three types of numerical models of orthogonal cutting," *Procedia CIRP*, vol. 31, pp. 112–117, 2015.

[31] and A. Movahhedy, M. R., Gadala, M. S., “FE Modeling of Chip Formation in Orthogonal Metal Cutting Process,” *An ALE Approach*, vol. 4, pp. 15–47, 2000.

[32] E. Ng and D. K. Aspinwall, “Modelling of hard part machining.pdf,” vol. 127, pp. 222–229, 2002.

[33] G. Chen, C. Ren, X. Yang, X. Jin, and T. Guo, “Finite element simulation of high-speed machining of titanium alloy (Ti-6Al-4V) based on ductile failure model,” *Int. J. Adv. Manuf. Technol.*, vol. 56, no. 9–12, pp. 1027–1038, 2011.

[34] G. G. Ye, S. F. Xue, W. Ma, and L. H. Dai, “Onset and evolution of discontinuously segmented chip flow in ultra-high-speed cutting Ti-6Al-4V,” *Int. J. Adv. Manuf. Technol.*, no. May, pp. 1–14, 2016.

[35] M. Yaich, Y. Ayed, Z. Bouaziz, and G. Germain, “Numerical analysis of constitutive coefficients effects on FE simulation of the 2D orthogonal cutting process: application to the Ti6Al4V,” *Int. J. Adv. Manuf. Technol.*, vol. 93, no. 1–4, pp. 283–303, 2017.

[36] J. M. Huang and J. T. Black, “An Evaluation of Chip Separation Criteria for the FEM Simulation of Machining,” *J. Manuf. Sci. Eng.*, vol. 118, no. 4, p. 545, 1996.

[37] A. Simoneau, E. Ng, and M. A. Elbestawi, “Chip formation during microscale cutting of a medium carbon steel,” *Int. J. Mach. Tools Manuf.*, vol. 46, no. 5, pp. 467–481, 2006.

[38] G. G. Ye, Y. Chen, S. F. Xue, and L. H. Dai, “Critical cutting speed for onset of serrated chip flow in high speed machining,” *Int. J. Mach. Tools Manuf.*, vol. 86, pp. 18–33, 2014.

[39] S. I. Sun, “A STUDY OF DIFFERENT FEM TECHNIQUES FOR MODELLING 3D METAL CUTTING PROCESS WITH AN EMPHASIZE ON ALE AND CEL FORMULATIONS,” McMaster University, 2014.

[40] P. J. Arrazola, “International Journal of Mechanical Sciences Investigations on the effects of friction modeling in finite element simulation of machining,” vol. 52, pp.

31–42, 2010.

[41] P. J. Arrazola and T. Özel, "Investigations on the effects of friction modeling in finite element simulation of machining," *Int. J. Mech. Sci.*, vol. 52, no. 1, pp. 31–42, 2010.

[42] M. N. A. Nasr, E. G. Ng, and M. A. Elbestawi, "Modelling the effects of tool-edge radius on residual stresses when orthogonal cutting AISI 316L," *Int. J. Mach. Tools Manuf.*, vol. 47, no. 2, pp. 401–411, 2007.

[43] H. Miguélez, R. Zaera, A. Rusinek, A. Moufki, and A. Molinari, "Numerical modelling of orthogonal cutting: Influence of cutting conditions and separation criterion," *J. Phys. IV*, vol. 134, pp. 417–422, 2006.

[44] K. Hosseinkhani and E. Ng, "Analysis of the cutting mechanics under the influence of worn tool geometry," *Procedia CIRP*, vol. 8, pp. 117–122, 2013.

[45] F. Ducobu, P. J. Arrazola, E. Rivière-Lorphèvre, G. O. De Zarate, a. Madariaga, and E. Filippi, "The CEL Method as an Alternative to the Current Modelling Approaches for Ti6Al4V Orthogonal Cutting Simulation," *Procedia CIRP*, vol. 58, pp. 245–250, 2017.

[46] A. Malakizadi, K. Hosseinkhani, E. Mariano, E. Ng, A. Del Prete, and L. Nyborg, "Influence of friction models on FE simulation results of orthogonal cutting process," *Int. J. Adv. Manuf. Technol.*, vol. 88, no. 9–12, pp. 3217–3232, 2017.

[47] ABAQUS Inc., "ABAQUS/Explicit," *ABAQUS Doc.*, pp. 1–28, 2005.

[48] A. Malakizadi, H. Gruber, I. Sadik, and L. Nyborg, "An FEM-based approach for tool wear estimation in machining," *Wear*, vol. 368–369, pp. 10–24, 2016.

[49] A. Malakizadi, K. Hosseinkhani, E. Mariano, and E. Ng, "Influence of friction models on FE simulation results of orthogonal cutting process," pp. 3217–3232, 2017.

[50] J. Rech, P. J. Arrazola, C. Claudin, C. Courbon, F. Pusavec, and J. Kopac, "Characterisation of friction and heat partition coefficients at the tool-work material interface in cutting," *CIRP Ann. - Manuf. Technol.*, vol. 62, no. 1, pp. 79–82, 2013.

[51] J. M. Boyd, K. Hosseinkhani, S. C. Veldhuis, and E. Ng, "Improved prediction of cutting forces via finite element simulations using novel heavy-load, high-temperature tribometer friction data," *Int. J. Adv. Manuf. Technol.*, vol. 86, no. 5–8, pp. 2037–2045, 2016.

[52] F. Kone, C. Czarnota, B. Haddag, and M. Nouari, "Finite element modelling of the thermo-mechanical behavior of coatings under extreme contact loading in dry machining," *Surf. Coatings Technol.*, vol. 205, no. 12, pp. 3559–3566, 2011.

[53] M. Shatla, C. Kerk, and T. Altan, "Process modeling in machining . Part II : validation and applications of the determined flow stress data," vol. 41, pp. 1659–1680, 2001.

[54] B. Denkena, A. Lucas, and E. Bassett, "CIRP Annals - Manufacturing Technology Effects of the cutting edge microgeometry on tool wear and its thermo- mechanical load," vol. 60, pp. 73–76, 2011.

[55] A. I. N. Press, "Mechanics of high speed cutting with curvilinear edge tools," vol. 48, pp. 195–208, 2008.

[56] K. W. Kim, W. Y. Lee, and H. C. Sin, "Finite-element analysis of machining with the tool edge considered," *J. Mater. Process. Technol.*, vol. 86, no. 1–3, pp. 45–55, 1999.

[57] M. S. Mengesha, B. Denkena, and J. Ko, "Influence of the cutting edge rounding on the chip formation process : Part 1 . Investigation of material flow , process forces , and cutting temperature," pp. 329–338, 2012.

[58] B. T. C. K.J. Trigger, "An analytical evaluation of metal cutting temperatures."

[59] I. Al-Zkeri, J. Rech, T. Altan, H. Hamdi, and F. Valiorgue, "Optimization of the cutting edge geometry of coated carbide tools in dry turning of steels using a finite element analysis," *Mach. Sci. Technol.*, vol. 13, no. 1, pp. 36–51, 2009.

[60] J. Rech, T. Altan, H. Hamdi, and F. Valiorgue, "OPTIMIZATION OF THE CUTTING EDGE GEOMETRY OF COATED CARBIDE TOOLS IN DRY

TURNING OF STEELS USING A FINITE ELEMENT ANALYSIS," vol. 0344, 2009.

[61] C. L., E.-W. T.I., N. M., and E. M.A., "Effects of Edge Preparation and Feed when Hard Turning a Hot Work Die Steel with Polycrystalline Cubic Boron Nitride Tools," *CIRP Ann. - Manuf. Technol.*, vol. 55, no. 1, pp. 89–92, 2006.

[62] P. Bhattacharyya, D. Sengupta, S. Mukhopadhyay, and A. B. Chattopadhyay, "On-line tool condition monitoring in face milling using current and power signals," *Int. J. Prod. Res.*, vol. 46, no. 4, pp. 1187–1201, 2008.

[63] H. Takeyama and R. Murata, "Basic Investigation of Tool Wear," *J. Eng. Ind.*, vol. 85, no. 1, p. 33, 1963.

[64] K. Hosseinkhani and E. Ng, "A hybrid experimental and simulation approach to evaluate the calibration of tool wear rate models in machining," *Int. J. Adv. Manuf. Technol.*, pp. 1–16, 2018.

[65] A. Attanasio, E. Ceretti, A. Fiorentino, C. Cappellini, and C. Giardini, "Investigation and FEM-based simulation of tool wear in turning operations with uncoated carbide tools," *Wear*, vol. 269, no. 5–6, pp. 344–350, 2010.

[66] E. Usui, T. Shirakashi, and T. Kitagawa, "Analytical prediction of cutting tool wear," *Wear*, vol. 100, no. 1–3, pp. 129–151, 1984.

[67] K. Hosseinkhani and E. Ng, "A combined empirical and numerical approach for tool wear prediction in machining," *Procedia CIRP*, vol. 31, pp. 304–309, 2015.

[68] L. Xie, J. Schmidt, C. Schmidt, and F. Biesinger, "2D FEM estimate of tool wear in turning operation," vol. 258, pp. 1479–1490, 2005.

[69] L. Filice, F. Micari, L. Settineri, and D. Umbrello, "Wear modelling in mild steel orthogonal cutting when using uncoated carbide tools," vol. 262, pp. 545–554, 2007.

[70] M. Binder, F. Klocke, and B. Doebbeler, "Simulation Modelling Practice and Theory An advanced numerical approach on tool wear simulation for tool and process design in metal cutting," *Simul. Model. Pract. Theory*, vol. 70, pp. 65–82, 2017.

[71] T. Özel, T. Thepsonthi, D. Ulutan, and B. Kaftanolu, “Experiments and finite element simulations on micro-milling of Ti-6Al-4V alloy with uncoated and cBN coated micro-tools,” *CIRP Ann. - Manuf. Technol.*, vol. 60, no. 1, pp. 85–88, 2011.

[72] T. Özel, M. Sima, a. K. Srivastava, and B. Kaftanoglu, “Investigations on the effects of multi-layered coated inserts in machining Ti-6Al-4V alloy with experiments and finite element simulations,” *CIRP Ann. - Manuf. Technol.*, vol. 59, no. 1, pp. 77–82, 2010.

[73] C. Courbon, V. Sajn, D. Kramar, J. Rech, F. Kosel, and J. Kopac, “Journal of Materials Processing Technology Investigation of machining performance in high pressure jet assisted turning of Inconel 718 : A numerical model,” *J. Mater. Process. Tech.*, vol. 211, no. 11, pp. 1834–1851, 2011.

[74] F. Ducobu, E. Rivière-Lorphèvre, and E. Filippi, “Mesh influence in orthogonal cutting modelling with the Coupled Eulerian-Lagrangian (CEL) method,” *Eur. J. Mech. A/Solids*, vol. 65, pp. 324–335, 2017.

[75] S. M. T. HALIM, “Finite Element Modeling of the Orthogonal Metal Cutting Process : Modeling the Effects of Coefficient of Friction and,” McMaster University, 2008.

[76] T. Lee, “An Experimental and Theoritical Investigation for the Machining of Hardened Alloy Steels,” no. April, 2007.

[77] Keyan Wang, “Johnson-cook failure parameters,” *McMaster Univ.*, p. 103, 2016.

[78] J. Ma, X. Ge, S. I. Chang, and S. Lei, “Assessment of cutting energy consumption and energy efficiency in machining of 4140 steel,” *Int. J. Adv. Manuf. Technol.*, vol. 74, no. 9–12, pp. 1701–1708, 2014.

[79] E. ARDALAN, “THE EFFECT OF TOOL EDGE RADIUS ON CUTTING CONDITIONS BASED ON UPDATED LAGRANGIAN FORMULATION IN FINITE ELEMENT METHOD,” McMaster University, 2017.

[80] T. K. Kershah, “Prediction of cutting coefficients during orthogonal metal cutting

process using FEA approach," McMaster University, 2013.

[81] W. Wang, "Application of edge preparation technologies to improve tool performance," McMaster University, 2018.

[82] L. Filice, F. Micari, S. Rizzuti, and D. Umbrello, "Short Communication A critical analysis on the friction modelling in orthogonal machining," vol. 47, pp. 709–714, 2007.

[83] B. Haddag, S. Atlati, M. Nouari, and M. Zenasni, "Analysis of the heat transfer at the tool – workpiece interface in machining : determination of heat generation and heat transfer coefficients," no. January, 2015.

[84] R. Kountanya, I. Al-zkeri, and T. Altan, "Journal of Materials Processing Technology Effect of tool edge geometry and cutting conditions on experimental and simulated chip morphology in orthogonal hard turning of 100Cr6 steel," vol. 209, pp. 5068–5076, 2009.

[85] E. G. NG, T. El-Wardany, and M. A. ELBESTAWI, *Influence of flank wear length on residual stress and workpiece quality in machined-surfaces*. 2003.

[86] S. Atlati, B. Haddag, M. Nouari, and A. Moufki, "Tribology International Effect of the local friction and contact nature on the Built-Up Edge formation process in machining ductile metals," *Tribiology Int.*, vol. 90, pp. 217–227, 2015.

[87] J. S. Strenkowski and K. Moon, "Finite Element Prediction of Chip Geometry and Tool / Workpiece Temperature Distributions in Orthogonal Metal Cutting," 2019.

[88] Z. Y. Wang and K. P. Rajurkar, "Cryogenic machining of hard-to-cut materials," pp. 168–175, 2000.

[89] D. E. D. Sr, "On-line metal cutting tool condition monitoring . I : force and vibration analyses," vol. 40, pp. 739–768, 2000.

[90] R. E. Devor and S. G. Kapoor, "The Mechanics of Machining at the Microscale : Assessment of," vol. 126, no. November 2004, 2019.

[91] M. R. Movahhedy, Y. Altintas, and M. S. Gadala, “Cutting With Chamfered and Blunt Tools,” vol. 124, no. May 2002, 2019.

[92] I. Summary, “The role of tool-chip contact length in metal cutting,” vol. 37, pp. 613–627, 1993.

[93] F. B. De Oliveira, A. R. Rodrigues, R. T. Coelho, and A. F. De Souza, “Size effect and minimum chip thickness in micromilling,” *Int. J. Mach. Tools Manuf.*, vol. 89, pp. 39–54, 2015.

[94] P. C. Wanigarathne, A. D. Kardekar, O. W. Dillon, G. Poulachon, and I. S. Jawahir, “Progressive tool-wear in machining with coated grooved tools and its correlation with cutting temperature,” *Wear*, vol. 259, no. 7–12, pp. 1215–1224, 2005.

[95] J. C. Aurich, T. Eyrisch, and M. Zimmermann, “Effect of the coating system on the tool performance when turning heat treated AISI 4140,” *Procedia CIRP*, vol. 1, no. 1, pp. 214–219, 2012.

[96] AZoM, “AZO MATERIALS, AISI 4140 Alloy Steel (UNS G41400),” *AZoM.com - An AZoNetwork Site*, 2012. .

[97] F. Jiang, L. Yan, and Y. Rong, “Orthogonal cutting of hardened AISI D2 steel with TiAlN-coated inserts - Simulations and experiments,” *Int. J. Adv. Manuf. Technol.*, vol. 64, no. 9–12, pp. 1555–1563, 2013.

[98] B. Deng, “INVESTIGATION OF THE EFFECT OF TOOL GEOMETRY ON THE MACHINING PROCESS INVESTIGATION OF THE EFFECT OF TOOL GEOMETRY ON THE MACHINING PROCESS BY,” McMaster University, 2018.